Biologically Adapted Radiotherapy on the Basis of Hypoxia Imaging with Positron Emission Tomography

Dissertation

zur Erlangung des Grades
eines Doktors der Naturwissenschaften

der Fakultät für Mathematik und Physik
der Eberhard-Karls-Universität zu Tübingen

vorgelegt von

Daniela Thorwarth
aus Reutlingen

2007

Tag der mündlichen Prüfung:	30. Januar 2007
Dekan:	Prof. Dr. Nils Schopohl
1. Berichterstatter:	Prof. Dr. Dr. Fritz Schick
2. Berichterstatter:	Prof. Dr. Hanns Ruder
3. Berichterstatter:	Prof. Dr. Fridtjof Nüsslin

Contents

List of abbreviations

BTV	Biological Target Volume
CT	Computed Tomography
DE	Dose Escalation
DP	Dose Painting
DPBN	Dose Painting by Numbers
DRE	Diffusion-Reaction Equation
FDG	[^{18}F]-Fluorodeoxyglucose
***f*-IGRT**	Functional Image Guided Radiotherapy
FMISO	[^{18}F]-Fluoromisonidazole
HIDE	Hypoxia Image Guided Dose Escalation
HNC	Head-and-Neck Cancer
IMRT	Intensity Modulated Radiotherapy
MI	Mutual Information
OAR	Organ at Risk
PET	Positron Emission Tomography
PFS	Progression-Free Survival
PTV	Planning Target Volume
pi	post injection
RT	Radiotherapy
SUV	Standardized Uptake Value
TAC	Time-Activity Curve
TCP	Tumour Control Probability
uniDE	uniform Dose Escalation

Chapter 1

Introduction

The development of molecular imaging modalities has been revolutionizing the diagnosis of human cancer in the last years. These new imaging techniques, especially positron emission tomography (PET) and functional magnetic resonance imaging (f-MRI), are used as complementary medical imaging tools in addition to computed tomography (CT). The purely anatomical images acquired with CT allow for the determination of position and extent of human tumours. In contrast, molecular imaging data reveal the structural and functional nature of the tissue, which can vary strongly throughout the whole tumour. Only with functional imaging it is possible to quantify the heterogeneity and irregularity of the structural tissue configuration. As a consequence of the newly developed methods for cancer diagnosis and an increased understanding of tumour biology, a number of targeted therapy approaches have recently been proposed and are currently beefing investigated.

Already in the 1950s it was found that heterogeneities in the structural architecture of a tumour can cause increased resistance to radiation therapy [21, 63]. Only now it is possible to assess these characteristics with new imaging techniques and use the obtained functional information as a basis for the design of biologically adapted therapies.

Radiotherapy (RT) treatment especially of the head-and-neck region still fails frequently. A targeted RT strategy, that makes use of the individual, internal functional features of the tissue assessed by new molecular imaging techniques could affect a great therapeutic gain. A biologically adapted treatment approach that targets the tumour according to the information detected via biological imaging may have high potential with regard to the overall survival rate of cancer patients [37].

The main idea for the design of a targeted RT treatment is to 'sculpt' or 'paint' the radiation dose according to the functional characteristics of the

tumour. The required radiation doses for such a 'dose painting' treatment may be highly irregular. Therefore, a RT technique is necessary which is able to accurately deliver inhomogeneous and highly varying doses. The technical basis for such an individually adapted radiotherapy is formed by intensity modulated radiotherapy (IMRT), as it is capable to produce spatially variant dose distributions [2].

During this PhD work, four main steps were developed which are necessary for the translation of functional imaging data into an individually adapted and targeted RT treatment. After a short introduction on the basics of tumour biology in **chapter 2** and the princliples of molecular imaging techniques in **chapter 3**, these four steps which were developed in the context of this project are discussed.

- In order to interpret reliably the internal properties of a tumour tissue, a series of molecular imaging data are needed which illustrate the characteristic temporal distribution of a marker substance in the tissue. For example, a dynamic positron emission tomography data acquisition enables us to assess this kind of temporal information. In order to analyze and interpret these dynamic data sets, a mathematical model which describes this transport phenomenon is necessary. In **chapter 5**, a physical transport model for the analysis of the uptake and distribution of the hypoxia PET tracer [^{18}F]-Fluoromisonidazole (FMISO) is developed. The model is derived from the general three-dimensional Diffusion-Reaction-Equation. A number of different model parameters can be determined from a fit of the model to the data curves which enable for the estimation of various functional parameters of the tumour. Thus, the model allows us to draw conclusions about the characteristic functional architecture of the underlying tumour tissue.

- In a second step, s statistical analysis was carried out in order to identify the main kinetic parameters which are relevant for therapy success. To reach this goal, parameters deduced from the kinetic analysis were compared to other important properties of a tumour. In the context of **chapter 6**, characteristic patterns of two important model parameters are investigated. Furthermore, a statistical analysis is performed in order to correlate these model parameters to RT treatment outcome.

- The key issue for the translation of functional imaging data into an individual prescription for RT is a model that is capable of predicting the probability of therapy success for a patient as a function of the molecular imaging data. In **chapter 7**, a tumour control probability

(TCP) model is introduced. The design of the model is based on characteristic changes in the functional imaging data during the course of RT treatment. This model presents essentially three features: (1) It involves characteristic values derived from the dynamic FMISO PET data. (2) The TCP model allows us to estimate the time a tumour needs until reoxygenation occurs. (3) The model is calibrated using therapy outcome data of a group of 15 patients.

- The established TCP model then allows for individual and spatially varying dose prescriptions for RT treatment planning. A treatment planning study is performed in **chapter 8** where two different approaches of targeted RT techniques are compared. The first approach increases the dose uniformly to a biological target volume that is delineated on the basis of the intensity distribution of a static PET image. In contrast, the second set of plans applies spatially variant doses according to the requirements of the dynamic FMISO PET images. A group of 13 patients was included into this planning study. The aim of the study was to evaluate the feasibility of individually adapted RT methods in a clinical setting and to estimate the potential gain of treatment success in a patient population.

Chapter 2

Fundamentals of Tumour Biology

The emergence of cancer is caused by mutations in the DNA of normal cells. A series of mutations to certain classes of genes is usually required before a normal cell will transform into a cancer cell. Only mutations in certain types of genes that are important for cell division, cell death, and DNA repair cause cancer. A tumour can originate from the genetic degeneration of a single cell. With each carcinogenic mutation, a cell gains a slight selective advantage over its neighbors, resulting in a process known as clonal evolution. This leads to an increased chance that the descendants of the original mutant cell will acquire extra mutations, giving them even more selective advantage.

Cells that are capable of forming malignant tumours present a number of properties which distinguish them from normal tissue cells:

- evasion of cell death (apoptosis)
- increased rate of uncontrolled cell division (proliferation)
- self-sufficiency with respect to growth factors
- insensitivity to anti-growth factors
- ability to promote growth of new blood vessels (angiogenesis)
- ability to invade neighbouring tissues
- capability to form metastasis at distant sites

2.1 Proliferation

The physiological process of cell division is called *proliferation*. It occurs in almost all tissues and under many circumstances. Normally the balance between proliferation and programmed cell death, usually in the form of apoptosis, is maintained by tight regulation of both processes to ensure the integrity of organs and tissues. A tumor consists of a population of rapidly dividing and growing cells, where the cancer cells have lost control over their ability to divide in a controlled fashion [4].

A consequence of uncontrolled proliferation in transformed cells is the increased uptake of nutrients [8]. Furthermore, there is a large difference in proliferation rate between cells located in areas close to blood vessels and those adjacent to regions of necrosis because of lack of supply. A reduced proliferation rate is observed for tumour cells distant from vasculature [14].

2.2 Neovascularization, Angiogenesis

Tumour growth, resulting from uncontrolled neoplastic cell division, is absolutely dependent on parallel expansion of the tumour vasculature to maintain sufficient supply of oxygen and nutrients for growth. Thus, neovascularization is a universal characteristic of all solid tumours larger than 1-2 mm^3. Blood vessel growth (angiogenesis) is induced by secreting various growth factors, such as the Vascular Endothelial Growth Factor (VEGF). These growth factors can induce capillary growth into the tumour, supplying required nutrients and allowing for further tumour expansion.

Regular directed growth of blood vessels requires complex bio-chemical control mechanisms, which are often not present in loosely regulated and rapidly proliferating tumour cells. Hence, tumour vasculature is very likely to be morphologically and functionally abnormal. Tumour blood supply is characterized by spatial and temporal heterogeneity in both structure and function [14]. Often, the newly formed vascular stretches do not show any hierarchy. Abrupt changes in diameter as well as dead ends are common features. Extreme heterogeneity of vascular density and individual microvascular architecture are observed in human tumours [34, 67].

2.3 Hypoxia

Endothelial cells have much longer doubling times than cancer cells. Therefore, tumours 'outgrow' their blood supply; neovascularization lags behind

proliferation and consequently the vasculature is unable to meet the increasing nutrient and oxygen demands of the expanding tumour mass [14]. The missing hierarchy and the chaotic structure in the blood vessel system push distant subpopulations of rapidly proliferating cells to face a lack of oxygen [26, 27, 67]. Hence, hypoxia occurs far from blood vessels as a result of the limited diffusion length of oxygen and O_2 consumption of the cells closer to the capillaries. As a consequence of the structural architecture of a tumour, cells are hypoxic for time intervals in the order of several days or even weeks. Additionally, they are also subject to chronic depletion of nutrient supplies and do therefore no longer show any proliferating activities. This phenomenon is referred to as chronic or diffusion limited hypoxia [17].

In contrast to the described chronic type, hypoxia can also result from dynamic changes in microregional perfusion, which is referred to as acute hypoxia [17]. Acutely hypoxic cells are exposed to relatively short periods of oxygen deprivation and as a consequence they are still healthy and actively proliferating.

The structural architecture of tumour tissues, showing chaotic organization of blood vessels, increased proliferation close to capillaries and hypoxia only distant from blood vessels was clearly shown by a number of immunohistochemical studies [11, 30–32, 38, 41] (see figure 2.1. Ljungkvist *et al* [38–41] and Janssen *et al* [30, 31] investigated the structural architecture of hypoxic tumours with pimonidazole. These studies depict hypoxic islands interspersed throughout the tissue on length scales between 100 and 500 μm, located in regions far from blood vessels and including necrotic tissue, as illustrated by figure 2.1.

2.4 Radiation Resistance

Hypoxic cells are much less sensitive to radiation than well-oxygenated cells [28]. The first indication that hypoxia exists in tumours and that this phenomenon could also be the reason of lower radiation sensitivity was made in the 1950s by Thomlinson and Gray [63]. It was also reported, that the response of cells to ionizing radiation was strongly dependent on oxygen. Hypoxic tumours were found to show $2.5-3$ times higher levels of radioresistance than well oxygenated cancer tissues [21]. Hypoxia-associated radioresistance can be described by the so-called *oxygen enhancement effect*: When radiation is absorbed in biological systems, free radicals are produced. If oxygen is present, it can react with the radicals $R^\bullet$ produced directly in the critical target to produce $RO_2^\bullet$, which then undergoes further reaction to yield ROOH in the target molecule. The induced change in the chemical compo-

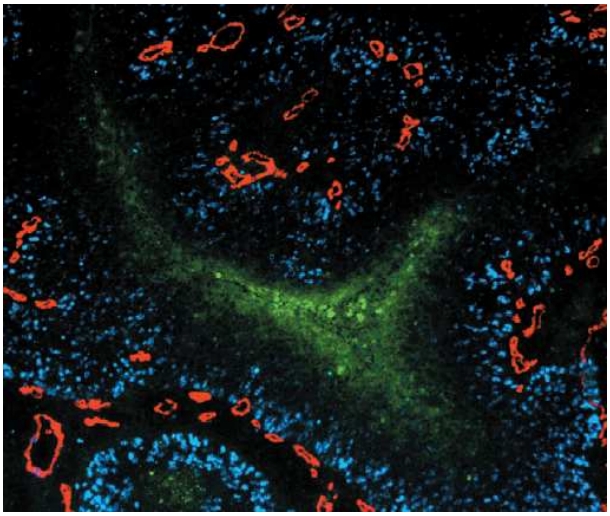

Figure 2.1: Microscopic image of human squamous-cell carcinoma of the oral cavity with immunofluorescent labelling of blood vessels (PAL-E, red), proliferating cells (iododeoxyuridine, blue), and hypoxic cells (pimonidazole, green). Figure taken from [32].

sition of the target fixes the damage [28, 45]. In the absence of oxygen, or in the presence of reducing species, $R^{\bullet}$ will restore its original form. Due to this effect, the radiation dose required to achieve the same biological effect is three times higher in the absence of oxygen than in the presence of normal levels of oxygen.

In addition, hypoxic cells show only very reduced cell division rates due to much longer cell cycles. As the cell DNA is most sensitive to radiation during mitosis, the phase of cell division, DNA damage is less effective on average in hypoxic cells.

Hypoxic tumours were reported to present not only reduced radiosensitivity, but they are also known to be resistant to certain chemotherapeutic agents and other non-surgical treatment modalities. An insufficient vasculature does not only cause hypoxia distant from blood vessels. A parallel symptom is the insufficient transport of drugs to tumour cells existing at a certain distance from the vessels. Hence, hypoxia causes and coincides with a certain degree of general therapy resistance.

As hypoxia alters the biochemical structure of tumours and induces a selective pressure on the tumour cells, a malignant behaviour of the tumour is promoted [28]. Hypoxic tumour cells cause increasing probability of local spread (direct invasion of neighbouring tissues and organs), regional spread

(through metastasis to the lymph nodes) and distant spread (distant metastasis) [27].

Chapter 3

The Basics of Molecular Imaging

Molecular imaging, also referred to as functional or biological imaging, allows for in vivo evaluation of targeted molecules or biological processes in human tumour tissues. In contrast to conventional radiological imaging techniques, such as computed tomography (CT) that primarily provide anatomical information, biological imaging reveals metabolic, functional and physiological data [37].

Positron emission tomography (PET) is a highly sensitive and also quantitative molecular imaging modality used in clinical practice [60]. Molecular imaging with PET enables for non-invasive visualization of different functional and biological characteristics of tumour tissues. PET is clinically used for the assessment of tumour extent, glucose metabolism, proliferation and tumour hypoxia. Further, physiological processes in the tumour tissue can be assessed with PET and used for therapy guidance.

The use of functional imaging is being complicated by specific diffusion and accumulation characteristics of the tracers. Additionally, the different mechanisms in the tissue face to a high level of heterogeneity. Further problems are induced to functional imaging by patient movement and high levels of image noise.

3.1 Positron Emission Tomography

PET scanners are commonly used for clinical functional imaging. PET examinations require the injection of radioactive markers which decay by positron emission. Due to the kinetic energy of the emitted positron, the positron range lies in the order if a few millimeters, which imposes a lower limit on

the spatial resolution of the PET scanner. The fundamental signal of the scanner results from the annihilation of the positron with an electron. This results in the production of two photons, each having an energy corresponding to the electron mass (511 keV), and a neutrino. The two photons are emitted with an angle of approximately 180 degrees. Via coincidence measurement, the annihilation photons are then registered in a detector ring. Only unscattered photon pairs contribute useful information to the image formation [69].

3.1.1 Data Acquisition

The PET measurements performed in the context of this work were acquired on a whole-body scanner (Advance, GE Medical Systems, Milwaukee, US) with an axial field of view (FOV) of 14.9 cm. The imaging process includes two different imaging steps: a transmission and an emission scan. The 20 min transmission scan is used for attenuation correction and is performed with three rotating ^{68}Ge sources. The obtained attenuation data are used during the reconstruction of the emission counts. For the emission scan, the total activity of the injected radionuclide is determined according to the patient's weight and to the half-live of the isotope used. When ^{18}F, which has a half-live of $\approx$ 108 min, is used as positron emitter, a total activity of $\approx$ 400 MBq is injected for a patient examination. The duration of the emission scan is calculated as a function of the time after injection and the weight of the patient. When ^{18}F is used as a positron emitter, a scan taken 2 h post injection (pi) will typically require data acquisition for approximately 5-6 min, whereas a 4 h pi scan will take 10-12 min.

After attenuation correction, the data are reconstructed with an iterative ordered subsets expectation maximization (OSEM) algorithm. The reconstructed images have $128 \times 128 \times 35$ voxels, each with a spatial resolution of $4 \times 4 \times 4.25$ mm^3.

Static PET images are made during a period when the activity distribution is fairly stable and the counting time is long enough to obtain good quality images. A typical application is the measurement of glucose metabolism using the tracer [^{18}F]-Fluorodeoxyglucose (FDG) [19, 51, 55, 56, 72].

3.1.2 Dynamic Acquisition

In contrast to static PET images, dynamic studies are used in cases in which it is necessary to follow the changes of the activity distribution over a long period to get a more detailed image of the underlying physiology. Dynamic scans are performed using a series of imaging frames (see figure 3.1), which

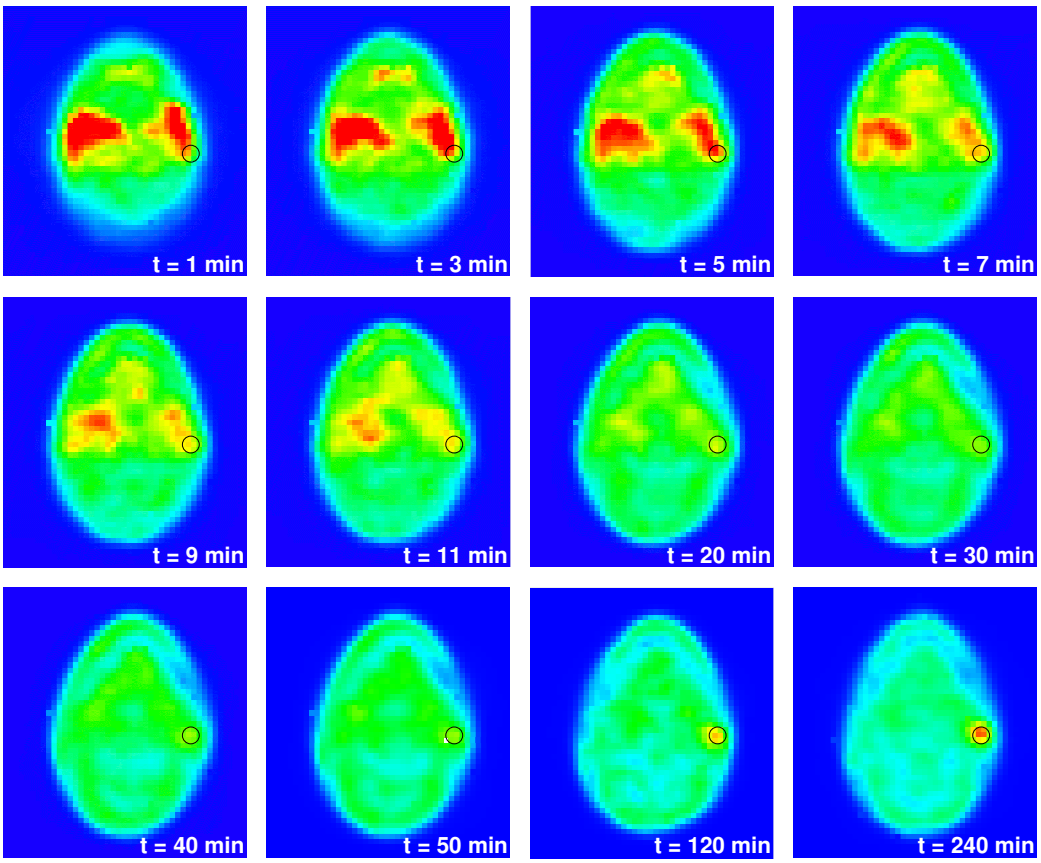

Figure 3.1: Dynamic series of FMISO PET scans. The images show one slice of a head-and-neck cancer patient, including the respective acquisition time points t.

normally get longer as the study progresses. In our case, dynamic data acquisition was performed during a time interval of up to 60 min, resulting in a total number of $\approx$ 40 image frames. Data acquisition started exactly at the time of marker injection and during the first two minutes pi, data were registered every 10 s. From 2 to 4 min pi, the counting time was 15 s and until 15 min pi, images were taken every minute. During 15-60 min pi, emission data were saved every 5 min.

Each image is reconstructed as if it were acquired independently, but only one transmission scan is taken for the whole dynamic image series.

The dynamic scanning mode adds a fourth dimension to the emission data. For each image voxel, a time-activity-curve (TAC) can be determined which shows the temporally varying activity distribution in the respective

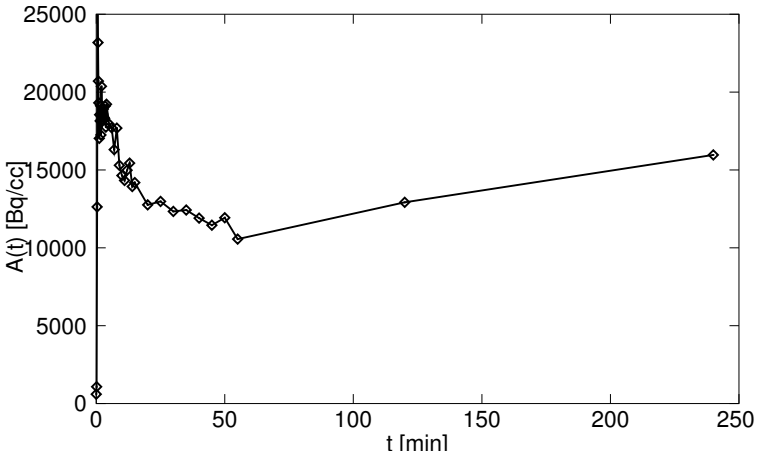

Figure 3.2: FMISO Time-Activity Curve. The TAC shown here corresponds to the marked voxel of the dynamic PET scan for the patient shown in figure 3.1. The TAC includes more times points than represented in figure 3.1.

voxel. Figure 3.2 shows an example TAC for the marked voxel in the data set of the patient represented in figure 3.1.

If the acquired TACs are not long enough (i.e. $\geq$ 1 h) to visualize the functional characteristics of the tissue, which is the case for the tracer used for this work ([^{18}F]-FMISO), the dynamic data can be extended "artificially". To reach this, additional static scans are taken several hours pi ($2, 3, 4, \cdots$ h). Unfortunately, each of these late image frames requires a separate transmission scan. The patient is in general repositioned for the acquisition of the late images, which necessitates subsequent alignment of the data sets.

3.1.3 Image Fusion

Image fusion was performed automatically using an entropy based mutual information algorithm [68]. This algorithm maximizes the mutual information $I(X, Y)$ of two images, which is defined by

$$I(X,Y) = \sum_{y \in Y} \sum_{x \in X} p(x,y) \ \log \frac{p(x,y)}{p(x)p(y)} \quad . \tag{3.1}$$

The mutual information $I(X, Y)$ measures the distance between the joint distribution of the image values $p(x, y)$ and the joint distribution in the case of independence of the two images $p(x)p(y)$ [53]. It is a measure of dependence of the two images. It is assumes, that there is maximal dependence between

the image values when the images are correctly aligned. Misregistration will result in a decrease in the measure.

Pointwise TACs were calculated by applying the resulting transformation matrix. A matching accuracy of $\leq$ 2 mm ($\approx$ 0.5 voxel) could be reached. Notice, that the errors of the late data points are not only due to statistical reasons, but also resulting from mismatches during the image fusion process.

3.2 Hypoxia Imaging

3.2.1 FMISO

[^{18}F]-Fluoromisonidazole (FMISO) is a hypoxia-specific tracer molecule routinely used for clinical PET examinations. The chemical structure of the tracer molecule FMISO is shown in figure 3.3, where the NO_2 is the functional group responsible for the binding characteristics of FMISO in the tissue and ^{18}F is the positron emitting agent required for PET.

FMISO binds selectively to macromolecules in hypoxic cells. At low oxygen levels ($\approx 5 - 10$ mm Hg), the compound is reduced and binds, when reduced by a second electron, covalently to intracellular macromolecules (see also figure 3.4). In the presence of oxygen, the favoured reaction is the reoxygenation to the less reactive parent compound which is freely diffusible and clears from tissue [35].

In vitro investigations of tracer specific distribution and binding characteristics were performed by [58]. Covalent binding was reported to take place approximately $2 - 3$ h post injection (pi). According to these findings, Koh *et al* [33] and Rasey *et al* [57] developed a strategy for the identification and quantification of hypoxic tumour areas on the basis of FMISO PET images. They pointed out the necessity of very long ($2 - 4$ h) examination proto-

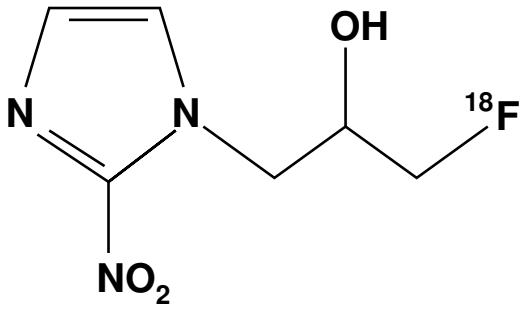

Figure 3.3: Chemical structure of the hypoxia PET tracer [^{18}F]-FMISO.

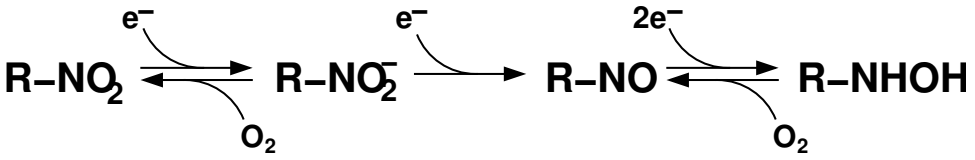

Figure 3.4: Schematical representation of the chemical reaction of [^{18}F]-FMISO (R-NO_2) in the tissue.

cols because of the slow transport and reaction mechanisms of the tracer molecules. The presented results displayed a highly variable character of human tumour hypoxia among different tumours and also among regions within the same tumour.

A fractional hypoxic volume (FHV) of the tumour was defined as the proportion of the tumour area presenting a tumour-to-blood activity ratio ≥ 1.4 at $2-3$ h pi. This FHV based on static FMISO PET scans taken $2-4$ h pi is commonly used for the analysis of clinical hypoxia PET images [24, 33, 44, 55, 57].

Eschmann *et al* [18] pointed out for the first time the necessity of long and *dynamically acquired* FMISO PET examinations because of the slow distribution and uptake characteristics of the tracer in the tumour tissue.

In contrast to other investigators, Casciari *et al* [12] developed a kinetic compartment model for the characterization of the transport and metabolism of FMISO. This model aims to determine the cellular FMISO reaction rate constant from time-activity data, which is assumed to reflect the mean local oxygen concentration. It consists of four compartments with a high number of free parameters. Hence, a certain number of parameters have to be fixed to increase the robustness of the model. The model is a classical kinetic model where the different compartments co-exist in the same volume. This is problematic because it assumes homogeneous oxygen concentration which contradicts the observation of concentration gradients in a tissue.

Fortunately, the pattern of tracer accumulation in hypoxic tumours can be made visible by histological investigations with the related compound pimonidazole, which is by means of cellular binding mechanisms identical to FMISO (cf. figures 3.3 and 3.4). Ljungkvist et al [38–41] and Janssen et al [30, 31] showed, that hypoxia exists only far (several 100 μm) from blood vessels, as represented in figure 2.1. A 'hypoxia-signal' on macroscopic length scales (size of PET-voxels: $4 \times 4 \times 4.25$ mm^3) emerges from an irregular heterogeneous distribution of tracer accumulation on microscopic length scales.

The essential fact that hypoxia exists spatially separated and at any rate

far from perfused vessels was not explicitely taken into account in the design of the compartment model by [12]. Also, it becomes evident that the total sub-volume which traps the tracer is rather small. These observations are typical of the problem and serve to make the point that hypoxia-PET imaging with any arbitrary tracer is more ambiguous and intricate than with tracers with an active transport mechanism and higher reaction rates, such as FDG, and to justify that some model is required to interpret the images.

The immunohistochemical studies also revealed large inter- and intra-patient differences in regard to tumour tissue vasculature. Hypoxia is only a consequence of the irregular geometry of the tumour vasculature. Therefore, it is essential that a model for the transport of the tracer from the perfused vessels to the hypoxic cell is general enough to include both the irregular tumour geometry and the inter-individual tumour heterogeneity.

3.2.2 Tracer Transport

The transport of the PET marker in the patient is mainly governed by two phenomena: the distribution of the tracer in to blood pool and the transport into the interstitial space.

The distribution of the tracer by the blood flow is very fast and takes place on length scales of a few minutes. However, due to the extremely heterogeneous structure of the tumour vasculature, there might still be regions with low levels of tracer at a certain distance from the vessel.

The transport of the FMISO molecule through the tumour tissue is purely diffusive and therefore depends crucially in the tissue geometry.

Histochemical studies [11, 30, 31, 38–41] found increasing staining intensities for pimonidazole in addition to a larger quantity of cells accumulating the tracer molecules far from blood vessels. Typical distances for increased pimonidazole staining are $100 - 300$ μm, as shown in figure 3.5. Since there exists no active transport mechanism for pimonidazole or FMISO in the extracellular space, the transport of the tracer molecules is purely diffusive [29]. Considering the molecular weight of FMISO and the distances the molecules have to travel from the vessel to the hypoxic cell [29], the diffusion time will be high compared to other tracers with active transport mechanisms and shorter diffusion distances (such as eg. FDG [35]). The time the marker needs to reach the hypoxic tissue area far from the blood vessel will be in the order of $100 - 1000$ s, as motivated in the following chapter.

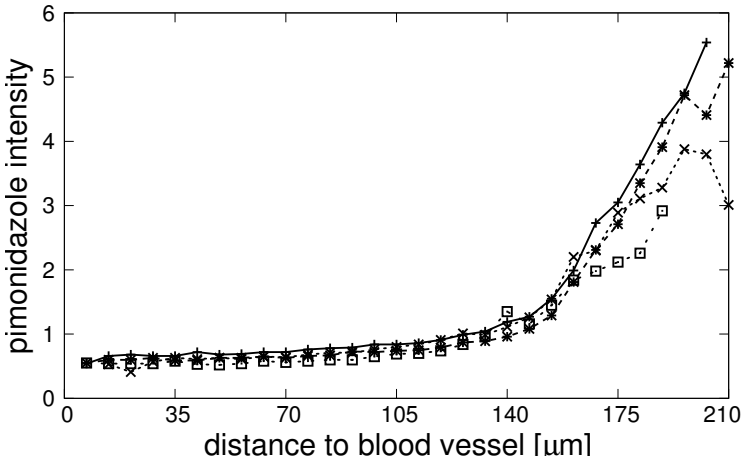

Figure 3.5: Pimonidazole staining intensities in arbitrary units as a function of the distance to the closest blood vessel. Data are taken from human head-and-neck cancer. Courtesy to H Janssen and A Begg, Amsterdam.

3.3 Experimental Data

3.3.1 Patient Data

After informed consent, fifteen patients with advanced stage head and neck cancer (HNC) were examined in the context of this study. Patients were examined with a dynamic FMISO PET before the start of radiotherapy (RT). In addition, a static FDG PET image was also taken approximately 3-5 days before the first treatment fraction. The majority of these patients was underwent one to three follow-up FMISO scans during the course of RT. For each patient, additional computed tomography (CT) image data was available. These CT scans, on which delineation of target volumes and organs at risk was performed, were used for RT treatment planning.

Characteristics of the group of 15 patients are summarized in table 3.1. Patients were 46 to 68 years old (median: 59 years). FDG-tumour volumes ranged from 32.4 to 287.6 cm^3 with a median volume of 114.5 cm^3. Overall, 7 of the 15 patients had local recurrences. All observed failures occurred in the first 8 months after the end of therapy.

Table 3.2 contains an overview of the image data that were available for each patient. In total, for 11 of the 15 patients, pretreatment FDG data were acquired, whereas only 10 out of 15 were examined with one or more dynamic follow-up PETs during the course of therapy. For 13 patients of this group, CT data with contoured regions of interest were available.

Patients						
Pat. nr.	prim. tumour site	age	sex	TNM stage	tumour volume V [cm^3]	failure site
1	oropharynx	60	m	T4 N2b M0	258.1	T*/N†
2	oropharynx	51	m	T4 N2c M0	126.2	T*
3	larynx	66	m	T4 N2c M0	153.7	T*/N†
4	FOM‡	46	m	T3 N2b M0	59.0	T*
5	BOT§	49	m	T4 N2c M0	287.6	T*/N†
6	oropharynx	48	m	T2 N2c M0	114.7	T*/N†
7	FOM‡	68	m	T4 N1 M0	213.7	T*/N†
8	oropharynx	65	m	T3 N2c M0	74.3	-
9	hypopharynx/ BOT§	51	m	T4 N2c M0	100.9	-
10	oropharynx	59	m	T2 N3 M0	172.4	-
11	oropharynx	50	f	T4 N2c M0	44.0	-
12	larynx-/ hypopharynx	60	m	T4 N0 M0	32.4	-
13	oro-/ hypopharynx	49	m	T3 N2c M0	80.9	-
14	oropharynx	60	f	T4 N2b M0	52.4	-
15	unknown	68	m	T4 N1 M0	125.5	-

Table 3.1: Tumor characteristics of the examined patients.
*T: tumour; †N: node. ‡FOM: floor of mouth; §BOT: base of tongue.

Pat. #	dyn. FMISO pre-treatment	FDG pre-treatment	planning CT + ROIs*	dyn. FMISO follow-up @ 2 weeks	dyn. FMISO add.follow-up scans
1	×	×	×	×	-
2	×	-	-	×	-
3	×	×	×	×	-
4	×	-	-	×	-
5	×	-	×	-	-
6	×	×	×	×	×
7	×	×	×	×	-
8	×	×	×	-	-
9	×	×	×	×	-
10	×	×	×	×	-
11	×	×	×	-	-
12	×	×	×	-	-
13	×	×	×	×	×
14	×	-	×	×	-
15	×	×	×	-	-

Table 3.2: List of image data available for each of the 15 patients. *ROIs: regions of interest.

Dynamic FMISO Patient Scans

For the dynamic FMISO examination, the following protocol was used: With the start of the image acquisition, a tracer activity of $A_0 \simeq 400$ MBq FMISO was injected. For the first $15 - 60$ min, the PET scanner (Millennium VG, General Electric, Milwaukee, US) was running in dynamic acquisition mode which resulted in a total of $31 - 40$ image frames. Additionally, two static images were taken for all patients 2 and 4 h pi and for a few patients also at 3 h post injection (pi). Detailed information about time points and corresponding acquisition durations for each examined patient ($n = 15$) are summarized in table 3.3.

A decay correction for the decomposition of the radioactive ^{18}F was performed for all data sets. The raw PET data was stored in three separate data sets, one dynamic set consisting of 31 image frames and two static data sets with one frame each. In order to implement a pointwise hypoxia analysis, it was necessary to match these three data sets. The corresponding rigid body transformation matrix was calculated by applying a Mutual Information algorithm [68]. This matching procedure reached an accuracy ≤ 2 mm in the

time pi [min]	$0-2$	$2-4$	$4-15$	$15-60$	120	180	240
acquisition time [min]	$12\times$ 0.167	$8\times$ 0.25	$11\times$ 1	$9\times$ 5	$1\times$ 5	$1\times$ $8-9$	$1\times$ $10-12$
Patient #							
1, 4	×	×	×	×	×	×	×
3, 5, 7, 9, 10, 11, 12, 14	×	×	×	−	×	−	×
8	×	×	×	−	×	×	×
15	×	×	×	×	×	−	×
2, 13	×	×	×	$3\times$ 5 min	×	−	×
6	×	×	×	$5\times$ 5 min	×	−	×

Table 3.3: Table of acquired image frames for each patient ($n = 15$)

region of the tumour and allowed us to determine a TAC for each voxel.

FDG PET

Whenever possible ($n = 12$), an additional [^{18}F]-fluorodeoxyglucose (FDG) PET was taken a few days ($1-3$) before or after the FMISO PET scan. Concerning the FDG PET acquisition, a static emission scan was taken 1 h after injection of approximately 400 MBq FDG.

Follow-up FMISO Examinations

A subgroup of 10 patients received repeat scans after approximately 2 weeks of treatment (≈ 20 Gy). For a total of eight patients (# 1-5, 7, 9, 10 and 14), one FMISO repeat scan is available, whereas for two patients (# 6 and 13), three repeat scans could be acquired. Patient 6 had follow-up scans after 20, 50 and 70 Gy, patient 13 after 10, 20 and 50 Gy. The secondary FMISO PET scans were also acquired using dynamic acquisition mode. The long acquisition times made it difficult to organize the trial and put a large burden on the patients who were suffering from acute reactions during therapy.

3.3.2 Tumour Volume Delineation

For the delineation of the tumour volume relevant in the context of this study, the FDG PET image data was used. The tumour volume was defined as the

volume including all voxels with at least 40% of the maximum intensity. This delineation technique was combined with a 12 mm margin (3 PET voxels). The tumour volume variable V used in the current study refers to the described FDG PET volume. It is determined as $V = n \cdot v$, where n is the number of tumour voxels. v represents the volume of a single voxel, in our case $v = (0.4^2 \cdot 0.425)$ cm^3 $= 0.068$ cm^3. In order to match the FDG-defined tumour volume onto the three different FMISO data sets (dynamic, 2 and 4 h pi), automatic MI coregistration [68] was performed.

3.3.3 Treatment

All patients were treated with primary RT to 70 Gy. Three of these patients were treated with Intensity Modulated Radiotherapy (IMRT) in 35 fractions, 5 fractions a week with a daily dose of 2 Gy. The other 12 patients received conventional RT, 5 fractions with 2 Gy per week until 30 Gy. This first phase was followed by a hyperfractionation composed of a dose of 1.4 Gy applicated twice per day until the end of treatment. In addition, concomitant chemotherapy was prescribed for 14 patients. Seven patients received 5-Fluorouracil/Mitomycin chemotherapy, whereas for six patients Cisplatin/Mitomycin was prescribed; one patient had Paclitaxel/Cisplatin chemotherapy.

3.3.4 Therapy Outcome

After the end of therapy, patients were reviewed regularly every three months with clinical examination, flexible endoscopy and computed tomography (CT) when recurrent disease was suspected. Routine CT scans were also acquired six weeks and one year after therapy was finished. Failure was defined as CT proven tumour progression. For the examined patient group, the follow up time was in the range of $2 - 21$ months (median: 12.8 months).

Chapter 4

A new Approach to Molecular Image Guided Radiotherapy

Four main steps were developed during this PhD project in order to create the link from functional imaging data to an individually adapted and targeted RT treatment. In the following, the four different issues that have to be addressed to determine a complete junction from molecular imaging to functional image guided radiotherapy (f-IGRT) are discussed in more detail. Figure 4.1 schematically shows the junction between functional imaging and an adapted radiotherapy.

1. A physical model that describes the transport of oxygen and nutrients in a tissue is used in order to interpret the internal structural properties of a human tumour. It is well known [21], that a lack of oxygen, which may result from a chaotic structural architecture of a tumour causes increased radioresistance. A non-invasive measurement of tumour hypoxia in humans can be obtained via dynamic positron emission tomography with the hypoxia-sensitive bio-marker F-MISO. In a first step (chapter 5), a physical transport model is developed which allows for the analysis of the uptake and distribution of the hypoxia PET tracer FMISO. The model is derived from the general Diffusion-Reaction-Equation. A Levenberg-Marquardt-algorithm is then used to fit the analytical tracer transport functions to the measurend data curves. A number of different model parameters can be determined from a fit of the model to the data curves which enable for the estimation of various functional parameters of the tumour. Thus, the model allows us to draw conclusions about the characteristic functional architecture of the underlying tumour tissue.

2. In a second step (chapter 6), a statistical analysis is carried out in order

to identify the main kinetic parameters which are relevant for therapy success. To reach this goal, parameters deduced from the kinetic analysis were compared to other relevant tumour parameters. Based on findings about pridictive variables assessed by the transport model, characteristic patterns of two important parameters are investigated. Furthermore, a statistical analysis is performed in order to correlate these model parameters to RT treatment outcome.

3. The translation of functional imaging data into an individual prescription for RT can only be performed by a model that is capable of predicting the probability of therapy success for a patient as a function of the molecular imaging data. In chapter 7, a tumour control probability (TCP) model is introduced. The design of the model is based on characteristic changes in the functional imaging data during the course of RT treatment. This model involves characteristic values derived from the dynamic FMISO PET data. It allows us to estimate the time a tumour needs until reoxygenation occurs. In addition, the model is calibrated by a log-likelihood fit to the binary therapy outcome data of a group of 15 patients.

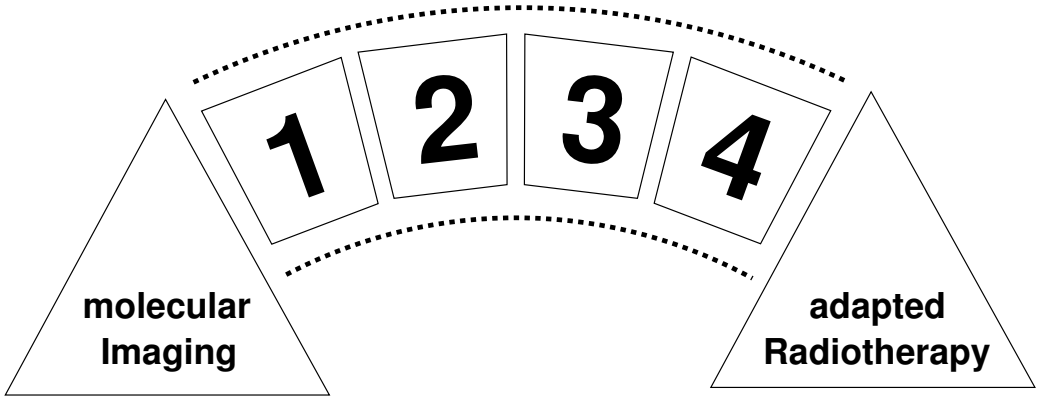

Figure 4.1: Schematical representation of the four main steps developed in this PhD project which are necessary to create a complete link between molecular imaging and a biologically adapted radiotherapy.

4. The TCP model introduced in step three allows for individual and spatially varying dose prescriptions for RT treatment planning. Step four (chapter 8) consists of a treatment planning study where two different approaches of targeted RT techniques are compared. The first approach increases the dose uniformly to a biological target volume that is delineated on the basis of the intensity distribution of a static PET image. In contrast, the second set of plans applies spatially variant doses according to the requirements of the dynamic FMISO PET images. A group of 13 patients was included into this planning study. The feasibility of individually adapted RT methods in a clinical setting were evaluated. The estimation of the potential gain of treatment success for a patient population was ad additional goal of the study.

Chapter 5

Step I: Tracer Transport Modelling

5.1 General Transport Characteristics in Tumour Tissues

As the transport of the FMISO tracer in the tumour tissue can be assumed to be of purely diffusive nature, in the following, the general Diffusion-Reaction-Equation (DRE) which should be used to describe the phenomenon mathematically is introduced. The diffusion equation cannot be solved for the realistic problem because of lacking knowledge about the tumour geometry. One measurement that is possible in the case of cancer patients is PET, where the signal is the bulk-averaged concentration of the tracer in 4 mm voxels, whereas the length scales of the tissue structures is in the order of 10 μm. Hence, the exact DRE cannot be solved accurately, but the general DRE and the corresponding solution may be useful to analyze the nature of the tracer transport phenomenon and to make an educated guess for the solution.

Furthermore, a kinetic compartment model is presented to investigate uptake and binding properties of FMISO in human tumours. The kinetic model assumes physical, purely diffusive transport of the tracer molecule to the hypoxic cell, where it is trapped according to the local oxygen tension. This simplified transport model is used to describe the tracer transport in the tumour tissue and to interpret the signal $S(t)$ acquired during PET examination. In addition, the investigated model is fitted to voxel-based TAC acquired from dynamic FMISO PET patient data.

5.1.1 Outline of the Approach

The tracer diffusion problem is intractable because of the geometry of the tumour in a patient is unknown (see also figure 2.1). Furthermore, all non-invasive patient measurements have spatial resolutions that are much larger than the length scale of the tissue structures. Therefore, the exact DRE can neither be established correctly nor solved accurately, due to structural heterogeneities of the cancer tissue. These structural heterogeneities in the tissue correspond to a spatial distribution of sources and sinks, which are expressed by inhomogeneities and boundary conditions of the DRE. Moreover, also the diffusion coefficients in the tissue will be a heterogeneous, their values are spatially varying.

In section 5.1.3, the one dimensional solution of the general DRE is determined. The mathematical form and nature of the solution may be useful to characterize the tracer transport problem. Typical elements of the solution are identified in order to make an educated guess for the solution in a bulk approximation. The one dimensional solution of the DRE constitutes an important link to be able to understand and analyze the bulk-averaged concentration of the tracer imaged with PET.

Finally, the spatial dependencies included in the DRE will be collapsed into a kinetic compartment model. This kinetic model contains solely temporal dependencies and can be applied to analyze the PET signal with a spatial resolution of 4 mm.

5.1.2 Diffusion-Reaction-Equation

The general 3-dimensional DRE emerges from the 1^{st} and 2^{nd} Fick's law [61], which describe mass transport on the basis of concentration differences. Fick's first law reads

$$\frac{\partial}{\partial t}\, N(\vec{x},t) = -D\; A\; \text{grad}\; n(\vec{x},t) \quad , \tag{5.1}$$

where N is the number of particles, A the surface area over which diffusion takes place, D is the diffusion coefficient (in $[m^2/s]$) and n the concentration. Considering the diffusion flux $\vec{j}$

$$\vec{j}(\vec{x},t) = \frac{1}{A}\frac{\partial}{\partial t}\, N(\vec{x},t) \quad , \tag{5.2}$$

Fick's first law reads

$$\vec{j}(\vec{x},t) = -D\; \text{grad}\; n(\vec{x},t) \quad . \tag{5.3}$$

Fick's second law, the continuity equation, describes the relationship between diffusion flux and particle density:

$$\frac{\partial}{\partial t}\, n(\vec{x},t) + \text{div}\ \vec{j}(\vec{x},t) = q(\vec{x}) \quad , \tag{5.4}$$

where $q(\vec{x})$ represents the change of the total number of particles, i.e. the change of a chemical potential or also a chemical reaction. Therefore, the DRE can be written in the form

$$\frac{\partial}{\partial t}\, n(\vec{x},t) = D\ \Delta n(\vec{x},t) + q(\vec{x}) \quad . \tag{5.5}$$

Here, Δ is the Laplace operator.

5.1.3 1-D Solution of the Diffusion-Reaction-Equation

In the following section, a solution for the one-dimensional DRE

$$\frac{\partial}{\partial t}\, n(x,t) = D\ \frac{\partial^2}{\partial x^2}\, n(x,t) + q(x,t) \tag{5.6}$$

is presented, where $q(x,t)$ is the reaction term. The initial and boundary conditions are given by

$$n(x,0) = f(x) \qquad \text{and} \qquad \lim_{x\to\infty} n(x,t) = 0 \quad . \tag{5.7}$$

Separation of the variables is one possible method to solve the homogeneous differential equation of (5.6) ($q(x,t) = 0$)) [10,46,47]. This approach assumes

$$n(x,t) = X(x)T(t) \tag{5.8}$$

and leads to

$$\frac{\dot{T}}{DT} = \frac{X''}{X} = const = -\lambda^2 \quad . \tag{5.9}$$

As the left part of equation (5.9) does no longer depend on x and the right side does not depend on t any more, each term has to be constant. The constant is chosen to be negative, because otherwise the boundary condition cannot be fulfilled. The following two linear differential equations can be derived from equation (5.9):

$$X'' + \lambda^2 X = 0 \tag{5.10}$$

$$\dot{T} + D\lambda^2 T = 0 \quad . \tag{5.11}$$

A combination of the solutions for $X(x)$ and $T(t)$ leads to the basic solutions of the homogeneous diffusion equation

$$n(x,t,\lambda) = e^{-D\lambda^2 t}\ [a(\lambda)\cos(\lambda x) + b(\lambda)\sin(\lambda x)] \tag{5.12}$$

with arbitrary functions $a(\lambda), b(\lambda), \lambda \in \mathbf{R}$. Continuous superposition is then used to determine the general solution $n(x,t)$:

$$n(x,t) = \int_{-\infty}^{\infty} e^{-D\lambda^2 t}\ [a(\lambda)\cos(\lambda x) + b(\lambda)\sin(\lambda x)]\ d\lambda \quad . \tag{5.13}$$

For the given initial condition, one obtains

$$f(x) = n(x,0) = \int_{-\infty}^{\infty} [a(\lambda)\cos(\lambda x) + b(\lambda)\sin(\lambda x)]\ d\lambda \quad . \tag{5.14}$$

A comparison with the representation of the *Fourier integral*, allows to derive

$$a(\lambda) \;=\; \frac{1}{2\pi}\int_{-\infty}^{\infty} f(\xi)\cos(\lambda\xi)d\xi \tag{5.15}$$

$$b(\lambda) \;=\; \frac{1}{2\pi}\int_{-\infty}^{\infty} f(\xi)\sin(\lambda\xi)d\xi \quad , \tag{5.16}$$

which, reinserted into equation (5.13), yields

$$n(x,t) = \frac{1}{2\pi}\int_{-\infty}^{\infty} f(\xi)\Big[\int_{-\infty}^{\infty} e^{-D\lambda^2 t}[\cos(\lambda\xi)\cos(\lambda x) + \sin(\lambda\xi)\sin(\lambda x)]d\lambda\Big]d\xi \quad . \tag{5.17}$$

The integration with respect to λ leads to the general homogeneous solution for $n(x,t)$:

$$n(x,t) = \frac{1}{2\sqrt{D\pi t}}\int_{-\infty}^{\infty} f(\xi)\ e^{-\frac{(x-\xi)^2}{4Dt}}d\xi \quad . \tag{5.18}$$

To obtain the solution for the inhomogeneous differential equation (5.6), the following term for the particular solution $n_p(x,t)$ of (5.6) has to be added to the homogeneous solution (5.18):

$$n_p(x,t) = \int_0^t \Big[\int_{-\infty}^{\infty} \frac{q(\xi)}{2\sqrt{D\pi(t-\tau)}}\ e^{-\frac{(x-\xi)^2}{4D(t-\tau)}}d\xi\Big]d\tau \quad . \tag{5.19}$$

The one dimensional solution of the general DRE (5.18) presents a number of characteristics which may be of importance for the design of a compartment model to analyze bulk diffusion data acquired with PET on larger length scales. If a δ-function is used as initial condition $f(x) = \delta(x_0)$, the solution turns out the be a propagating concentration front/wave of tracer with increasing distance to x_0. Width and amplitude of this propagating tracer front change with space and time. In a human tumour, the exact geometry of the tissue, where the diffusion takes place is unknown and only measurement data are available that show bulk averaged concentrations in 4 mm PET voxels. In principal, one could assume the concentration in each voxel to be constant and consider only the diffusion process through the surface of each voxel. But still, the boundary conditions for each voxel would be unknown.

Therefore, the development of a bulk diffusion model is proposed. The solution of the general DRE in one dimension (5.18) as well as the time dependence revealed by equation (5.11) will be used as a basis for the design of a compartment model in the following section.

5.2 Development of a Compartment Model

Although the diffusive transport of FMISO in the tumour depends crucially on the tissue geometry, blood vessel permeability and the interstitial flow and pressure situation, which are obviously unknown, the bulk diffusion equation (without spatial dependencies) for a net flow from a point A to a point B reads schematically:

$$\frac{\partial}{\partial t} C_B = \frac{D}{l^2} \left(C_A(t) - C_B \right) \quad . \tag{5.20}$$

Here D is the diffusion constant, l the distance between points A and B, and $C_A(t)$ is assumed to be unaffected by the efflux (infinite supply). The linearity of the diffusion equation allows us to associate spatially separated sub-volumes with compartments and an approximate linear reaction rate equation. For a compartmental model, the consequence of this diffusion delay will be a translation of the spatial separation of blood pool and tracer trapping into a temporal separation [23]. With D typically in the order of 10^{-6} cm^2 s^{-1}, and $l \simeq 0.01$ cm it follows that $k \simeq 10^{-2}$ s^{-1}, i.e. typical time scales are > 100 s.

Regarding the design of a kinetic model, it is assumed that for all practical purposes a general two compartment model (see figure 5.1) will be sufficient

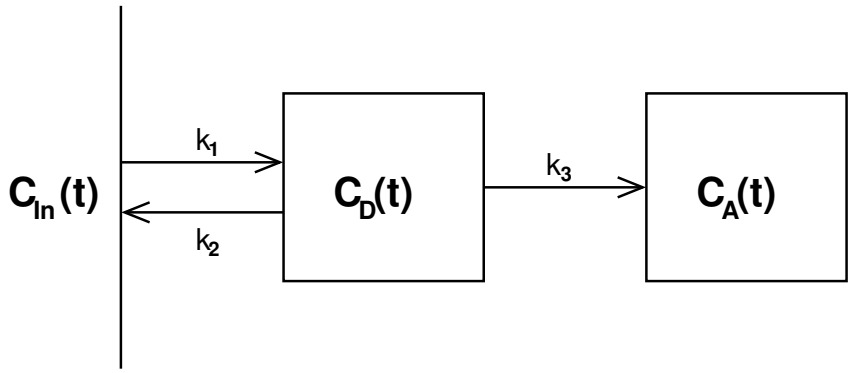

Figure 5.1: Compartmental model consisting of a diffusive and an accumulative compartment. The input function $C_{In}(t)$ comprises the tracer concentration in the blood and in the interstitial space close to the vessels.

to describe the dynamic FMISO data[1]. The model can be motivated by the heuristics that there are essentially three distinguishable components of the TACs. One, showing rapid concentration changes due to perfusion and fast diffusion into the interstitial space close to the vessels, represented by the input function. Another, characterized by slow concentration changes due to long diffusion times to and from the large inter-vessel spaces of irregular tumours. And a third, describing the irreversible binding of the tracer. In the following, the compartment describing the freely diffusive tracer molecules will be referred to as *diffusive* compartment. The *accumulative* compartment is linked to the diffusive compartment by a kinetic rate constant that depends on the partial oxygen pressure.

In contrast to classic compartmental models, the compartments in this model are spatially separated or overlap only partially (the accumulative compartment corresponds only to those sub-volumes described by the diffusive compartment which are hypoxic) and the volumes of the different compartments are not identical. In addition, some of the kinetic constants of this model are not parameters of a chemical reaction, but reflect purely diffusive transport.

The diffusive compartment is linked to the input function by diffusion rate constants k_1 and k_2. The accumulative part is only coupled to the diffusive one with the rate constant k_3. It is assumed that the diffusion of unbound re-

[1]This is a consequence of the integration of the manifold of various TACs of all the particular sub-volumes in a PET voxel. If tumours were more homogeneous or the spatial resolution of the scanner better, a chain of compartment pairs, stratified according to their diffusion time, might be a more appropriate model.

duced FMISO cannot be discerned on the time scales of the experiment. This kinetic model is described by the following system of differential equations:

$$\frac{\partial}{\partial t} C_D(t) = k_1 C_{In}(t) - (k_2 + k_3) C_D(t) \tag{5.21}$$

$$\frac{\partial}{\partial t} C_A(t) = k_3 C_D(t) \quad . \tag{5.22}$$

$C_D(t)$ and $C_A(t)$ are the basis functions for the diffusive and the accumulative compartment respectively. They are determined by

$$C_D(t) = e^{-(k_2+k_3)t} \otimes k_1 C_{In}(t) \tag{5.23}$$

$$= k_1 \int_0^t e^{-(k_2+k_3)(t-\tau)} \cdot C_{In}(\tau)\, d\tau \qquad \text{and}$$

$$C_A(t) = k_3 \otimes C_D(t) \tag{5.24}$$

$$= \frac{k_1 k_3}{k_2 + k_3} \int_0^t (1 - e^{-(k_2+k_3)(t-\tau)}) \cdot C_{In}(\tau)\, d\tau \quad ,$$

where the k_i are the respective rate constants and $\otimes$ denotes the convolution product. The measured PET signal $S(t)$ is given by a linear combination of the basis functions (eq. 5.23 and 5.24) and the input function $C_{In}(t)$:

$$S(t) = w_0 C_{In}(t) + w_D C_D(t) + w_A C_A(t) \tag{5.25}$$

$$= w_0 C_{In}(t) + w_D k_1 \int_0^t e^{-(k_2+k_3)(t-\tau)} \cdot C_{In}(\tau)\, d\tau$$

$$+ w_A \frac{k_1 k_3}{k_2 + k_3} \int_0^t (1 - e^{-(k_2+k_3)(t-\tau)}) \cdot C_{In}(\tau)\, d\tau.$$

Here w_D and w_A are the relative weights of the compartments. They represent the relative contribution of each compartment to the total signal. The weight parameters are difficult to normalize, as overlapping areas are possible.

In the complete expression for the total signal $S(t)$ (5.25), the rate constant k_1 turns out to be only a multiplicative factor to the weight parameters w_D and w_A. It can therefore be set constant without loss of generality. Variations of this parameter are absorbed in $\tilde{w}_D = w_D k_1$ and $\tilde{w}_A$. Additionally, the rate constant k_2 can be absorbed by substituting $\tilde{k}_3 = k_2 + k_3$ and

$\tilde{w}_A = w_A\ k_1\ k_3/\tilde{k}_3$. The final equation for the PET signal reads

$$\begin{aligned} S(t) &= w_0 C_{In}(t) + \tilde{w}_D \int_0^t e^{-\tilde{k}_3(t-\tau)} \cdot C_{In}(\tau)\ d\tau \\ &\quad + \tilde{w}_A \int_0^t (1 - e^{-\tilde{k}_3(t-\tau)}) \cdot C_{In}(\tau)\ d\tau \quad . \end{aligned} \tag{5.26}$$

The remaining kinetic model has 4 open parameters, the weight parameters $w_0, \tilde{w}_D$ and $\tilde{w}_A$ in addition to the modified accumulation rate constant $\tilde{k}_3$. This parametrization was chosen such that three different modes can be distinguished. Only one mode (w_D) is chosen to be constant. This specific choice allows a stable fit with small covariants.

5.2.1 Input Function

For head and neck cases, it is difficult to obtain the blood input function directly from the images. Therefore, we propose the use of a reference tissue model.

One might also take a measured arterial blood input function. Such a measured input function would contain the pure blood signal, whereas a 'dressed' input function, determined by a reference tissue model has the advantage to account for the varying tissue composition of the respective voxel. A pure blood function may be problematic as the flow into the considered voxel can be completely different of the measured function due to highly deficient and irregular vascular systems of tumours. The 'dressed' input function comprises not only the tracer concentration in the blood, but also the concentration in a number of cell layers close to the vessels which are fast coupled. Hence, a dressed input function consists of two different parts: The blood vessels plus a certain volume of extravascular, extracellular space. The two components will have individual weight parameters which allows us to account for the varying composition of vessels and extravascular space in the tissue from voxel to voxel.

Normal tissues can be described by a kinetic model consisting of the blood concentration $C_{In}(t)$ and a tightly coupled diffusive compartment, see figure 5.2. The tracer concentration in the cell layers around a blood vessel (i.e. the diffusive compartment of the normal tissue model) is denoted with $C_{NT}(t)$. Therefore, the input function may be extracted from typical normal tissue voxels.

During the first minutes after injection, the image signal is governed by diffusion from well perfused capillaries into the interstitial space. This will

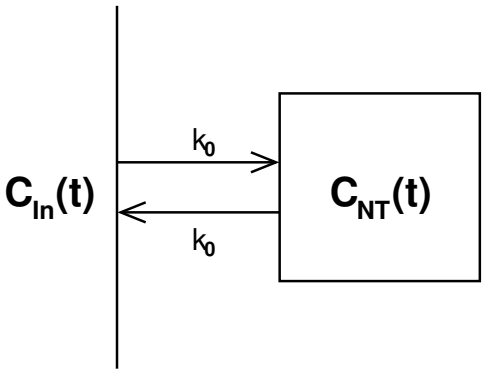

Figure 5.2: Reference tissue compartment.

occur in a similar fashion in both normal tissue and tumour tissue, although the deficient vasculature in tumours may offer less resistance. In this case, k_1 and k_2 of the tumour would be greater than in the reference tissue, but this does not affect the input function, which should be the same as long as the tracer transition from the vessel into the interstitial space is permeability limited and not flow limited. Apart from this difference in kinetic parameters, well perfused tumour areas and normal tissues should behave similarly during the first minutes after injection. This assumption is corroborated by immunohistochemical investigations [30, 31, 41] that showed that cells situated in the neighbourhood of a blood vessel under well oxygenated conditions exist in both hypoxic and non-hypoxic tumours.

However, these investigations also show badly perfused vessels. Also, temporary stasis has been described in tumours [17]. This means, that the well perfused vasculature which becomes visible in the first minutes after injection may not be the entire vasculature available for tracer transport by flow during the course of the investigation. Frequently, the distinction between chronic and acute hypoxia is made. The effect of fluctuations in the perfusion of a voxel on the TAC depend on the time scale of these fluctuations relative to the diffusion time scale, and the partial volume of the voxel affected by them. In our model, this is approximately taken into account by a spatially dependent input function as follows.

A dressing of the input function accounts for the fact, that the geometry of volumes that are quickly reached after tracer injection can be very different from voxel to voxel. We assume, that the input function to the tumour kinetic model $C_{In}(t)$ can be derived from the signal of a reference tissue

$$S_{NT}(t) = A \cdot C_{In}(t) + B \cdot C_{NT}(t) \quad . \tag{5.27}$$

We assume further that the blood concentration after a certain time after injection is a sum of two exponentials:

$$C_{In} = A \cdot (e^{-k_0 t} + r \cdot e^{-k_K t}) \quad . \tag{5.28}$$

The first term $e^{-k_0 t}$ describes the dispersion of the tracer in the whole body blood volume, i.e. the rate with which the equilibrium is established, whereas the second exponential represents the kidney clearance of the tracer. The rapid rise of tracer concentration in the blood pool observed in the very early frames is not taken into account by this input function. Therefore, the first frames (typically 4-5) have to be ignored for data analysis.

The concentration in the extravascular normal tissue space obtains from a convolution

$$C_{NT}(t) = C_{In}(t) \otimes e^{-k_0 t} \quad . \tag{5.29}$$

Here, we assume that the diffusion rate constant k_0 equals the mean rate of tracer flux into the extravascular volume, averaged over the whole body.

The signal measured in a reference tissue voxel $S_{NT}(t)$ will be of the form

$$S_{NT}(t) = A \cdot (e^{-k_0 t} + r \cdot e^{-k_K t}) + B \cdot C_{NT}(t) \quad . \tag{5.30}$$

The parameters k_0 and k_K are determined by fitting this expression (5.30) to a set of TACs from a reference tissue in close proximity of the tumour. For the input function of a tumour voxel, these parameters are kept constant while r remains floating. This allows us to adapt the ratio between the fast and the slow component of the input function to the local properties of the tumour vasculature and perfusion, and to some extent to their temporal variability. The number of parameters in the fit of the voxel-by-voxel TACs to the compartment model (eq. (5.26)) thereby increases to five.

5.2.2 Parameter Plots

Parameter plots can be used in order to visualize the voxel-by-voxel results of the compartmental analysis. To achieve this, an image is generated, where each voxel is coloured according to the value of the respective parameter. A specific parameter plot is used in the context of this study, where the tracer uptake at infinite times S_∞ is considered:

$$S_\infty = \lim_{t \to \infty} S(t) = \alpha \tilde{w}_A, \tag{5.31}$$

where $\alpha = A(1/k_0 + r/k_K)$. This derived parameter represents an estimate of the pure tracer uptake, when all unbound tracer molecules are washed out. High image intensities in those parameter plots represent areas with high levels of tracer uptake which correlates to the mean density of viable hypoxic cells in the respective voxel.

5.3 Data Evaluation

In order to evaluate the time-activity data with the presented kinetic model, a least squares fit was performed to adjust the analytical function $S(t)$ (5.25) to the patient TACs. For this, a Levenberg-Marquardt algorithm was used [54].

The data points were included into the proximity function with errors corresponding to Poissonian noise. Standard deviations σ_i were calculated as scaled Poissonian noise, depending on local count rate $Y_i(t)$ and acquisition time T_i for the respective frame.

Additional uncertainties may occur due to image coregistration errors. As only the late data sets ($2-4$ h pi) undergo a matching procedure, additional errors have only to be taken into account for the late data points. The magnitude of the individual error associated to each image voxel depends strongly on the image gradient in the considered region. Hence, the error due to an eventual mismatch ΔY_{MM} can be estimated by

$$\Delta Y_{MM} = \Delta x \cdot \left(\sum_{i=1}^{n} \frac{(Y - Y_i)^2}{n \cdot x_i} \right)^{1/2}, \tag{5.32}$$

where Y_i are the count rates of the n neighbour voxels, x_i is the distance to the respective neighbour voxel and Δx represents the average co-registration error, which is assumed to be approximately 2 mm in our case. The total error associated to data points $2, 3$ and 4 h pi is determined by $\Delta Y_i^{tot} = \sigma_i Y_i + \Delta Y_{MM}$.

The variability of the model parameters due to the estimated data errors is then determined by the variance-covariance matrix associated to the least squares fit [54]. The diagonal matrix elements represent estimates of the respective parameter variances. In addition, a parameter correlations $\rho_{i,j}$ can be derived from the covariance matrix for each fit according to

$$\rho_{i,j} = \frac{Cov(X_i, X_j)}{\sqrt{Var(X_i) \cdot Var(X_j)}} \tag{5.33}$$

where $Cov(X_i, X_j)$ is the covariance between parameters X_i and X_j and $Var(X_i)$ is the variance of the i-th fit-parameter.

In addition, the continuous automatic tracer injection during the first 10 s after the start of the acquisition is not taken into account by the model. To avoid problems, the very steep and slightly oscillating component dominating all data curves during the first 60 seconds was omitted.

5.4 Results of the Kinetic Analysis

The TACs observed in a group of 15 examined patients showed great variability. In figure 5.3, four examples of characteristic shapes of the acquired time-activity data are displayed.

In well perfused regions[2], the shapes of the curves have a very pronounced tracer influx and distribution during the first few minutes after tracer injection followed by an exponential washout (see figure 5.3(a)). These tumour areas are characterized by a high density of vessels and a good blood supply. The majority of cells should be well oxygenated because no tracer retention can be seen.

In figure 5.3(b), a very similar behaviour can be observed during the first 30 minutes, followed by a clear retention. This shows that a large number of viable hypoxic cells is present, which co-exist with a very well perfused cell population. This is the classical picture of diffusion limited hypoxia, where oxygen consumption outweighs supply.

More serious forms of hypoxia result from a deficient vasculature and chaotic blood flow. However, this may also result in a decrease of viable hypoxic cells as necrotic cores may form in which no tracer retention occurs. In terms of the TAC, the perfusion peak should become smaller, and retention less pronounced until finally a horizontal curve type results, see figure 5.3(c) and figure 5.3(d). In voxels with a significant concentration of necrosis, the purely diffusive contribution to the signal as represented by $\tilde{w}_D$ and r should go up. The tracer enters these tissue regions very slowly due to the low density of blood vessels. Accumulation of tracer can be observed in the order of several hours after injection (see figure 5.3(d)). Because of the small fraction of viable hypoxic cells, the total uptake is low.

Figure 5.4 shows the analytical curves $S(t)$ determined by the kinetic analysis for the data TACs presented in figure 5.3. The corresponding parameter values are summarized in table 5.1, whereas table 5.2 shows the corresponding parameter value uncertainties. In figure 5.5, the decompositions of the model curves into the three components $C_D(t), C_A(t)$ and $C_{In}(t)$ of the compartment model are shown. Additionally, for the correlation matrix

[2]Good perfusion/high vascular density is supposed in regions where the dynamic TAC presents a fast tracer influx after injection ($\approx 30 - 40$ s).

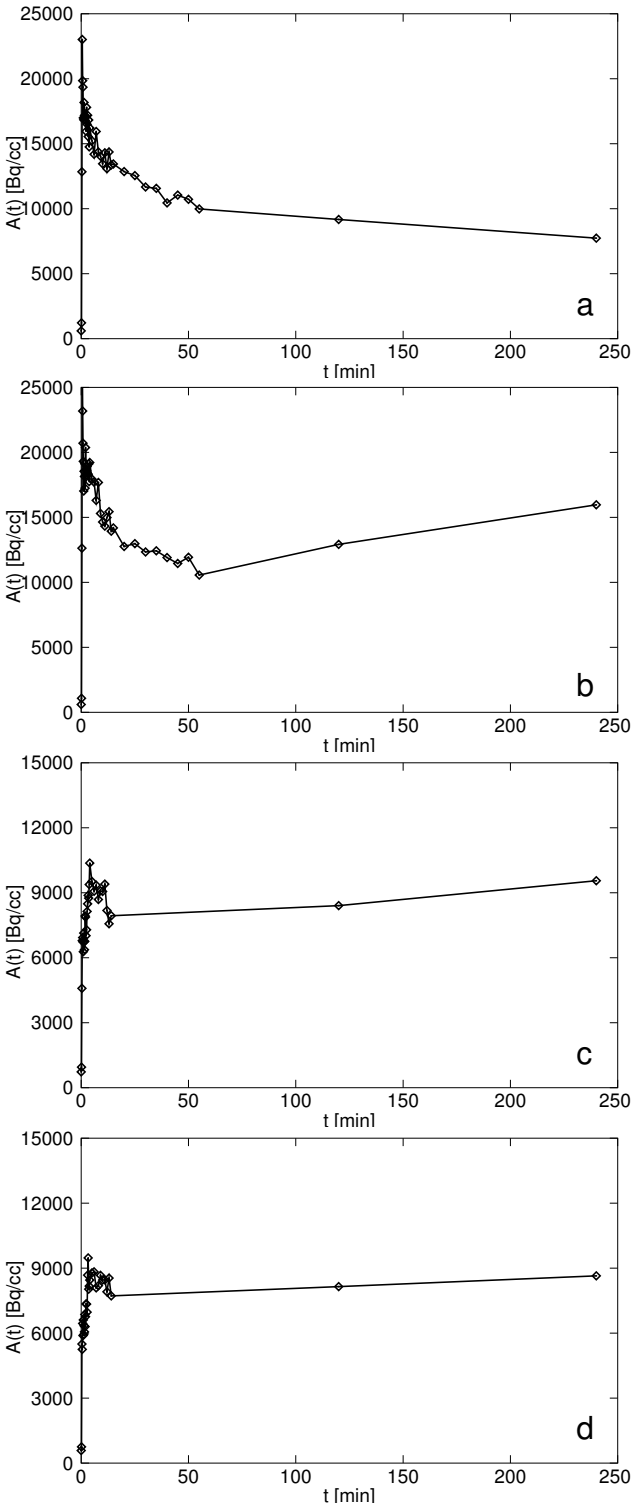

Figure 5.3: Different characteristic time-activity data curves corresponding to tumour areas with increasingly deficient vasculature. (a) Well perfused tumour area. (b) Tissue area with diffusion limited hypoxia. (c) Diffusion limited and structural hypoxia. (d) Hypoxic / necrotic area.

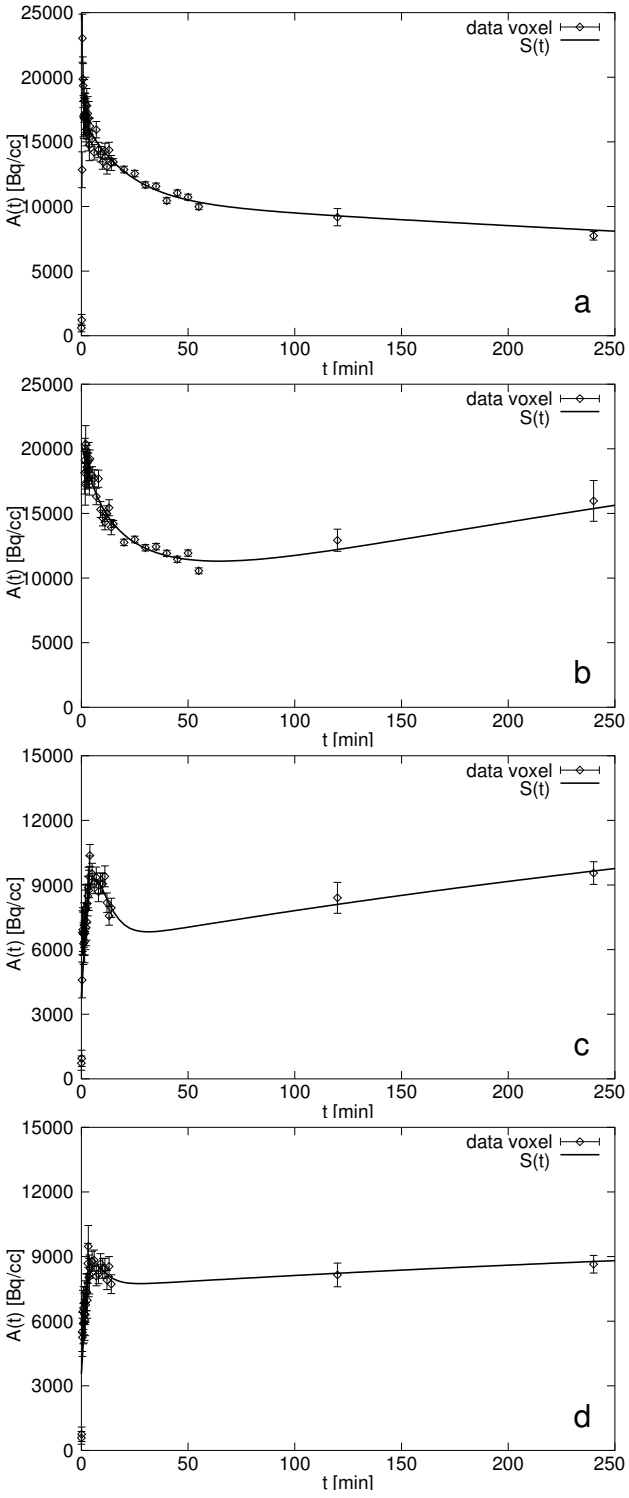

Figure 5.4: Resulting analytical time-activity curves corresponding to data curves (a)-(d) of figure 5.3.

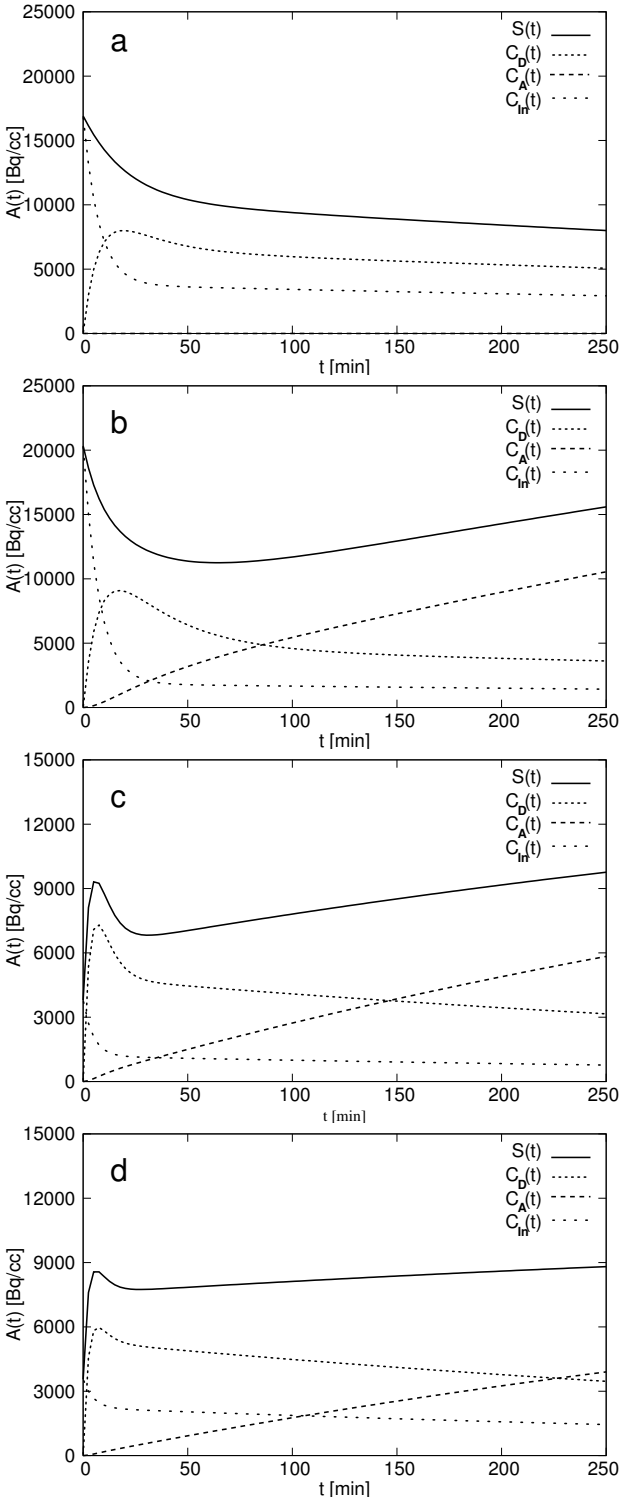

Figure 5.5: Decomposition of the analytical model curves (a)-(d) of figure 5.4 into the three different components of the compartment model.

of curve (c), the following values were calculated:

$$\mathbf{Corr} = \begin{pmatrix} 1 & -0.554 & 0.711 & -0.904 & -0.737 \\ -0.554 & 1 & 0.140 & -0.036 & -0.041 \\ 0.771 & 0.140 & 1 & -0.862 & -0.996 \\ -0.904 & -0.036 & -0.862 & 1 & 0.888 \\ -0.737 & -0.041 & -0.996 & 0.888 & 1 \end{pmatrix}$$

In summary, figure 5.3 (a)-(d) represent the TACs in tumour regions with increasingly deficient vasculature. The tracer influx peak at short time-points after injection decreases as the blood supply gets worse due to the more and more chaotic vasculature. At the same time, while the number of viable hypoxic cells decreases ($\tilde{w}_A$), the degree of hypoxia increases ($\tilde{k}_3$). This is illustrated by the decomposition of the model curves $S(t)$ into the components $C_D(t), C_A(t)$ and $C_{In}(t)$, represented in figure 5.5. Here, the contribution of the input function $C_{In}(t)$ decreases from curve (a) to (d), whereas the weight of the accumulative compartment increases from (a) to (d). The kinetic analysis showed that the resulting parameter values might reveal information about the structural architecture of the tissue sample. Curve types representing putatively well perfused and only slightly hypoxic tumours (such as figure 5.4(a)) are described by a relatively high weight parameter w_0 in addition to a small value for the product $\tilde{w}_A\tilde{k}_3$ for the hypoxic compartment. Also for the diffusion limited hypoxia type (figure 5.4(b)) a large w_0 is found, but in this case the value of $\tilde{w}_A$ and thus S_∞ is also high.

In contrast, there exist tumour areas where very small parameters w_0 are necessary to describe the time-activity course of the data adequately. This behaviour is mainly observed for curves that putatively represent severely

	putative structure types	w_0	r	$\tilde{w}_D$ $[min^{-1}]$	$\tilde{w}_A$ $[min^{-1}]$	$\tilde{k}_3$ $[min^{-1}]$
(a)	low hypoxia/ well perfused	1.06	0.29	0.09	0.00	0.05
(b)	diffusion limited hypoxia	1.50	0.10	0.13	0.31	0.03
(c)	diff. limited and structural hyp.	0.32	0.45	0.28	0.08	0.21
(d)	strongly hypoxic/ necrotic	0.16	1.67	0.14	0.01	0.36

Table 5.1: Resulting parameter values for curves (a) - (d), figure 5.4

	Δw_0	Δr	$\Delta\tilde{w}_D$ $[min^{-1}]$	$\Delta\tilde{w}_A$ $[min^{-1}]$	$\Delta\tilde{k}_3$ $[min^{-1}]$
(a)	0.17	0.17	0.02	0.00	0.02
(b)	0.18	0.11	0.02	0.11	0.02
(c)	0.16	0.39	0.06	0.08	0.11
(d)	0.18	1.86	0.07	0.01	0.25

Table 5.2: Errors of model parameters due to image noise and coregistration uncertainties associated to curves (a) - (d), figure 5.4

hypoxic or necrotic tissues (such as figures 5.4(c) and (d)). Hence, $\tilde{w}_A\tilde{k}_3$ turns out to take relatively high values.

In the following, the kinetic data analysis will be shown in more detail exemplarily for patients # 6 and 13. Figure 5.6(b) shows the S_∞ parameter plot of patient # 13 and figure 5.8(b) the one for patient # 6. Both hypoxia maps are displayed in comparison to the corresponding distributions of standardized uptake values (SUV) at 2 h pi (figures 5.6(a) and 5.8(a)).

Figure 5.6(b) represents a first example of a parametric plot for patient # 13. The region characterized by an increased SUV 2 h pi is also highlighted in the parametric plot. A typical TAC of this region is plotted in figure 5.7. The curve shows a relatively high influx peak as well as a positive slope for long times after injection.

In case of patient # 6, displayed in figure 5.8, the SUV image 2 h after injection indicates two distinct areas where the tracer seems to be accumulated (figure 5.8(a)). However, the parametric plot for the indicated region of interest only highlights one of these two regions (figure 5.8(b)). This phenomenon is due to a different overall shape of the curves in the respective tumour voxels and may be caused by different architectures of the tumour vascularization leading to different retention times for the tracer.

Voxels A and B were chosen as representatives for these two areas. The analytical curves $S(t)$ as well as the corresponding measured data points are displayed in figure 5.9. The plotted TACs present an interesting behaviour: Even though the two curves have nearly the same activity level 120 min after tracer injection, the shape of the curves is completely different. While the TAC for voxel A shows a very high tracer influx peak followed by a continuous washout, voxel B is characterized by a steady accumulation of tracer 30 to 240 min pi in addition to a much lower influx peak at the beginning. Hence, the impression that the static image 2 h after injection presented the same level of tracer accumulation was due to the fact that the intercept point of two absolutely different curves was situated coincidentally at the time of

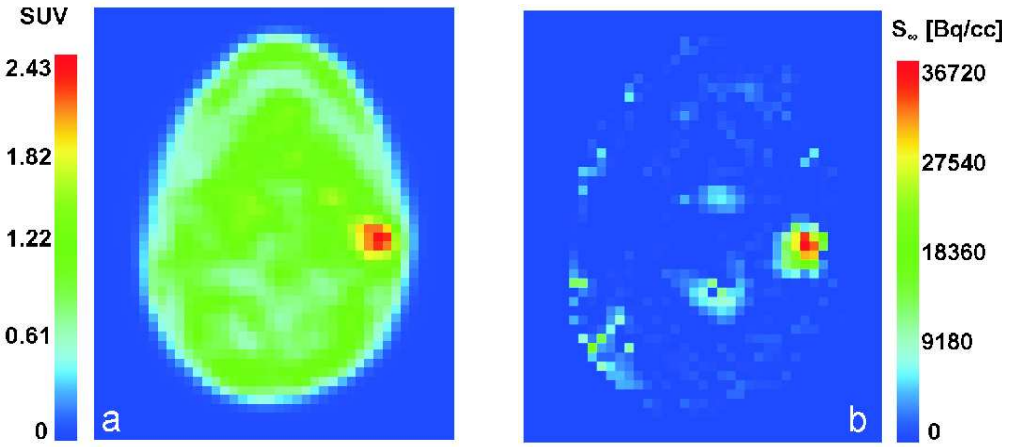

Figure 5.6: Tumour region of head-and-neck patient # 13: (a) SUV distribution 2 h pi of one PET slice, (b) parametric plot: S_∞ for each voxel.

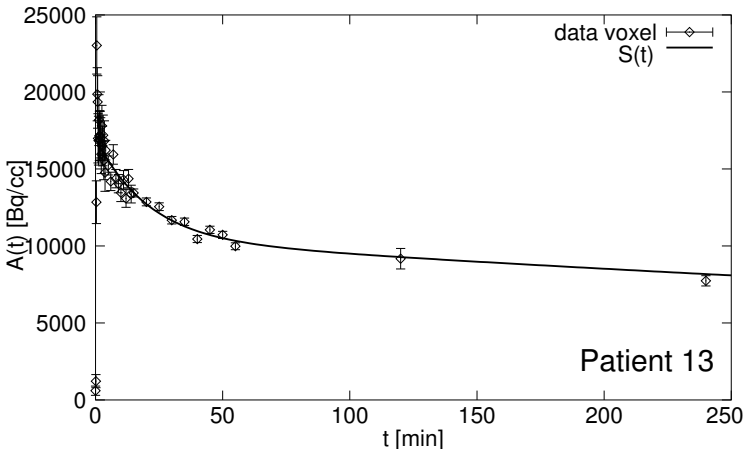

Figure 5.7: Typical TAC of the tracer accumulating region in figure 5.6.

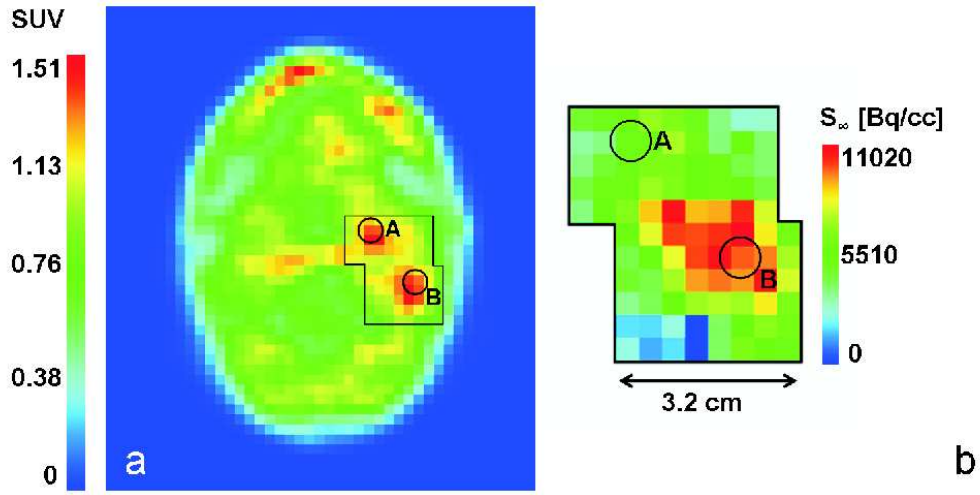

Figure 5.8: (a) SUV distribution 2 h pi, (b) parametric plot for the marked tumour region of patient # 6: S_∞ for each voxel.

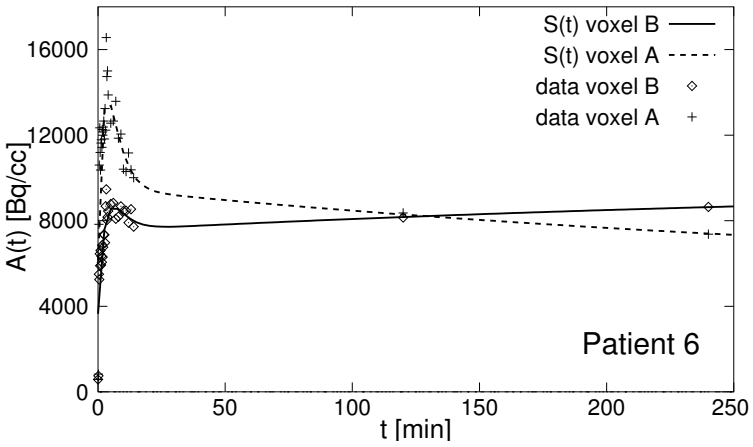

Figure 5.9: Comparison of the overall curve shapes of voxels A and B, figure 5.8.

image acquisition. Therefore, it does not seem reliable to identify hypoxia only on the basis of a static image 2 h pi which obviously bears a high risk of incorrect interpretation.

5.5 Discussion

The presented investigation showed that the overall shapes of the TACs contain essential information about hypoxic tumour areas. Particularly the behaviour of the curves at long time scales is important. Hence, a criterion based on a single time point threshold is not sufficient to perform a reliable hypoxia analysis. SUV thresholds were used by other investigators [33, 57] in order to calculate the hypoxic sub-volume of a tumour.

Curve features such as the position of the minimum in the TACs between 20 and 60 min hint at the characteristics of the underlying processes which occur on corresponding time scales. This property is understandable by the immunohistochemical investigations with pimonidazole [30, 31, 41] that found that long diffusion distances had to be travelled by the tracer before reaching hypoxic cells. The signature of the characteristic diffusion times in the tumour tissue is the position of the minimum in the curves.

The presented model involves slow diffusion rates of the tracer in the interstitium, caused by long diffusion distances in the tumour tissue. It also respects the inherent heterogeneity of tumour tissues, where well perfused and hypoxic sub-volumes may coexist in the same PET voxel. These facts were not considered by previous models [12], which explicitely treated homogeneous tumour tissues and were more appropriate to normal tissues made hypoxic under experimental conditions.

The heterogeneity of the tumour structure requires that all compartment weights remain floating in the fits to accommodate partial volume effects by virtue of the linearity of the differential equation and that the input function becomes spatially variable. The derivation of this specific compartment model from the 'classical' kinetic modelling is well justified by the difference of the tissue architectures. Due to the particular choice of the input function and the assumption of physical transport into the diffusive compartment which ensures $k_{1,in} = k_{1,out}$, the total number of fit parameters is five. This reduces the variability and co-variance of the fits. The experimentally established need for a spatially variable input function poses an obstacle to the use of graphical TAC analysis such as the Logan plot [42, 43].

A kinetic model was developed, which allows the analysis of dynamic FMISO TACs. This compartmental analysis enables to derive a set of five different parameters from the shape of the TACs. The values of these param-

eters contain information about the structural configuration of the tumour. In the following chapter, a statistical analysis is carried out in order to identify single parameters which are related to the radiation sensitivity of the tissue.

Chapter 6

Step II: Correlation to Therapy Outcome

Tumor hypoxia has been known to be associated with poor radiation response for several decades. Recent publications suggested that hypoxia in tumours had a direct influence on treatment success [15, 20] by a variety of mechanisms [70, 71]. A prognostic impact of tumour hypoxia for therapy outcome in head and neck cancer (HNC) has been shown by different investigators [9,48,49]. Hypoxia has also been related to lower survival probability and higher risk of recurrence in patients with cervix cancer [20, 25]. In these studies, hypoxia was assessed invasively by polarographic Eppendorf electrodes.

In the following chapter, the derived quantities of the kinetic analysis are linked to RT outcome. The patient specific values for perfusion, kinetic constants and the concentration of tracer retaining cells are shown to correlate well with treatment outcome for this group of 15 HNC patients.

6.1 Scatter Plots

Hypoxia is a consequence of an irregular vasculature as it occurs only in a certain distance from the blood vessels. The quality of the vascular irregularity gives rise to different measures of hypoxia. Hypoxia exists only in the 'gaps' between the blood vessels. Hence, to measure the 'mesh size', the characteristic distance between blood vessels may reveal information about the configuration of the vessel system. In addition, vascular efficiency and hypoxia carry independent information. If the pouches between the vessels become too large, necrotic areas will develop, which do not accumulate the FMISO tracer. The kinetic model presented in chapter 5 allow us to distin-

guish by separating the amount of unbound tracer from the signal emerging from tracer retaining cells. By virtue of the kinetic model analysis of the time-activity curves of tracer uptake, it is possible to eliminate the non-specific background activity in the signal. A *scatter plot* is generated by plotting the value of w_0, the *perfusion efficiency* (P) on the ordinate against $\tilde{w}_A\tilde{k}_3$, describing the *tracer retention potential* (R), i.e. the concentration of hypoxic cells weighted with the mean degree of hypoxia for each voxel on the abscissa. Characteristic patterns in the scatter plots will allow to distinguish between tumour areas according to vascular density and concentration of hypoxia.

6.2 Data analysis and statistics

Tumor control was defined on the basis of computed tomography (CT) scans as complete and persistent regression of the primary tumour and failure was defined as local recurrence of the tumour in the irradiated volumes. Follow up time was determined from the end of RT treatment until the day of the last CT.

Loco-regional tumour control probability was estimated using the Kaplan-Meier method [73]. Differences between curves were analyzed with the log-rank-test [74].

Different variables that might influence treatment outcome were compared using the Wilcoxon-Mann-Whitney (Wilcoxon signed rank) U-test [3,5] between patient groups showing no local relapse and failure. In all cases, a two-sided significance level of 0.05 was used. Correlation of different variables with treatment success was assessed using a Pearson correlation coefficient [3].

The impact on treatment outcome was checked for different classes of variables: tumour volume and patient age, SUV related factors and variables derived from the kinetic analysis. The SUV related factors were the maximum standardized uptake value (SUV_{max}) and the fractional hypoxic volume (FHV) 4 h after FMISO injection. FHV is defined as the fraction of tumour volume presenting a tumour-to-blood ratio larger than 1.4. Both variables SUV_{max} and FHV have been correlated with tumour hypoxia in earlier studies [18, 57]. Finally, a number of parameters derived from the compartmental analysis were checked for a statistically significant influence on therapy outcome. These parameters were the mean value of R, the mean value of perfusion, and two metrics involving both tracer retention R and perfusion P parameter values. A first metric was defined intuitively as the volume integral of the retention-to-perfusion ratio (RPR). A second metric,

which was derived from a model of tumour dose-response and reoxygenation, is the *Malignancy* value M. The malignancy M is a phenomenologically defined metric which allows to mathematically describe the hypoxia – perfusion scatter pattern of a patient according to the following formula:

$$M = \sum_{i=1}^{N} M_i = \sum_{i=1}^{N} e^{\frac{bR_i}{P_i + P_0}} \quad . \tag{6.1}$$

Here, N is the number of voxels of the tumour, R_i and P_i are tracer retention and perfusion values of voxel i. The value of M_i will be the larger, the lower P is and the higher R is. M_i is the malignancy value of a single tumour voxel. A motivation for the specific choice of this metric and a description of its intrinsic properties will be presented in detail in chapter 7. The parameter values of b and P_0 are $b = 208.0$ and $P_0 = 0.704$. They are derived from a fit to a TCP-model, introduced also in chapter 7.

6.3 Patterns of Hypoxia and Perfusion

The kinetic model (see chapter 5 is able to discriminate the variety of observed types of FMISO TACs. These curve shapes can be associated with three main types of tumour tissues: (1) tissue areas with a high vessel density, (2) well perfused but also hypoxic, and (3) severely hypoxic and badly perfused tumour areas. Figure 6.1 shows that characteristic TACs are associated to distinct areas in the scatter plot. The patterns for the whole group of patients are displayed in scatter plots in figure 6.2. It becomes apparent, that the ultimate purpose of the kinetic model is to subtract the background of unbound tracer from the signal intensity.

Statistics

Image analysis of the FMISO PET scans taken 4 h pi revealed maximum SUVs in the tumour volume between 1.36 and 4.02. The median SUV_{max} was 2.25. The FHV ranged from 0 to 72.5% with a mean of 19.7%. Due to the chosen tumour volume definition strategy, which adds a margin, the determined FHV can never reach 100%.

Examination of the scatter plots showed very different patterns of hypoxia and perfusion. All possible combinations of hypoxia and perfusion parameters were observed: well perfused tumours which were not at all hypoxic, tumours showing at the same time a quite high vascular density and hypoxic subareas, and finally also tumours that were badly perfused and severely

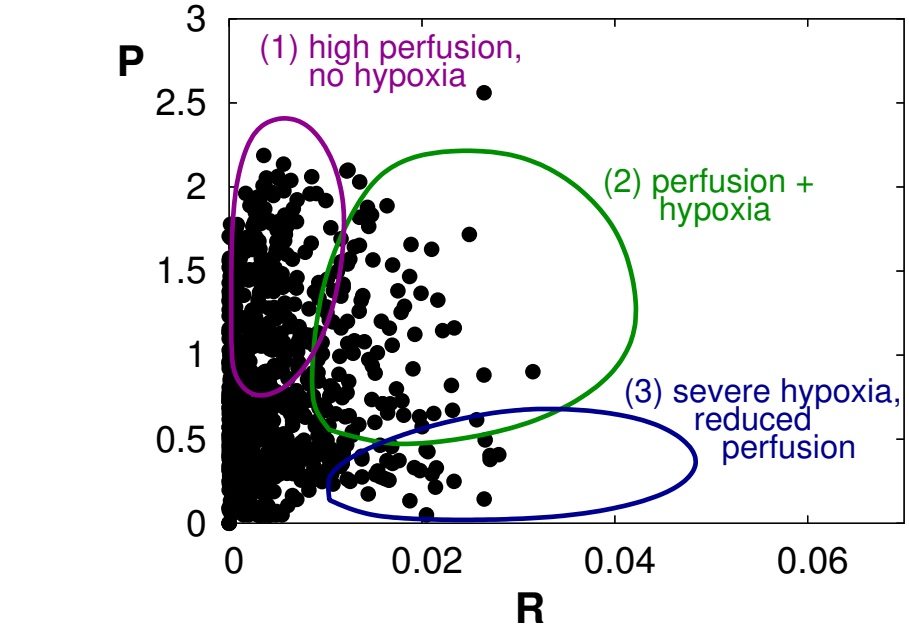

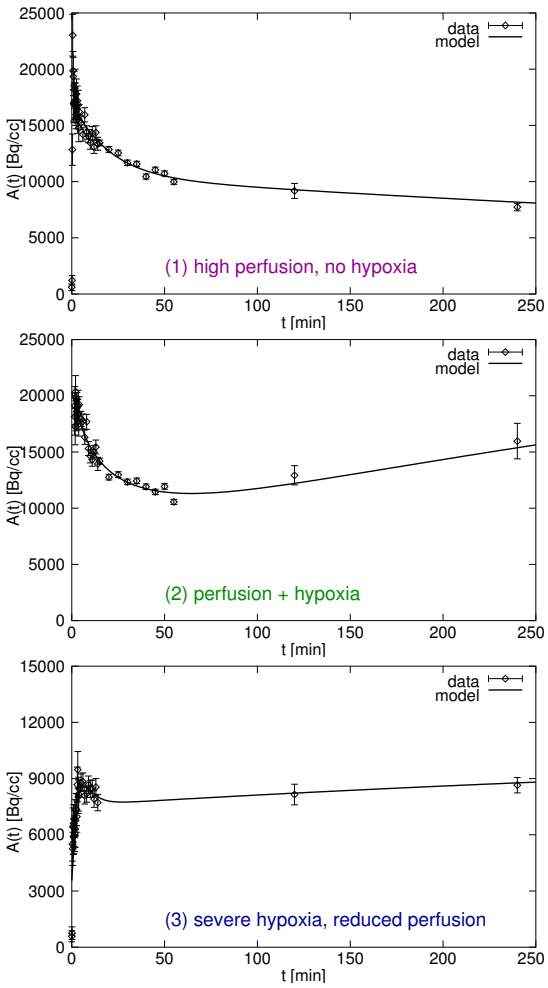

Figure 6.1: *Above:* Scatter plot for one patient based on tracer retention (R) and perfusion (P) parameters resulting from a kinetic FMISO analysis. Schematically shown are typical regions for characteristic perfusion-hypoxia patterns: (1) High perfusion without hypoxia, (2) well perfused and simultaneously hypoxic, and (3) severe hypoxia, low vessel density. *Left:* Corresponding types of characteristic FMISO Time-Activity Curves.

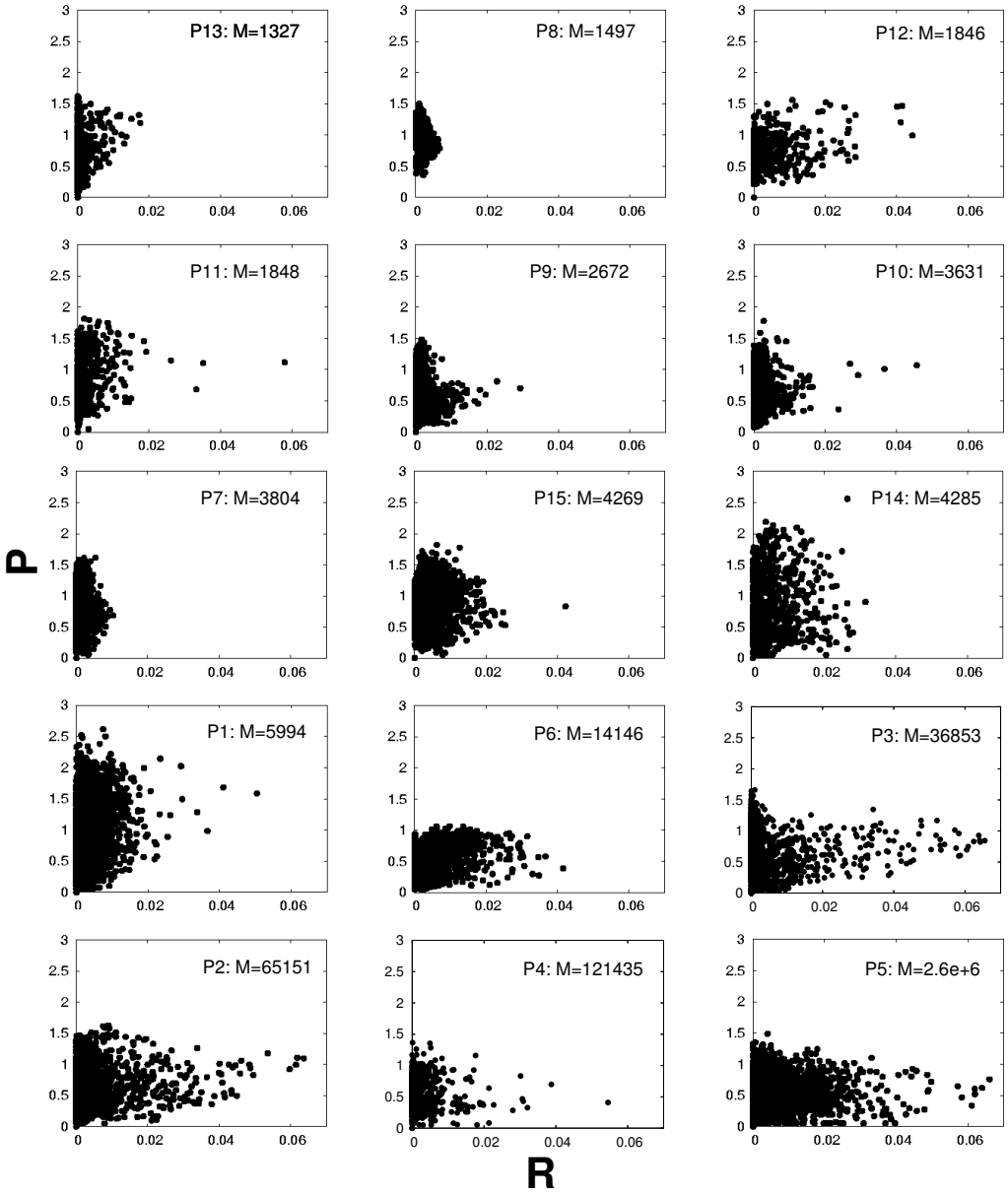

Figure 6.2: Scatter plots of all 15 patients with increasing M-value.

hypoxic. These two variables represent physiological tumour characteristics that are not correlated ($r = -0.096$). As a first result, it has to be stated that hypoxia occurs independently from the degree of perfusion in tumour tissues.

The Wilcoxon-Mann-Whitney U-test with respect to the age of the patients showed no difference ($p = 0.3$) between the subgroups with and without relapse. In contrast, there was a significant difference in tumour volume between the two subgroups ($p = 0.014$). This corroborates the findings of earlier studies that correlated tumour size with treatment outcome [52]. Also, SUV_{max}, determined 4 h after injection separated patients according to failure and progression free survival (PFS). The significance for SUV_{max} was only weak $p = 0.041$, whereas the U-test for the FHV showed no significance at all ($p = 0.13$).

Regarding the variables derived from the kinetic analysis, mean tumour perfusion and RPR discriminated between the group without recurrence and the failure group ($p = 0.05$ and 0.008, respectively). The mean tracer retention value showed no significance ($p = 0.18$). Finally, the malignancy value M was highly significant, with $p = 0.0013$ (table 6.1). The prognostic value of this model based metric M is higher than the value of tumour size or SUV_{max} after 4 h.

Figures 6.3 and 6.4 show the Kaplan-Meier plots according to the variables tumour volume and Malignancy, respectively. Malignancy also grows linearly with tumour volume. The progression free survival curves for the two subgroups separated by tumour volume were not significant ($p = 0.08$), whereas the Malignancy metric is a variable which has a high potential to

Univariate statistical analysis		
Variables	p-value U-test	p-value log-rank test
age [years]	NS* (0.30)	NS* (0.91)
tumour volume V [cm^3]	0.014	NS* (0.08)
$\mathrm{SUV}^{\dagger}_{max}$	0.041	NS* (0.10)
FHV‡ [%]	NS* (0.13)	NS* (0.53)
mean retention*	NS* (0.18)	NS* (0.24)
mean perfusion§	0.05	NS* (0.11)
RPR§	0.008	NS* (0.09)
malignancy value $M^{\S}$	0.001	0.01

Table 6.1: Results of univariate analysis of prognostic factors. *NS: not significant ($p > 0.05$); $^{\dagger}\mathrm{SUV}_{max}$: maximum SUV; ‡FHV: fractional hypoxic volume. § derived from kinetic model

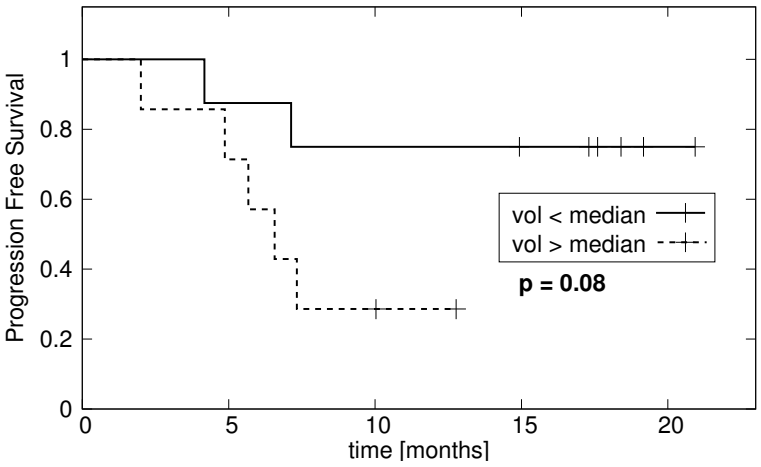

Figure 6.3: Kaplan-Meier Plot for patient subgroups separated according to tumour volume. Crosses represent censored data points. p-value is calculated according to the log-rank test.

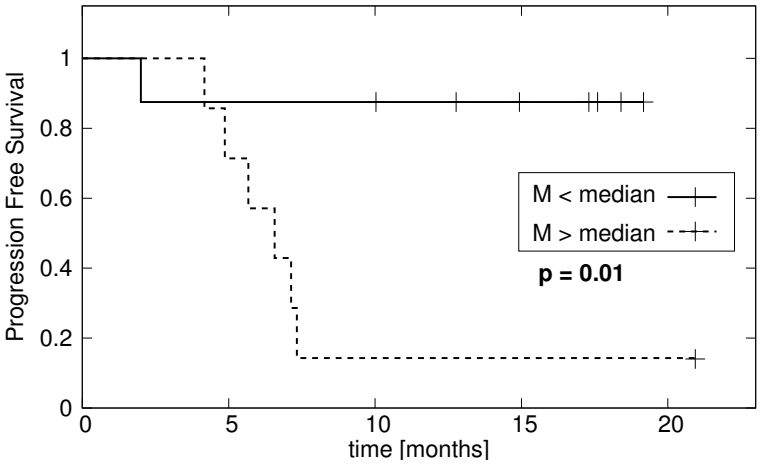

Figure 6.4: Kaplan-Meier Plot where the two groups are separated according to the Malignancy metric. Crosses represent censored data points. p-value is calculated according to the log-rank test.

stratify patients according to treatment outcome (see also table 6.1). In this case, the log-rank p-values turned out to be $p = 0.01$. Hence, the malignancy metric is a prognostic factor with respect to progression free survival.

6.4 Discussion

The results of this study showed, that SUV_{max} alone even at late time points has limited predictive value. These findings are in line with results of other investigators [6] who found that SUV 2h pi and Eppendorf pO_2 did not correlate well.

A limiting factor for the retention of FMISO in the tumour is that binding of the tracer can only take place in *viable* hypoxic cells which may be few if the tumour is largely necrotic. In other words, a low level of the FMISO TAC several hours after tracer injection is not necessarily due to non-hypoxic tissue. This might also be caused by largely necrotic tumour areas which contain only a very low number of strongly hypoxic cells. In this case, the low intensity of the PET signal would lead to an underestimation of the extent of hypoxia by the SUV-method. A kinetic analysis subtracts the non-specific background signal and hence enables to determine the local tracer retention potential of the tumour. Still, the classical hypoxic tumour core may only give a weak signal due to the low density of tracer retaining cells. Hence, a second parameter is needed to give a more complete picture of the abnormalities of the vascular architecture.

FMISO uptake kinetics are quite slow due to long diffusion distances and for lack of active transport mechanisms. PET scans several hours after injection of the radiotracer are therefore essential. Nevertheless, dynamic scans at short times pi cannot be abandoned, as they are needed to determine the degree of perfusion of the tumour.

There is no possibility in FMISO PET to distinguish between acute and chronic hypoxia [17]. On one hand, this is due to a quite large size of the image voxels ($\approx (4\text{ mm})^3$). On the other hand, the slow kinetics of tracer retention do not allow a distinction of fast re-perfusion. Since both effects are a consequence of the deficient vasculature, they may co-exist anyway.

The analysis of the parameters derived from the kinetic model demonstrated, that tracer retention and perfusion values alone do not predict treatment outcome. Additionally, hypoxia occurred independent of degree of perfusion, since no correlation was found between the two variables. Furthermore, it turned out that either one variable did not suffice to describe the vascular architecture fully. The two parameters perfusion efficiency and tracer retention are linked to the total capacity of blood vessels (P) and to

the spatial resolution of the vascularization (R). Hypoxia is a symptom of a deficient vasculature and can be a result of both, a low capacity and/or a poor distribution of vessels. Hence, the combination of two kinetic parameters carries more meaning than just one. Taking both parameters together proved to be reliable predictors for treatment outcome. The malignancy metric M, which involves these two physiological characteristics of the tissue, was found to be the strongest prognostic factor.

The results of this study demonstrate that dynamic FMISO PET has prognostic value for therapy outcome, but only when perfusion and retention are both taken into consideration. Hence, dynamic FMISO PET might in the future be used to select patients for an adapted radiotherapy treatment as e.g. dose painting [2,13,37]. Furthermore, variables derived from a kinetic analysis [64] may serve to determine individual dose escalation factors in order to overcome hypoxia related treatment resistance.

Most essential for the design of new adaptive treatment strategies is the time until reoxygenation takes place after the beginning of RT. The malignancy metric M involves an estimate of this characteristic time. The worst physiological setting in a tumour seems to be the combination of low perfusion and severe hypoxia, as reoxygenation then appears to be very slow. In contrast, a high degree of perfusion co-existing with hypoxic areas may favour fast reoxygenation. Hence, this setting might be associated with an intermediate level of risk. This interpretation can be supported by follow-up scans during RT, which will be reported on in chapter 7.

Chapter 7

Step III: A Hypoxia TCP Model

In the present chapter, a model for the influence of hypoxia on tumour control probability (TCP) is developed. The configuration of the vascularization is essential for possible reoxygenation processes and therefore also for the response to treatment. The TCP model estimates the time to reoxygenation from measurements of perfusion efficiency and hypoxia with the PET tracer [^{18}F]-FMISO. Its design is guided by a series of repeated FMISO PET scans. These follow-up data for the patient group give some insight into the changes of both perfusion efficiency and hypoxia. All dynamic PET scans were evaluated with the kinetic compartment model introduced in chapter 5.

7.1 Development of a Tumour Control Model

Assuming that a hypoxic cell population shows a decrease in radiosensitivity, this population cannot be controlled by doses applied via conventional radiotherapy [21]. The population of hypoxic cells determined the treatment outcome unless it is reduced by reoxygenation. Thus, the most relevant quantity for hypoxia TCP is the time from the onset of radiotherapy to reoxygenation, which is equivalent to the number of treatment fractions lost on the radioresistant cells. At first sight, this suggests that a single pre-treatment hypoxia image cannot be sufficient to determine the required extent of dose escalation.

The presence of regions in a tumour where cells can suffer from a lack of oxygen supply is a result of an insufficient or deficient vasculature. Hence, despite the complicated processes that occur during normal growth or under therapy, like repopulation, redistribution between cell compartments, and

loss of cells either by starvation or as a consequence of therapy, the central question for HIDE is: When does the vasculature become sufficient again, either by neovascularization or reduced consumption, or both? Animal experiments show that the phenomenon of hypoxia is an inherent property of cell lines [41] and can outlast the lifespan of hypoxic cells by far [39]. The emergence of hypoxia seems to be engrained in the growth characteristics of a clonogen population.

If functional imaging reveals the irregularity and coarseness of the tumour vasculature, it may be possible to estimate the time to reoxygenation. In dynamic studies of PET tracer or MR/CT contrast agent uptake, it is possible to obtain a measure of the efficiency of perfusion (determined by the number, calibre and distribution of blood vessels and the magnitude of blood flow within them) during the influx phase shortly after injection. The degree of hypoxia as given by the uptake of PET tracer is in itself an indicator of the coarseness of the vasculature, as hypoxia can only persist in wide gaps between perfused blood vessels. The combination of both, perfusion efficiency and hypoxia labeling, has been shown to carry significant information about the success of chemo-radiotherapy [65].

7.1.1 Observations

The distributions of tracer retention – perfusion efficiency for each patient can be classified as one of three typical scatter patterns. The classical hypoxic tumour shows high tracer retention and lower than average perfusion efficiency values, see figure 7.1(a). Here, a deficient vasculature creates pockets of severe hypoxia, which may even contain necrotic cells which are not visible on FMISO images. A second class of tumours shows significant tracer retention and more than average perfusion efficiency values, see figure 7.1(b). These tumours do have a viable vasculature, but oxygen consumption is so high that the supply is not sufficient. These tumours may be more amenable to hypoxia-modifying treatments and may show faster reoxygenation than the first type. Finally, tumours of the third class show no tracer retention, while their perfusion efficiency values are normal to greater than average, see figure 7.1(c). In chapter 6 it was shown that the prognosis for type 1 is very poor, for type 2 intermediate, but very good for type 3.

The fast response of a tumour to radiotherapy could be dominated by two effects. Firstly, due to a deceleration of proliferation, the oxygen consumption drops and as a consequence, perfusion limited hypoxia vanishes. Secondly, due to an acute inflammatory reaction, the blood flow increases which increases oxygen supply with the same result as above. This turns out to be the reoxygenation pattern of type 2 tumours. Of the 6 patients

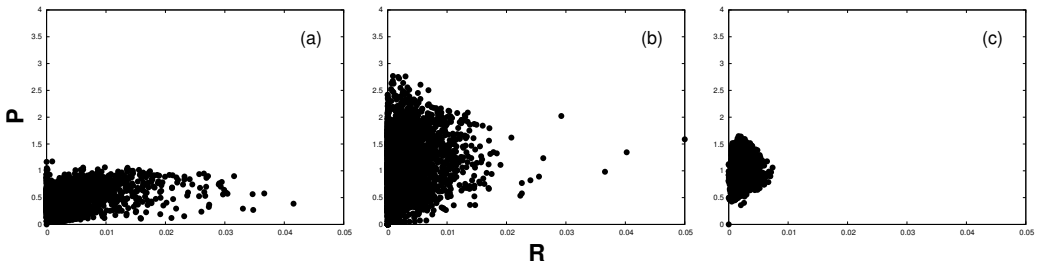

Figure 7.1: Scattergrams of tracer retention R versus perfusion efficiency P for patients # 6 (a), # 1 (b) and # 8 before the start of RT.

classified as type 2, only 3 had noticeable traces of hypoxia left at 20 Gy, while the perfusion was generally enhanced.

At later times during treatment, the reoxygenation response could be shaped by an overall shrinkage of tumour mass and neovascularization, two effects that can enhance the quality of the vasculature, while it is certainly also damaged by radiation. The net effect is somewhat elusive on the basis of current knowledge. For this reason, type 1 tumours are more interesting study objects. Figure 7.2 shows the scatter patterns of patient 6 before treatment (a), at 20 Gy (b) and at 50 Gy (c). The early response leads to increased perfusion efficiency, but the overall reduction of tracer retention is rather small. The 20 Gy scatter pattern resembles a type 2 tumour. At 50 Gy, hypoxia has almost vanished, resulting in a type 2-3 scatter pattern.

The example of this patient suggests the hypothesis that the footprint of reoxygenation in the scatter patterns is a *progression to less malignant types*. The aforementioned and additional unknown mechanisms of reoxygenation and redistribution may in effect increase perfusion efficiency and reduce tracer

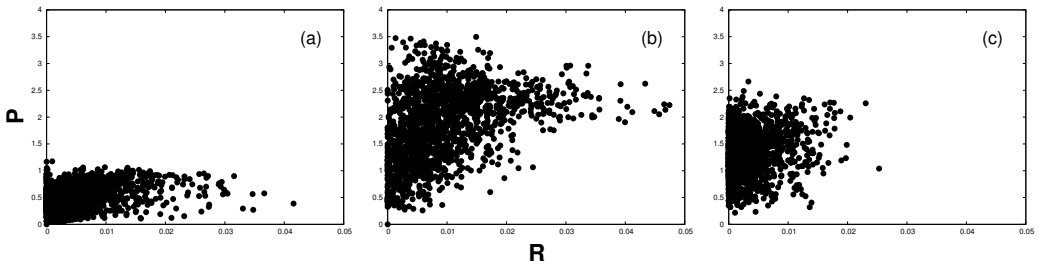

Figure 7.2: Scatter pattern of patient # 6 (a) before treatment, (b) at 20 Gy and (c) at 50 Gy.

retention and thus propagate a volume element in the scatter plot from the lower right to the upper left. This propagation would move a volume element from a region of high malignancy to lesser malignancy. Hence, the lines of equal malignancy would run orthogonal to the direction of propagation, i.e. from the lower left to the upper right. This is in fact what a TCP model needs to capture.

7.1.2 Model Design

Naturally, given the population-averaged experimental data, the best a tumour control model including reoxygenation can do is to describe the observations. No attempt at a mechanistic model is made, and all parameters are understood as averages over the patient population.

We start with the common Poisson approximation of TCP

$$-\ln \mathrm{TCP} = \rho \sum_{i=1}^{n} \exp(-\alpha_0 D_i) \quad , \tag{7.1}$$

where ρ is the mean cell density per volume element, α_0 is the mean cell sensitivity, D_i is the dose in volume element i and the sum runs over all volume elements $i = 1, ..., n$. The rhs is equal to the expected value of surviving cells in the total tumour volume, henceforth denoted with μ_0. If $\mu_i = \rho \exp(-\alpha_0 D_i)$ is the expected value of surviving cells per volume element, we obtain

$$\mu_0 = \sum_{i=1}^{n} \mu_i \quad . \tag{7.2}$$

Assume now that the cells of a given tumour volume element are labelled according to their distance to the next perfused blood vessel. Next, the cells are sorted according to their distance label and collected into bins such that each bin contains the same number of cells. Hence, the bin $[0, \Delta s]$ contains the fraction Δs of all cells being closest to the next blood vessel, likewise, the interval $[1 - \Delta s, 1]$ contains the fraction Δs of all cells with the largest distance to the next perfused blood vessel.

In order to take into account hypoxia induced radio-resistance, we assume that each bin has a specific mean cell sensitivity $\alpha(s)$ and reoxygenates after a fraction $t_R(s)$ of the total number of treatment fractions. Therefore

$$\mu_i = \rho \int_0^1 ds \exp\left(-\alpha(s) t_R(s) D_i - \alpha_0 (1 - t_R(s)) D_i\right) \tag{7.3}$$

$$= \rho \exp(-\alpha_0 D_i) \int_0^1 ds \exp\left(-(\alpha(s) - \alpha_0) t_R(s) D_i\right) \quad . \tag{7.4}$$

The integral is the excess of cells surviving the treatment because of reduced cell sensitivity. In case no hypoxia is present, the integral is 1. If there is some hypoxia present, the integral becomes rapidly dominated by the most distant cells ($s \approx 1$) where $\alpha(s)$ is smallest and $t_R(s)$ largest. In keeping with the well established saddle-point approximation (i.e. $\alpha_0 D_i >> 1$), we write

$$\int_0^1 ds \exp\left(-(\alpha(s) - \alpha_0) t_R(s) D_i\right) = \exp(-(\alpha_h - \alpha_0) t_R D_i) \quad , \tag{7.5}$$

where α_h and t_R are the macroscopically observable quantities of cell sensitivity and reoxygenation time for this volume element. The rhs is termed the *Malignancy value* M_i of this volume element.

The kinetic analysis of FMISO uptake delivers for each volume element a measure of perfusion efficiency P and of tracer retention R. In chapter 6 it was shown, that the distributions of (R, P) are quite characteristic for each tumour, with an indication that the presence of high-R/low-P volume elements is an unfavourable indicator for treatment response. Here, we assume

1. the macroscopic cell sensitivity α_h is proportional to the tracer retention R and

2. the macroscopic time to reoxygenation t_R is proportional to $1/(P+P_0)$, suggesting that there exists a maximum time $1/P_0$ after which any volume element will have reoxygenated.

In the results section below, we elaborate on this choice.

Finally, we obtain

$$M_i = \exp(bR_i/(P_i + P_0)) \tag{7.6}$$

and, assuming that $D_i = D$ everywhere

$$\mu_0 = \rho \exp(-\alpha_0 D) \sum_{i=1}^{n} M_i \quad . \tag{7.7}$$

The parameters $A = \rho \exp(-\alpha_0 D)$, b and P_0 were determined by a maximum log-likelihood fit [16] of $\exp(-\mu_0)$ to the group of 15 patients.

7.2 Results

The TCP model predicts a progression of the scatter plot during RT to less malignant phenotypes, i.e. to higher perfusion efficiencies and lower levels of

tracer retention. From eq. (7.6), the lines of constant malignancy have the form

$$P = \frac{bR}{\ln M} - P_0 \quad . \tag{7.8}$$

The model was chosen such that it produces the simplest possible form of iso-malignancy lines that still describes the observations. The directions of progression to lower malignancy obtain as

$$\nabla M = \frac{bM}{P + P_0} \begin{pmatrix} -1 \\ \frac{R}{P+P_0} \end{pmatrix} \quad . \tag{7.9}$$

Figure 7.3 shows the iso-malignancy lines and the directions of progression for the example patient of figure 7.2.

By virtue of its definition, a certain malignancy value M is equivalent to an M-fold increase of the expected number of surviving cells per unit volume.

The parameters of the model were obtained from a maximum likelihood fit to the initial set of 15 patients. The following parameter values were determined from the fit: $A = 9.92 \cdot 10^{-5}, b = 208.0$ and $P_0 = 0.704$. The goodness of fit was estimated by evaluation of the deviance Δ. The deviance is defined as twice the difference between the current and the full log-likelihood $\Delta = -2(L_c - L_f)$, which is supposed to follow a χ^2 distribution. In our

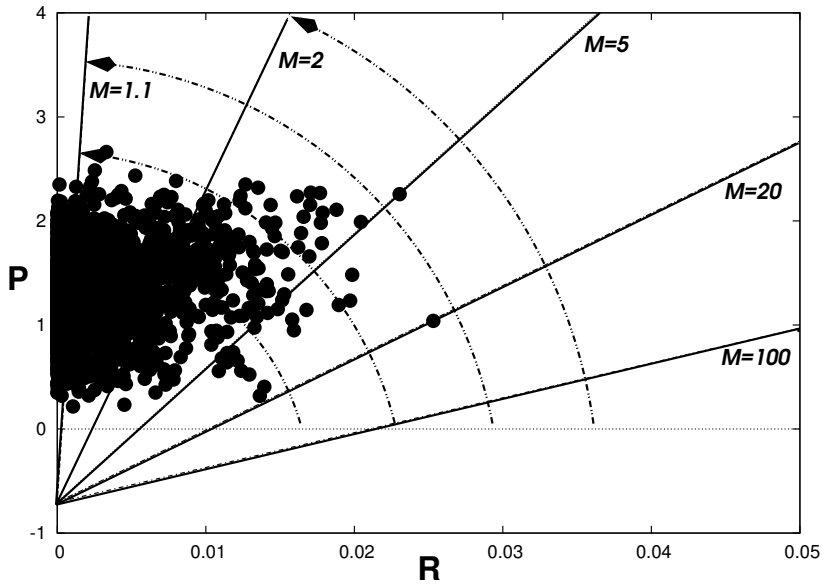

Figure 7.3: Isolines for different malignancy values M and directions of progression to lower Malignancy for patient #6.

case, the deviance confirmed an acceptable fit ($\Delta = 2.75, p > 0.05$). For each patient, a TCP value was computed. The patients were grouped according to the expected number of surviving cells μ_0 into four groups. The observed rate of local control is compared with the predicted TCP value of the model in figure 7.4.

The ratio of $\bar{M}$ before the start of treatment ($\bar{M}_0$) and after 10 fractions ($\bar{M}_{10}$) represents the factor by which the expected value of surviving cells is increased due to hypoxia. For the analysis of the mean malignancy $\bar{M}$, only patients were taken into account that presented $\bar{M}_0 \geq 1.69$. This cutoff value was chosen to be equal to a reoxygenation time of two days. Four of the ten patients presented $\bar{M}_0$-values below this cutoff (# 1, 7, 10 and 13), whereas the mean malignancy values for the remaining six patients are shown in table 7.1. These results support in four cases (# 3, 4, 6 and 14) the hypothesis of a progression to less malignant tumours during irradiation. The high M-value in the follow-up scan of patient 2 is possibly caused by too sparse dynamic data acquisition points (dynamic acquisition for only 10 min), which resulted in high errors for the kinetic analysis. In contrast, the small malignancy increase seen for patient 9 might be due to eventual errors during data analysis.

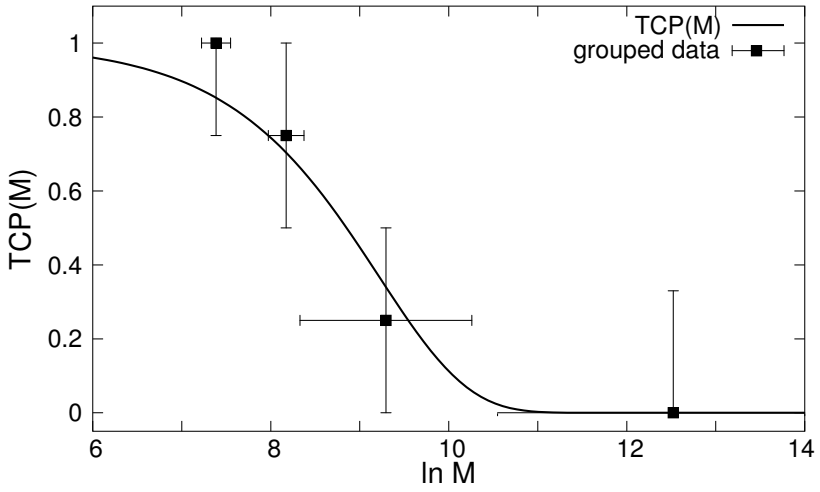

Figure 7.4: TCP model fitted to the patient outcome data.

Pat #	$\bar{M}_0$	$\bar{M}_{10}$
2	35.3	15810
3	17.1	1.16
4	143.1	71.0
6	8.39	2.56
9	1.80	4.56
14	6.02	1.61

Table 7.1: Mean malignancy values $\bar{M}$ before the start of treatment and after 10 fractions for all patients with $\bar{M}_0 \geq 1.69$.

7.3 Consequences for Hypoxia Image Guided Dose Escalation (HIDE)

The present development sees hypoxia and reoxygenation essentially as a consequence of a deficient vasculature and its response to radiation. While hypoxia constitutes a severe problem in radiotherapy for a variety of reasons [15], it stems from a deeper cause. The model tries to capture the observable patterns of hypoxia and reoxygenation, both of which are linked to the irregularity of vascularization.

The processes occurring as response to therapy in an individual tumour are many and varied. Histological studies suggest, that any imaginable effect can indeed be found in some specimen [39–41]. Naturally, a population based TCP model can only describe the net effect of all possible scenarios of hypoxia/reoxygenation on local control. Within the limitations of the study size, this seems to be possible with a single pre-treatment hypoxia image.

The reason for this may be that on average, both the initial degree of hypoxia and the speed of reoxygenation are linked to the irregularity of the vasculature. The patchiness of the intervascular spaces defines the regions where hypoxia can occur. Redistribution of cells between compartments or even a constant loss of the most hypoxic cells do not change anything about the number of cells that are located in a hypoxia-prone region at any given time. Only slower processes like neovascularization or shrinkage of the tumour can change the overall constitution of the vasculature.

In this image, the concepts of acute and chronic hypoxia seem to lose meaning in the context of clinical treatments. Clearly, both are signs of a less than sufficient vasculature, so the likelihood of coincidence is high, especially given the rather large dimensions of PET image voxels. For a model that averages over the total treatment time and a population of patients, all

that matters is the mean size of the hypoxic pouches created by the patchy vascularization. The more relevant distinction here is whether this quantity diminishes quickly due to fast reoxygenation, driven by increased supply and reduced consumption of oxygen, or whether reoxygenation occurs by slow processes.

The speed of reoxygenation also impacts the strategy of dose escalation that could be adopted to overcome hypoxia induced radioresistance, and the consequential reduction of cell kill. If dose escalation was applied from the beginning of treatment, a lot of the additional dose administered to the hypoxic region could be wasted on resistant cells if reoxygenation was slow. It could be better to wait with escalation until reoxygenation has occurred and make up for the loss of cell kill towards the end of the treatment, when the dose is more efficient. This strategy runs the risk that reoxygenation may come too late and the dose per fraction becomes too high.

The model affords predictions about the required dose escalation per volume element. If the strategy of a late boost after reoxygenation is to be adopted, we require for the additional dose ΔD

$$M_i \exp(-\alpha_0 \Delta D) = 1 \tag{7.10}$$

which leads to

$$\frac{\Delta D + D_0}{D_0} = \frac{\ln M_i}{\alpha_0 D_0} + 1 \tag{7.11}$$

where D_0 is the base treatment dose, in our case 70 Gy, and the cell sensitivity of non-hypoxic tumours α_0 equals, say, 0.4. This strategy assumes that the image of initial hypoxia is frozen in the distribution of remaining cells half way into the treatment.

In contrast, a homogeneous boost has to overcome the mean cell sensitivity $\bar{\alpha}$

$$M_i \exp(-\alpha_0 D_0) = \exp(-\bar{\alpha} D_0) \tag{7.12}$$

so that if we require that

$$\bar{\alpha}(\Delta D + D_0) = \alpha_0 D_0 \tag{7.13}$$

it obtains

$$\frac{\Delta D + D_0}{D_0} = \frac{\alpha_0 D_0}{\alpha_0 D_0 - \ln M_i} \quad . \tag{7.14}$$

This strategy assumes that the reoxygenation is not accelerated by the hypofractionation. Both strategies do not take into account the additional effect of greater fraction sizes as it is felt that this is of secondary importance given the individual uncertainties of hypoxia images and their interpretation.

It can be seen easily by Taylor expansion of eq. (7.14) for $\ln M_i \geq 0$ small, that both factors agree for small dose escalations. For large dose escalations, the first factor becomes noticeably smaller than the second. The observed range of required dose escalation factors in the present population according to eq. (7.14) was between 1 and 1.66 (see chapter 8).

The presented TCP model can be used as a key in order to perform individual, spatially varying dose prescriptions according to the regional TCP. In chapter 8, a planning study is carried out with the goal to investigate the technical feasibility of applying Hypoxia Image Guided Dose Escalation (HIDE).

Chapter 8

Step IV: Dose Painting Planning Study

In this chapter, the results obtained so far from the kinetic analysis of dynamic FMISO data and from the corresponding TCP model will be applied for dose painting (DP) treatment planning. A dose escalation (DE) is prescribed in addition to the conventional radiotherapy (RT) treatment in order to overcome hypoxia-induced radiation resistance. DE to a tumour that was identified as hypoxic can be beneficial because of different aspects, concerning malignancy and radiosensitivity of the tissue. Hence, a DP concept can be based on different hypothesis.

The presence of hypoxia indicates a more malignant phenotype of tumour which may coincide with a number of unfavourable traits, e.g. enhanced proliferation. To counteract these mechanisms preemptively, a uniform dose escalation (uniDE) to the entire macroscopic tumour volume is proposed. In order to identify this volume, FDG PET can be used. However, a major limitation of this approach might be the high dose levels applied uniformly to large volumes. In addition, there might be a risk of an unacceptably high probability of serious acute reactions and higher normal tissue doses.

For these reasons, the idea of hypoxia DPBN [2, 7, 37, 62, 66] that applies higher doses only where needed seems to be very promising from a clinical point of view. Applying spatially variant doses - according to the degree of hypoxia, might allow a significant reduction of the normal tissue burden and additionally reduce the overall treatment dose. A measurable amount of hypoxia is known to cause therapy resistance [9, 20, 48, 49]. However, in order to assign accurate dose prescriptions for DPBN on the basis of hypoxia PET, a clear relation between treatment outcome and the considered hypoxia imaging method is required. In chapter 6, the correlation between dynamic FMISO PET and RT outcome was demonstrated. For this purpose, the

FMISO data was analyzed using the kinetic model introduced in chapter 5, which allowed for the determination of characteristic parameters related to the degree of hypoxia and blood vessel density. The key requirement for the translation of functional imaging data into clinically promising dose prescriptions is given by the TCP model based on these parameters and their relation to tumour reoxygenation, as shown in the previous chapter.

The present chapter investigates the feasibility of hypoxia DP in a patient population. A planning study with 13 HNC patients was performed, where for each patient three IMRT plans were created: a hypoxia DPBN plan according to a DE map determined from the dynamic FMISO PET data, a uniDE to an FDG-based BTV, and a conventional IMRT plan. All of these plans were restricted to the same dose in the organs at risk (OARs) spinal cord, brain stem and parotid glands. The aim of of this study was to evaluate DE strategies with respect to target coverage at constant normal tissue toxicity. Additionally, a TCP analysis was carried out in order to determine whether the overall change in local control effected by the directed and the indiscriminate dose escalation would be sufficiently different to prove either one concept, or both, of value.

8.1 Planning Study

A total of 13 out of the 15 patients listed in table 3.1 were included into this planning study. For patients # 2 and 4, no planning CT data were available. Details about the FMISO and FDG PET examinations can be found in sections 3.1.2 and 3.3.1. Patients were treated as explained in section 3.3.3. For each patient, three individual IMRT plans were created with the planning system Hyperion [1]: a conventional IMRT plan, a uniDE was applied to the FDG PET positive BTV and finally a plan, where a DPBN approach according to dynamic FMISO PET data was realized. For all three plans the same equivalent uniform dose (EUD) constraints were used. Hence, all final dose distributions had the same EUDs in the OARs. The advantage of this approach is that OARs were not compromised if the target goal was hard to achieve. Conversely, if the target dose could not be achieved a higher toxicity would have been necessary. The OAR that were taken into account generally were the spinal cord, the spinal cord extended by a safety margin of 3mm, the parotid glands and the non-specified normal tissue. Also in terms of beam angles, the same settings were used for the three different plans of a patient. Additionally, acute reactions were taken into account for the plan optimization: the weekly dose was limited to 12 Gy for all three branches.

8.1.1 Conventional IMRT

In each case individual planning target volumes (PTVs) of first, second and third order (PTV70, PTV60 and PTV54 respectively) were defined. The nominal prescription doses were 70, 60 and 54 Gy. A simultaneous integrated boost (SIB) technique allowed us to apply 60/54 Gy during the first 30 fractions to the PTVs of second and third order. An additional boost of 10 Gy in 5 fractions was then given to the PTV70. This type of conventional IMRT plan corresponds to the clinically applied dose distribution.

8.1.2 Uniform Dose Escalation

A second set of plans was created in order to apply a uniformly escalated dose to the FDG positive subarea of the PTV70. The FDG PET image was therefore manually matched to the planning CT. The FDG-avid BTV was defined as the region in the PTV70 containing FDG intensities higher than 40% of the maximum value. A dose escalation of 10%, respectively 77 Gy, was prescribed to this area. For this branch, also 35 fractions were used, so that uniDE was applied with a SIB technique. The dose prescriptions for the PTVs and the normal tissue constraints were the same as for the conventional IMRT plans.

8.1.3 Hypoxia Dose Painting by Numbers

In order to perform hypoxia DPBN, a map of locally varying dose escalation factors (DEF) was determined on the basis of dynamic FMISO PET scans. The analysis of this data was performed using a compartmental model described in chapter 5. The tumour control probability (TCP) model developed in the previous chapter assumes

$$\text{local cell survival } \sim \exp\left(\frac{b \cdot R_i}{P_i + P_0}\right) := M_i, \tag{8.1}$$

where R_i and P_i are the tracer retention and perfusion values for voxel i. b and P_0 are fit constants of the TCP model defined by

$$\ln(\text{TCP}) = \frac{\ln(\text{TCP}_0)}{V} \cdot \sum_{i=1}^{N} M_i. \tag{8.2}$$

In the above equation, TCP_0 denotes TCP in the case of a non hypoxic tissue, which is given by $-\ln(\text{TCP}_0) = N \cdot \exp(-\alpha_0 D_0)$. Here, α_0 is the tumour cell sensitivity in Gy^{-1} and D_0 the required dose for a normoxic

tumour tissue region in Gy. In the context of this study $\alpha_0 = 0.4$ Gy^{-1} and $D_0 = 70$ Gy were used. Assuming that the map of cell survival values reflects the degree of therapy resistance, the local dose escalation factor (DEF) for a given voxel i can be determined. Under the stipulation that the expected value of surviving cells is constant in all voxels, the DEF reads

$$\mathrm{DEF}_i = \frac{\alpha_0 D_0}{\alpha_0 D_0 - \ln(M_i)} = \frac{\alpha_i}{\alpha_0}. \tag{8.3}$$

This local DEF compensates for the mean cell sensitivity $< \alpha_i >_T$ of a voxel during the whole treatment time. Hence, the resulting DE is applied throughout the whole treatment course, starting from the first day of treatment.

The resulting map of DEFs was used for a gradual dose prescription. By virtue of the model, the DEFs are truncated at 1: $\mathrm{DEF}_i \geq 1.0$. In order to ensure accurate coregistration, the corresponding FMISO image acquired 2 h after tracer injection was manually matched to the planning CT. The determined transformation matrix was then applied to the respective DEF map, which is available in the same coordinate system as the 2 h pi FMISO scan.

8.1.4 Evaluation and Comparison of Treatment Plans

A statistical analysis of the DEFs associated to uniDE and DPBN was carried out. For DPBN, the mean DEF (DEF_{mean}) and the maximum DEF (DEF_{max}) were determined. Furthermore, the volume of the FDG-based BTV (V_{FDG}) was compared to the fractional tumour volumes associated with DEFs exceeding 1.05 ($V_{1.05}$), 1.1 ($V_{1.1}$) and 1.2 ($V_{1.2}$), respectively.

The three different treatment plans were compared based on dose volume histograms (DVHs). In order to evaluate the dose distributions in the target volumes, a comparison of characteristic DVH points is not possible as the DP prescriptions vary from one patient to another. Therefore, it was evaluated how the applied doses matched the prescribed doses according to the effective DVH method proposed in [2]. However, cumulative histograms - similar to DVHs - were determined that show the fractional volume which receives at least a certain percentage of the prescribed dose. To achieve this, the applied doses were weighted with the inverse of the local DEFs. This DVH transformation allows us to objectively compare the target coverage of treatment plans with different DE strategies.

Furthermore, TCP was calculated for different scenarios according to

$$-\ln(\mathrm{TCP}) = C \cdot \sum_{i=1}^{N} e^{-\alpha_i D_i}, \tag{8.4}$$

where α_i is the local cell sensitivity in Gy^{-1}, D_i the dose in Gy applied to voxel i and N is the number of voxels. The constant C equals voxel volume times number of cells per ccm and is determined from a fit to the patient population (cf. chapter 7). In a first step, ideal TCP (TCP_{ideal}) was estimated assuming that the tumour cell sensitivity α was spatially variable. FMISO mapping was supposed to reveal the sensitivity distribution in the tissue. Validity of the hypoxia TCP model introduced in chapter 7 was presumed. In addition, it was assumed that the required dose prescription $D_0 \cdot \alpha_0/\alpha_i$ could be achieved in all tumour voxels. To fulfill the dose requirements perfectly would imply a homogeneous cell survival probability and TCP would depend only on tumour volume. In contrast, the second TCP scenario (TCP_{real}) took into account that prescriptions could not be achieved perfectly. TCP_{real} was calculated using the realistic dose distributions obtained from the planning study. In general, TCP_{real} will be different from TCP_{ideal}. Usually TCP estimated for the realistic situation will be smaller. The third scenario evaluated the realistic dose distributions, but assumed a homogeneous tumour tissue, i.e. no deleterious influence of hypoxia. Here, $\alpha_i = \alpha_0$ was used everywhere so that the effect of a dose escalation created in the absence of hypoxia was estimated.

8.2 Results of the Planning Study

For all 13 patients, three different IMRT plans were created. For all plans, 7 or 8 fields were used. No FDG PET data were available for patients # 5 and 14. In these cases, the FMISO scans taken 2 h pi were used to define a BTV, which was also defined as the region including tumour voxels with FMISO intensities larger than 40% of the maximum.

The volumetric analysis for the two DE approaches, uniDE and DPBN, revealed a large bandwidth of volumes determined by the FDG positive area (V_{FDG}). V_{FDG} ranged from 7.32 to 94.34 cm^3, with a mean value of 37.79 cm^3. In most of the cases, the tumour region that receives 2.2 Gy per fraction (Gy/fx) would be too large to be clinically applicable. In contrast, the DPBN approach assigns doses in the order of 2.2 Gy/fx only to very small subvolumes of the tumour. In general, a DE of 10% was only observed for severely hypoxic areas, whereas regions of moderate hypoxia required DE factors lower than 1.1. Volumes that were for the DPBN approach associated to DEFs higher or equal than 1.1 ($V_{1.1}$) were in the range of 0 to 7.75 cm^3 (mean: 1.77 cm^3). In contrast volumes that received additional doses of 5% or more ($V_{1.05}$) were between 0 and 26.54 cm^3 large, with a mean volume of 7.42 cm^3. Five of the 13 patients required DEFs greater than 1.2 in small

Pat	**PTV70**	$\mathbf{V_{FDG}}$		$\mathbf{V_{1.05}}$		$\mathbf{V_{1.1}}$		$\mathbf{V_{1.2}}$	
#	[ccm]	[ccm]	[%]	[ccm]	[%]	[ccm]	[%]	[ccm]	[%]
1	450.4	67.12	14.90	2.81	0.62	0.22	0.05	0	0
3	288.7	36.42	12.61	17.12	5.93	7.75	2.68	1.84	0.64
5	314.4	93.83*	29.84	25.68	8.17	6.70	2.13	1.22	0.39
6	278.1	32.13	11.55	26.54	9.54	5.78	2.08	0.68	0.24
7	447.3	44.50	9.95	0.05	0.01	0	0	0	0
8	256.1	21.14	8.25	0	0	0	0	0	0
9	438.7	21.12	4.81	4.83	1.10	0.32	0.07	0	0
10	559.4	94.34	16.86	2.46	0.44	0.35	0.06	0.03	0.00
11	462.8	7.45	1.61	0.84	0.18	0.11	0.02	0.05	0.01
12	371.6	7.32	2.00	4.64	1.25	0.70	0.19	0	0
13	174.3	14.28	8.20	0.46	0.26	0	0	0	0
14	208.1	20.44*	9.82	3.54	1.70	0.49	0.23	0	0
15	266.8	31.21	11.70	7.51	2.81	0.62	0.23	0	0

Table 8.1: Volumetric analysis for the different types of dose prescriptions: volume PTV70, volumes of the FDG-avid BTVs (V_{FDG}) and DPBN sub-volumes associated to DEFs higher or equal 1.05 ($V_{1.05}$), 1.1 ($V_{1.1}$) or 1.2 ($V_{1.2}$) respectively, according to the FMISO-based DE map. Relative values given in brackets are normalized to the total PTV70 volume. *No FDG scan was available for patients # 5 and 14. The BTVs were defined on the basis of the FMISO PET acquired 2 h pi.

regions of the target. The detailed volumetric analysis for all patients is summarized in table 8.1.

The statistical analysis of the DEF determined for DPBN revealed a large variation of the maximum DEFs (DEF_{max}) among the considered patients. DEF_{max} ranged from 1.03 to 1.66. The mean values of the individual DEFs (DEF_{mean}) were in the range $1.01-1.03$ FDG-positive BTV. Table 8.2 shows DEF_{max} and DEF_{mean} values for each patient in detail. DPBN escalates the dose for most of the patients by less and also in a smaller sub-volume of the tumour. Hence, DPBN might constitute a more effective use of the radiation dose.

Figure 8.1 shows a histogram of the required DEFs for patient # 6. This histogram illustrates that the majority of tumour voxels requires DEFs lower than 1.1, only for a small number of voxels higher doses are prescribed.

Figure 8.2 exemplarily shows the dose distributions of the three different plans for one patient (# 6). For this patient, the dynamic FMISO data revealed large areas of severe hypoxia. This is the reason why in small subareas

Pat #	$\mathbf{DEF_{max}}$	$\mathbf{DEF_{mean}}^*$
1	1.198	1.010
3	1.415	1.019
5	1.664	1.021
6	1.350	1.030
7	1.052	1.006
8	1.033	1.008
9	1.172	1.011
10	1.229	1.006
11	1.264	1.007
12	1.190	1.018
13	1.072	1.004
14	1.185	1.016
15	1.145	1.019

Table 8.2: Maximum and mean DEFs for DPBN determined for each patient on the basis of dynamic FMISO PET data. *Mean value of DEFs referring to the FDG-volume.

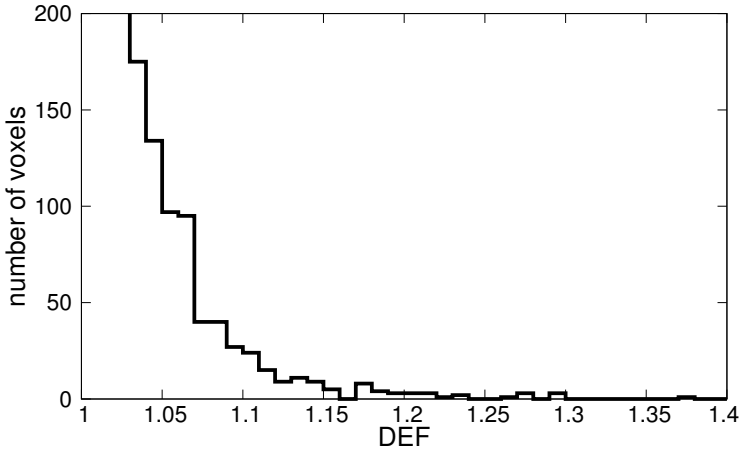

Figure 8.1: Histogram of DEFs for patient # 6.

of the PTV doses exceeding 82 Gy can be observed. The maximum DEF for this patient turned out to be 1.35. In contrast to other patients, the FDG positive area of this patient was quite irregular, which leads to a complicated prescription also in the case of uniDE. In the right column of figure 8.2 the corresponding DVHs are presented. The displayed DVHs for the OARs substantiate the isotoxicity constraint achieved for the three different branches.

A detailed DVH comparison of normal tissue doses is not necessary, since the whole study was defined requiring isotoxicity of the three plans (see also fig. 8.2). A comparison of the overall treatment doses that showed no significant increase of the integral dose neither for the uniDE approach nor for the DPBN plan. The total doses for both branches were in the order of $\pm 2\%$ relative to the conventional IMRT plan.

In order to evaluate the dose assigned to the target, a comparison of the cumulative histograms for the three plans of patient # 6 is displayed in figure 8.3 for the PTV of first order. Compared to the conventional IMRT plan, the uniDE showed a non-negligible part of the PTV where the dose prescription could not be fully realized. Underdosages are mainly observed at the edges of the FDG-positive area, where the prescription rises from 70 to 77 Gy. Generally, a lower target coverage was observed for the uniDE approach. In contrast, the requirement of DPBN was easier to fulfill. The target coverage of DPBN was only slightly worse than for the conventional IMRT plan. Nevertheless, if the DE maps become too heterogeneous, a precise application of the required dose might no longer be guaranteed. In table 8.3, a detailed list is given, that summarizes for all patients and for each of the three treatment modalities the percentage of target volume that receives at least 95, 100 or 105% of the prescribed dose.

Table 8.4 shows the detailed TCP analysis for the patient group. In the case of patient #2, TCP_{real} and TCP_0 were 0. This was probably due to the position of the PTV70, which presented regions overlapping with the spinal cord. In these areas, doses were reduced according to the normal tissue requirements. Therefore, also TCP decreased significantly.

The determined values for TCP_{ideal} revealed that the fraction of patients that is overtreated with uniDE is substantial. A large fraction of patients (e.g. # 8, 11, 12, 13 and 14) had already before the start of treatment TCP values of 0.8 and higher. A uniDE would not significantly improve the probability of tumour control for these patients. The marginal increase of TCP does not justify DEs of such magnitude. In contrast, for severely hypoxic tumours, which have initially very low TCPs (≤ 0.35), uniDE is not sufficient, a more focused application of the dose is needed. The TCP values for these patients (# 3, 5 and 6) show the high potential of DPBN.

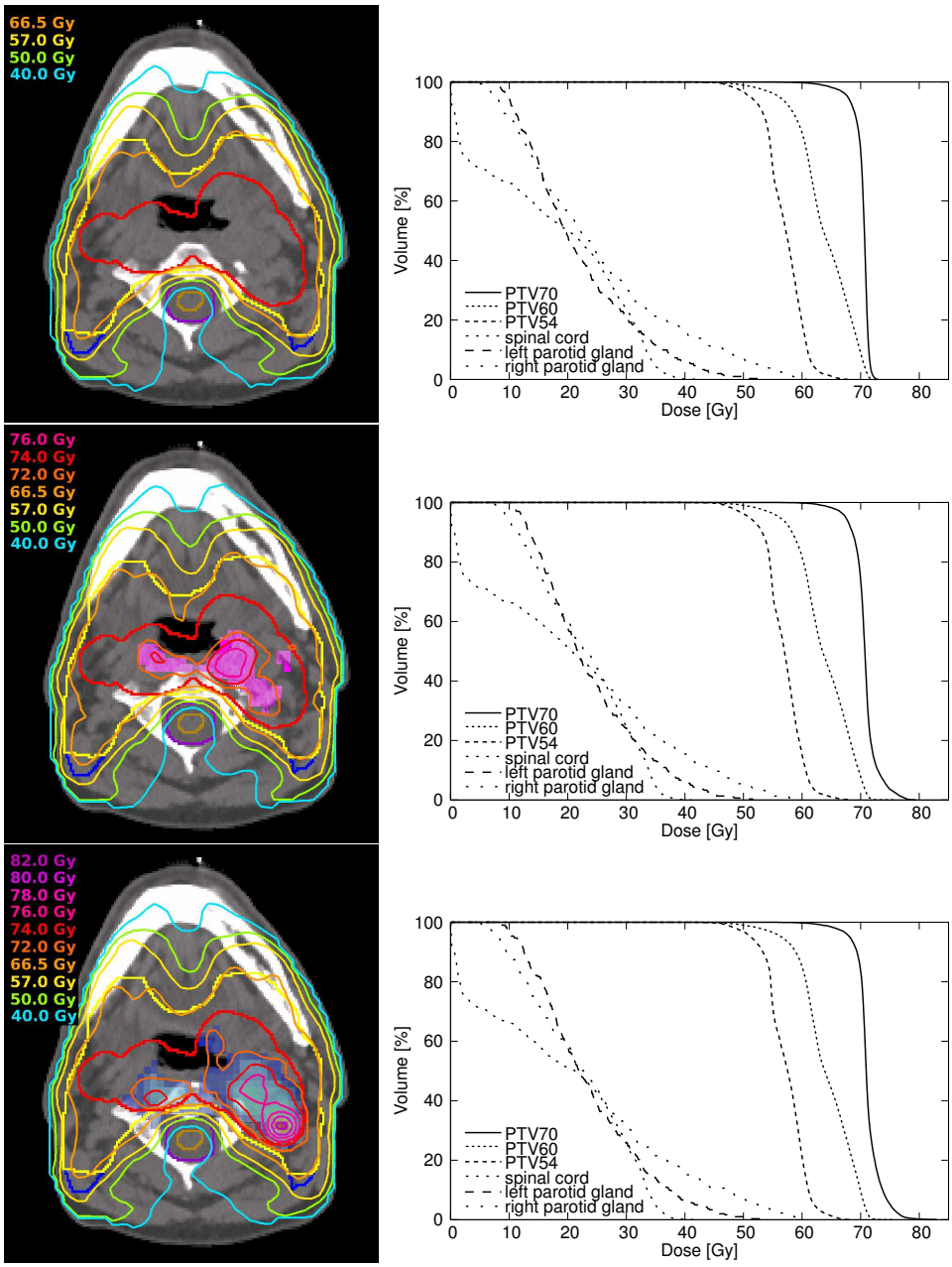

Figure 8.2: Dose distributions and corresponding DVHs for patient # 6. (a) Conventional IMRT plan. (b) uniDE to the FDG PET positive area shown in purple. (c) DPBN according to the superimposed DE map determined from dynamic FMISO PET scans. Volumes of interest: PTV70 (red), PTV60 (yellow), PTV54 (blue) and spinal cord (brown) and expanded spinal cord (purple).

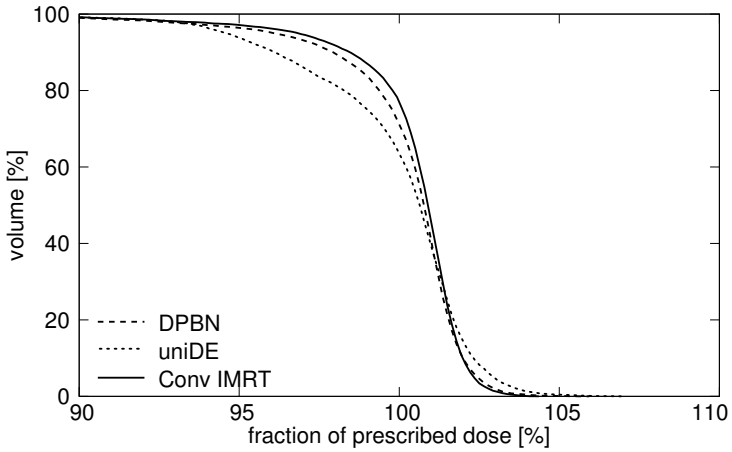

Figure 8.3: Target coverage of prescribed dose for patient # 6. The fraction of prescribed dose is displayed for the uniform DE and hypoxia DPBN in comparison the DVH of the conventional IMRT plan. The prescription of DPBN can be achieved better than uniDE.

Pat	**Conv**			**uniDE**			**DPBN**		
#	V_{95}	V_{100}	V_{105}	V_{95}	V_{100}	V_{105}	V_{95}	V_{100}	V_{105}
1	92.5	69.5	0	89.1	56.4	0.5	92.2	63.9	0
3	98.4	86.6	0	97.2	78.0	0.4	97.7	83.5	0.4
5	99.4	88.8	0	80.7	53.4	0.4	96.8	60.8	0.2
6	97.1	76.9	0	93.8	63.5	0.4	96.4	71.1	0.1
7	99.6	90.5	0	98.3	81.2	0.4	98.3	85.9	0
8	99.1	75.6	0	98.6	72.2	0.5	99.6	74.6	0
9	96.3	76.7	0	93.6	67.0	0.1	95.6	69.8	0
10	98.0	90.1	0	96.4	78.4	0.5	97.7	89.2	0
11	95.0	72.7	0	94.8	70.9	0.1	95.1	71.1	0
12	98.8	80.8	0	98.5	80.1	0	98.3	78.8	0
13	96.4	87.0	0	95.5	83.6	0.2	96.4	88.8	0
14	97.4	82.4	0.1	91.9	66.8	0.3	96.8	74.0	0
15	99.9	92.6	0.1	98.9	82.5	0.3	99.7	83.8	0

Table 8.3: Evaluation of target coverage: fractional volume (in %) that receives at least 95, 100 or 105% of the prescribed dose.

For patients where TCP for DPBN is higher than for uniDE, $DEF_{max} > 1.1$.

The major quality shown by the TCP values is the 15% increase in TCP_{real} when applying DPBN. Especially for patients with highly hypoxic tumours, which have very low probabilities of treatment success when treated with 70 Gy, DPBN seems to be highly promising. The comparison with uniDE, where only an increase of 2% is observed using the realistic dose distributions, shows evidence of the large benefit of DPBN. For those patients, the uniDE is not powerful enough to overcome hypoxia induced radioresistance.

The computation of TCP_0 revealed TCPs comparable to the conventional IMRT plan for both uniDE and DPBN. This is probably due to nearly unchanged overall doses. The TCP analysis also estimates, that in case of homogeneous tumour tissues, the dose escalation would not cause significant changes in TCP. In other words, the risks of treating with uniDE or DPBN are in the same order of magnitude.

8.3 Discussion

The presented work consists of a DP planning study that includes a group of 13 HNC patients. The aim of the study was to compare two different DE strategies, uniDE and DPBN, in a patient population while sticking to the requirement of isotoxicity. Previously published investigations either showed the feasibility of uniDE exemplarily for a single patient [13, 22] or studied the possibility of performing DPBN [2, 7]. The presented paper additionally estimates the possible gain in terms of TCP for the different therapy approaches.

The study revealed, that under the condition of isotoxicity, both DE methods are feasible. For the DPBN approach, the prescriptions could be realized in a larger region of the target than for uniDE. The lower grade of target coverage for uniDE is due to the fact, that the dose gradient always lies inside the BTV. Hence, by virtue of the prescription a complete coverage of the FDG-enriched region with 77.0 Gy can hardly be reached. In contrast, the DPBN strategy is based on a gradual dose prescription. This results in general in high grades of target coverage, if the DE map taken from dynamic FMISO data does not present too high gradients or consist of too patchy patterns.

Furthermore it turned out, that the areas of FDG enrichment which should receive additional 10% of dose had volumes up to 94 ccm. The volumes of the BTV were in most of the cases too large to be clinically acceptable because of the enhanced risk of acute reactions. In contrast, only small areas

Pat	$\mathbf{TCP_{ideal}}$			$\mathbf{TCP_{real}}$		
#	Conv	uniDE	DPBN	Conv	uniDE	DPBN
1	0.530	0.629	0.637	0.000	0.000	0.000
3	0.135	0.152	0.875	0.198	0.193	0.750
5	0.002	0.002	0.706	0.000	0.001	0.489
6	0.316	0.373	0.799	0.347	0.393	0.744
7	0.612	0.670	0.666	0.617	0.643	0.659
8	0.817	0.857	0.852	0.836	0.875	0.861
9	0.688	0.757	0.784	0.326	0.238	0.393
10	0.644	0.753	0.713	0.727	0.814	0.773
11	0.870	0.881	0.915	0.879	0.891	0.903
12	0.853	0.883	0.934	0.884	0.905	0.939
13	0.859	0.886	0.876	0.897	0.921	0.916
14	0.832	0.871	0.907	0.867	0.889	0.905
15	0.603	0.670	0.764	0.679	0.739	0.793
avg	**0.597**	**0.645**	**0.795**	**0.559**	**0.577**	**0.702**

Pat	$\mathbf{TCP_0}$			**outcome***	
#	Conv	uniDE	DPBN		
1	0.000	0.000	0.000	0	
3	0.791	0.809	0.827	0	
5	0.711	0.781	0.780	0	
6	0.793	0.808	0.869	0	
7	0.676	0.695	0.708	0	
8	0.869	0.896	0.886	1	
9	0.425	0.312	0.469	1	
10	0.783	0.845	0.808	1	
11	0.921	0.930	0.929	1	
12	0.946	0.953	0.962	1	
13	0.910	0.927	0.923	1	
14	0.927	0.940	0.942	1	
15	0.813	0.846	0.872	1	
avg	**0.744**	**0.749**	**0.767**	**0.615**	(obs.)

Table 8.4: TCP values calculated for different scenarios. TCP_{ideal}: TCP of an ideal situation, where all tumour voxels are irradiated with exactly the prescribed dose. TCP_{real}: TCP values determined for the real situation, assuming the established TCP-model is valid. TCP_0: TCP assuming the tumour tissue is homogeneous and nevertheless irradiated with the different DE treatment plans. *0: local recurrence, 1: no local recurrence.

received comparable radiation doses using the DPBN approach. In a large number of cases, the maximum DEFs did stay significantly below 1.1. Only in severely hypoxic areas, doses of 2.2 Gy/fx or higher were needed.

In the previous chapter, a TCP model was established [65] relating dynamic FMISO data with therapy outcome. This model formed the basis for the DE map used for DPBN. In addition, it allows us to estimate the potential benefit of the different DE strategies. The theoretically achievable increase in TCP was determined for both DE branches. Assuming full validity of the TCP model, a large fraction of patients would be overtreated by the use of uniDE. Especially in cases where the TCP values are high even without increasing the dose, the benefit of higher dose levels would be too small compared to the enhanced risk of acute toxic reactions.

Moreover, the analysis showed a potential increase in TCP of $\sim$ 15% for a population treated with DPBN, whereas the probability of treatment success rose only by 2% using the uniDE approach. For the TCP estimates, EUDs obtained from the planning study were included into the calculation. This difference in TCP observed for the population of 13 patients is a strong hint for the validity of using dynamic FMISO PET as a basis for DPBN. An estimation of TCPs assuming complete homogeneity of the tumour tissue shows no significant difference between the three treatment branches. Hence, DPBN based in dynamic FMISO PET revealed substantially more potential than uniDE.

Chapter 9

Design of a Randomized Clinical Study

The whole development of the dose painting method presented in the context of this thesis was done retrospectively. The design of the kinetic model in chapter 5 as well as the development of the TCP model, including the definition of the malignancy metric in chapter 7 was performed on the basis of a sample of 15 patient data sets.

The ultimate justification, especially of the TCP model, would be a prospective, randomized patient study. It was shown in chapter 6, that the malignancy value M was predictive for therapy outcome for the group of 15 patients.

A possible future patient study with dynamic FMISO PET will enable us to validate the hypothesis that high M-values predict low chances of therapy success, whereas low M-values correlate with high tumour control probabilities. In order to validate and further improve the statistical power of these promising findings, a larger patient study has to be carried out.

A hypoxia DP patient study for HNC will consist of the same functional imaging examinations as performed already during the present study. Each patient will undergo PET examinations with FMISO and FDG approximately one week before the start of treatment. The FMISO PET scan will be taken in dynamic acquisition mode, whereas for the FDG PET examination, static image acquisition will be sufficient.

According to the individual features of the FMISO TACs, assessed by a compartmental analysis, patients will be classified into three groups: non-hypoxic, moderately hypoxic and severely hypoxic tumours will be distinguished. The first group consists of patients with well perfused and non-hypoxic tumours, where no FMISO uptake is visible in the dynamic curves. These patients will receive a conventional IMRT treatment with 70 Gy. In

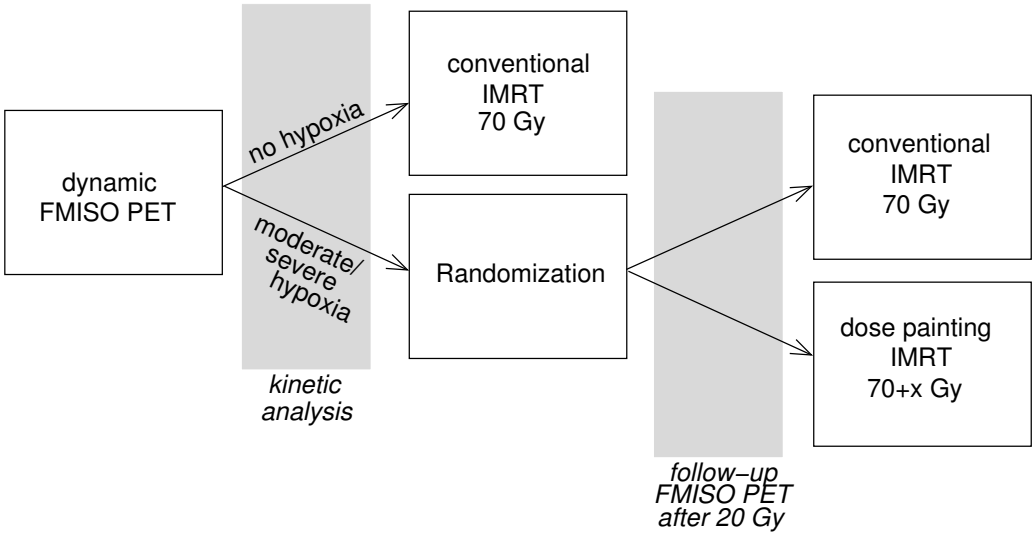

Figure 9.1: Schematical representation of the planned randomized clinical trial.

contrast, patients presenting with moderately to severely hypoxic tumours, which means high levels of tracer retention and possibly even low perfusion efficiencies of the tumours, will enter a randomized treatment with two different therapy arms. 50% of those patients will also be treated with conventional IMRT delivering a homogeneous dose of 70 Gy to the target, whereas a dose painting IMRT treatment will be applied to the second half of the patient group. Here, the tumour regions where a dose escalation is necessary will be determined by the analysis of the individual hypoxia-perfusion patterns and the value of the corresponding M-metric in the pre-treatment FMISO scans.

All patients which enter the randomized treatment arm, i.e. all patients presenting with moderately or severely hypoxic tumours in the pre-treatment examinations, will undergo a follow-up examination with dynamic FMISO PET after approximately two weeks of therapy (at $\approx$ 20 Gy).

Figure 9.1 schematically shows the design of this prospective randomized clinical trial.

Three main issues are addressed with this study:

- This study will be a proof of principle to validate the TCP model and also the predictive character of the malignancy value M. With the presented TCP model, it is possible to prospectively predict treatment success probabilities, which can then be compared to the observed outcome data. Patients entering the non-escalated treatment arm will be

of highest importance. Those patients will receive a comparable IMRT treatment and will therefore allow us to validate the hypothesis that patients presenting with low M-values have higher probabilities of progression free survival than patients with high M.

- Secondly, a larger patient study will enable us to further test the kinetic compartment model and to optimize the parameter values of the TCP model as a consequence of the greater number of data sets.

- Finally, patterns of failure may be analyzed for patients presenting with hypoxic tumours which do not receive any dose escalation. An investigation of the correlation of regions of failure and their functional characteristics are of great scientific interest. This type of analysis might give us deeper insights into the failure patterns in hypoxic tumours of HNC.

Chapter 10

Discussion

In the context of this work, a strategy to perform individually adapted RT treatment on the basis of functional hypoxia imaging was developed. The hypothesis that dynamic FMISO PET scans allow for the determination of the configuration of the tissue vasculature was investigated. The vascular configuration of a tumour is described by two different variables: The total capacity of the blood vessels and their spatial distribution. By using a kinetic model, these two variables can be assessed from the dynamic FMISO data. The configuration of the vascularity, especially the vascular 'mesh size', is responsible for the development of hypoxia, whereas the capacity of the vessels is the key to tumour reoxygenation. The grade of heterogeneity of a tissue is dictated by the vascularity. Hence, the grade of malignancy of a tumor tissue is determined by the degeneracy and complexity of the vascular system and governs treatment resistance.

The compartment model developed in chapter 5 involves a total of five open parameters. It allows to reproduce the complete spectrum of observed data curves. An important property of the compartment model is that it takes into account the long diffusion distances covered by the tracer molecules before a covalent binding in hypoxic regions can take place. Hence, FMISO probes intra-vascular distances. This feature, which is based on immunohistochemical observations [11, 30, 31, 38, 41] is not accounted for in the only model for transport and distribution of FMISO presented in literature so far [12]. The specific choice of the blood input function allows us to model in addition the varying composition of blood vessels and extravascular space of the tissue throughout the tumour. However, due to different reasons such as inaccuracies of the reconstruction algorithm, image fusion errors and statistical uncertainties of the physical positron decay process itself, the data curves are quite noisy. These various types of uncertainties cause subsequent errors in the parameter values. Additional sources for errors are intrinsically given

by the kinetic model, as it is not completely free of parameter covariances.

In general, both acute and chronic hypoxia can have a certain influence on the therapy resistance of a tumour. Acute and chronic hypoxia coexist in a tumour. Both phenomena result from the same cause, which is an insufficient, chaotic and spatially varying vascular system. Dynamic FMISO PET analyzed with a kinetic model measures not the symptom hypoxia, but its cause. The vascular system of a tumour can be sufficiently described by two parameters: (1) the total capacity of the vasculature and (2) the characteristic distance between adjacent vessels. Dynamic FMISO imaging allows us to accurately assess these two features. Hence, both types of hypoxia are accounted for in the presented model and also their influence on therapy outcome is taken into account intrinsically by the derived TCP model.

The model of tumour control presented in chapter 7 constitutes the key between the kinetic FMISO PET data analysis and therapy outcome data. The model requires a calibration with realistic outcome data to be clinically applicable. This calibration lacks a sufficiently large patient sample. Hence, the parameter values present with non-negligible inaccuracies. However, by virtue of its design, the TCP model is population averaged. The individual grade of therapy resistance may therefore deviate significantly from the population averaged TCPs due to the large inter- and intra-patient variability of tissue configuration and other tumour specific factors.

Finally, a main issue is the clinical feasibility of applying highly modulated radiation doses. In the context of this work, it could be shown that HIDE is theoretically feasible without compromising neither the organs at risk nor the surrounding non-specified normal tissue. The required DP prescriptions may not be perfectly translated into deliverable fluence profiles due to the finite size of the multi-leaf collimator. Also from a dosimetric point of view, the dose delivery for extremely varying radiation fields has to be guaranteed. However, from a clinical point of view, set-up errors and also internal organ movements or therapy induced tumour deformations are crucial points that need to be considered in the context of individually targeted RT approaches.

In contrast to dose painting strategies, there exist a number of alternative adapted therapy approaches in RT, such as ARCON (accelerated radiotherapy with carbogen and nicotinamide) [32] or pharmaceutical methods administering the radiosensitizers nimorazole [50] or tirapazamine [36, 59] in addition to RT. For each of these three approaches, the first clinical trials revealed promising results.

The ARCON concept [32] consists of an accelerated RT with two treatment fractions a day during which the patient breathes a gas enriched with oxygen and carbondioxide and injection of nicotinamide. Increased tumour control rates were reported by the investigators. However, carbogen breath-

ing induces a certain level of toxicity which in addition to hyperfractionated RT cannot be tolerated by a considerable fraction of patients.

Different pharmaceutical hypoxia modifiers are currently under clinical investigation. The Danish Head and Neck Cancer Study (DAHANCA 5) [50] reported increased survival rates for patients treated in addition to RT with the radiosensitizer nimorazole. In other studies, patients were treated with the radiosensitizer tirapazamine in addition to a standard radiochemotherapy [36, 59]. Here, the investigators found decreased rates of local failure for the patient group receiving the hypoxia modifying drug tirapazamine. Furthermore, they reported that tirapazamine acted by specifically targeting hypoxic cells and might therefore be an ideal drug for a hypoxia targeted therapy approach.

The present work concentrates on hypoxia image guided dose escalation (HIDE) as a possible method to overcome hypoxia-induced radioresistance. A major advantage of HIDE is the fact that no additional drugs are used. Therefore, there might be an increased possibility to control the side effects of the treatment. By virtue of the treatment design, HIDE does not compromise the normal tissue. Furthermore, increased doses will only be assigned to regions where it is absolutely necessary by applying dose painting by numbers.

Chapter 11

Summary and Outlook

The aim of including functional imaging data into the treatment planning process of RT is to perform a targeted RT which is adapted to the functional and biological characteristics of the tumour. In order to draw the link from functional PET imaging to adapted RT approaches, four main issues have to be addressed:

- The identification of the physical and biochemical processes that govern tracer uptake and distribution in the tumour tissue is imperative for the correct analysis and interpretation of functional PET data.
- Secondly, the microbiological factors affecting the radiation resistance of tumours have to be correlated to PET tracer retention.
- Only a model for tumour control as a function of the important biological imaging parameters can constitute the link between functional imaging data and adapted RT.
- Finally, the feasibility of a RT modification has to be investigated.

These four links were established in this thesis for the hypoxia PET tracer FMISO and hypoxia targeted *f*-IGRT.

In a first step, a kinetic model was derived to analyze the dynamic FMISO data on a voxel basis. This model served as a tool for the analysis and functional interpretation of dynamic FMISO PET patient data. It was derived from the general diffusion-reaction equation. The principal design of the model is based on the physical and biochemical processes that govern uptake and distribution of the tracer. It is able to reproduce the variety of observed FMISO data curves. It could be shown, that the shape of the dynamic FMISO data curves contain essential information about the local structural

architecture of the underlying tumour tissue. A kinetic analysis allows to determine characteristic parameter values to reliably describe the according tissue structure.

In a second step, two parameters were identified which are important for therapy outcome: The perfusion efficiency of the blood vessels and the tracer retention potential. These two parameters define the configuration of the local vasculature of the tumour. The perfusion efficiency is linked to the total capacity of the vasculature, whereas the level of tracer retention carries information about the spatial distribution of blood vessels. A two-dimensional method for the visualization of the two important parameters perfusion and tracer retention is given by scatter plots.

Three typical types of perfusion-retention scatter patterns were identified. The distribution of perfusion and retention values of a tumour turned out to be predictive for radiotherapy treatment outcome. A malignancy metric was defined in order to couple the two main kinetic parameters. This metric allowed for a highly significant stratification of the patient group with respect to treatment success ($p = 0.001$). Hence, evidently dynamic FMISO PET has a high prognostic value for RT in head-and-neck cancer.

A tumour control model which depends on the patient specific malignancy values is the key that translates functional imaging data into a dose prescription for an individually adapted RT. On the basis of clinical outcome data and repeated functional imaging data, a model for tumour control probability (TCP) was derived. This model is based on findings about characteristic therapy-induced changes of the scatter patterns. The model reflects reoxygenation as a progression to less malignant scatter patterns. The TCP model was calibrated by a fit to therapy outcome data observed in the patient group that entered the present study.

Finally, a RT planning study was carried out in order to investigate the feasibility of RT modification in a realistic setting. Radiation doses were prescribed spatially varying according to the TCP model. It was possible to apply higher doses to sub-volumes of the tumour without compromising the surrounding organs at risk. Hence, dose painting seems to be a very effective way of a functional RT modification. Dose painting was shown to be most effective for patients presenting with severely hypoxic and badly perfused tumours before the start of treatment. An estimation of the benefit to a population revealed a potential increase in TCP from 56 to 70%.

The response of vasculature and perfusion efficiency to radiation are most essential for therapy outcome. In addition, a fast reoxygenation of an initially hypoxic tumour is good for therapy outcome, whereas a slow reoxygenation has a negative effect on therapy success. Two quantities can be determined from the vascular configuration of a tumour: The overall number and the

capacity of blood vessels in addition to the spatial distribution of the vascularity, i.e. the homogeneity or heterogeneity of the vascular system. Dynamic FMISO PET enables to measure the capacity of blood vessels directly, whereas the spatial distribution is measured indirectly via tracer retention in large pouches between adjacent vessels. The presented work allowed us to validate two essential hypotheses: (1) Dynamic image acquisition captures more information than static PET scans do and (2) a dynamic FMISO pre-treatment scan may be enough to estimate the probability of treatment success for a patient and to accordingly adapt RT.

This work presents a complete junction between functional imaging with FMISO PET and a biologically adapted radiotherapy strategy. Only by applying a kinetic model to the dynamic PET data, the vascular configuration of the tumour can be investigated. The correlation between the vascular configuration and the chance for a successful treatment is the key for an evidence based biologically adapted treatment. These promising results emphasize the value of dynamic FMISO PET imaging for clinical hypoxia dose painting in HNC. The next step to establish an evidence based concept for *f*-IGRT will be a patient study defined on the basis of the results of this study.

Bibliography

[1] M Alber and C Belka. A normal tissue dose response model of dynamic repair processes. *Phys Med Biol*, 51:153–172, 2006.

[2] M Alber, F Paulsen, SM Eschmann, and H-J Machulla. On biologically conformal boost dose optimization. *Phys Med Biol*, 48:N31–N35, 2003.

[3] RJ Barlow. *Statistics: A Guide to the Use of Statistical Methods in the Physical Sciences*. John Wiley & Sons, Chichester, 1989.

[4] AC Begg. Cell proliferation in tumours. In GG Steel, editor, *Basic clinical radiobiology*, pages 14–23. Arnold, London, 2nd edition, 1997.

[5] R Bender, S Lange, and A Ziegler. Wichtige Signifikanztests. *Dtsch Med Wochenschr*, 127:T1–T3, 2002.

[6] L Bentzen, S Keiding, M Nordsmark, L Falborg, SB Hansen, J Keller, OS Nielsen, and J Overgaard. Tumour oxygenation assessed by ^{18}F-fluoromisonidazole PET and polarographic needle electrodes in human soft tissue tumours. *Radiother Oncol*, 67:339–344, 2003.

[7] SM Bentzen. Theragnostic imaging for radiation oncology: dose-painting by numbers. *Lancet Oncol*, 6(2):112–117, 2005.

[8] JGD Birkmayer. *Tumorbiologie: Eine Einführung in die Biologie von Krebszellen*. Karger, Wien, 1984.

[9] DM Brizel, GS Sibley, LR Prosnitz, RL Scher, and MW Dewhirst. Tumor hypoxia adversely affects the prognosis of carcinoma of the head and neck. *Int J Radiat Oncol Biol Phys*, 38(2):285–289, 1997.

[10] IN Bronstein, KA Semendjajew, G Musiol, and H Mühlig. *Taschenbuch der Mathematik*. Verlag Harri Deutsch, Frankfurt, 1999.

[11] J Bussink. *The tumor microenvironment and effects of hypoxia modification*. PhD thesis, University of Nijmegen, The Netherlands, 2000.

[12] JJ Casciari, MM Graham, and JS Rasey. A modeling approach for quantifying tumor hypoxia with [F-18]fluoromisonidazole PET time-activity data. *Med Phys*, 22(7):1127–1139, 1995.

[13] KS Chao, WR Bosch, S Mutic, JS Lewis, F Dehdashti, MA Mintun, JF Dempsey, CA Perez, JA Purdy, and MJ Welch. A novel approach to overcome hypoxic tumour resistance: Cu-ATSM-guided intensity-modulated radiation therapy. *Int J Radiat Oncol Biol Phys*, 49(4):1171–1182, 2001.

[14] DJ Chaplin, MR Horsman, MJ Trotter, and DW Siemann. Therapeutic Significance of Microenvironmental Factors. In M Molls and P Vaupel, editors, *Blood Perfusion and Microenvironment of Human Tumors*, pages 133–143. Springer, Berlin, Heidelberg, New York, 2000.

[15] CN Coleman, JB Mitchell, and K Camphausen. Tumor Hypoxia: Chicken, Egg, or a Piece of the Farm? (editorial). *J Clin Oncol*, 20:610–615, 2002.

[16] DR Cox and EJ Snell. Analysis of Binary Data. In DR Cox, DV Hinkley, D Rubin, and BW Silverman, editors, *Monographs on Statistics and Applied Probability*, volume 32. Chapman and Hall, London, 2nd edition, 1989.

[17] J Denekamp and A Dasu. Inducible Repair and the Two Forms of Tumour Hypoxia – Time for a Paradigm Shift. *Acta Oncol*, 38(7):903–918, 1999.

[18] S-M Eschmann, F Paulsen, M Reimold, H Dittmann, S Welz, G Reischl, H-J Machulla, and R Bares. Prognostic Impact of Hypoxia Imaging with ^{18}F-Misonidazole PET in Non-Small Cell Lung Cancer and Head and Neck Cancer Before Radiotherapy. *J Nucl Med*, 46:253–260, 2005.

[19] SM Eschmann, G Friedel, F Paulsen, W Budach, C Harer-Mouline, BM Dohmen, and R Bares. FDG PET for staging of advanced non-small cell lung cancer prior to neoadjuvant radio-chemotherapy. *Eur J Nucl Med Mol Imaging*, 29(6):804–808, 2002.

[20] A Fyles, M Milosevic, D Hedley, M Pintilie, W Levin, L Manchul, and RP Hill. Tumor Hypoxia has Independent Predictor Impact Only in Patients With Node-Negative Cervix Cancer. *J Clin Oncol*, 20:680–687, 2002.

[21] LH Gray, AD Conger, M Ebert, S Hornsey, and OCA Scott. The concentration of oxygen dissolved in tissues at the time of irradiation as a factor in radiotherapy. *Br J Radiology*, 26:638–648, 1953.

[22] A-L Grosu, M Piert, and M Molls. Experience of PET for target localisation in radiation oncology. *Br J Radiol*, Supplement 28:18–32, 2005.

[23] KO Hicks, SJ Ohms, PL van Zijl, WA Denny, PJ Hunter, and WR Wilson. An experimental and mathematical model for the extravascular transport of a DNA intercalator in tumours. *Br J Cancer*, 76(7):894–903, 1997.

[24] RJ Hicks, D Rischin, R Fisher, D Binns, AM Scott, and LJ Peters. Utility of FMISO PET in advanced head and neck cancer treated with chemoradiation incorporating a hypoxia-targeting chemotherapy agent. *Eur J Nucl Med Mol Imaging*, 32(12):1384–1391, 2005.

[25] M Höckel, C Knoop, K Schlenger, B Vorndran, PG Knapstein, and P Vaupel. Intratumoural pO_2 predicts survival in advanced cancer of the uterine cervix. *Radiother Oncol*, 26:35–50, 1993.

[26] M Höckel and P Vaupel. Biological Consequences of Tumor Hypoxia. *Semin Oncol*, 28(suppl 8):36–41, 2001.

[27] M Höckel and P Vaupel. Tumor Hypoxia: Definitions and Current Clinical, Biologic, and Molecular Aspects. *J Natl Cancer Inst*, 93:266–276, 2001.

[28] MR Horsman and J Overgaard. The oxygen effect. In GG Steel, editor, *Basic clinical radiobiology*, pages 133–140. Arnold, London, 2nd edition, 1997.

[29] RK Jain. Transport of molecules in the tumor interstitium: A review. *Cancer Res*, 47:3039–3051, 1987.

[30] HL Janssen, KMG Haustermans, D Sprong, G Blommestijn, I Hofland, FJ Hoebers, E Blijweert, JA Raleigh, GL Semenza, MA Varia, AJ Balm, MF van Velthuysen, P Delaere, R Sciot, and AC Begg. HIF-1A, pimonidazole, and iododeoxyuridine to estimate hypoxia and perfusion in human head-and-neck tumours. *Int J Radiat Oncol Biol Phys*, 54(5):1537–1549, 2002.

[31] HL Janssen, FJ Hoebers, D Sprong, L Goethals, KJ Williams, IJ Stratford, HM Haustermans, AJ Balm, and AC Begg. Differentiation-associated staining with anti-pimonidazole antibodies in head and neck tumours. *Radiother Oncol*, 70:91–97, 2004.

[32] JHAM Kaanders, J Bussink, and A van der Kogel. ARCON: a novel biology-based approach in radiotherapy. *Lancet Oncol*, 3:728–737, 2002.

[33] W-J Koh, JS Rasey, ML Evans, JR Grierson, TK Lewellen, MM Graham, KA Krohn, and TW Griffin. Imaging of hypoxia in human tumours with [F-18]fluoromisonidazole. *Int J Radiat Oncol Biol Phys*, 22(1):199–212, 1992.

[34] MA Konerding, C van Ackern, E Fait, F Steinberg, and C Streffer. Morphological Aspects of Tumor Angiogenesis and Microcirculation. In M Molls and P Vaupel, editors, *Blood Perfusion and Microenvironment of Human Tumors*, pages 5–17. Springer, Berlin, Heidelberg, New York, 2000.

[35] C Laubenbacher and M Schwaiger. The Potential Role of Positron Emission Tomography in Investigation of Microenvironment. In M Molls and P Vaupel, editors, *Blood Perfusion and Microenvironment of Human Tumors*, pages 161–191. Springer, Berlin, Heidelberg, New York, 2000.

[36] QT Le, A Taira, S Budenz, M Jo Dorie, DR Goffinet, WE Fee, R Goode, D Bloch, A Koong, J Martin Brown, and HA Pinto. Mature results from a randomized Phase II trial of cisplatin plus 5-fluorouracil and radiotherapy with or without tirapazamine in patients with resectable Stage IV head and neck squamous cell carcinomas. *Cancer*, 106(9):1940–1949, 2006.

[37] CC Ling, J Humm, S Larson, H Amols, Z Fuks, S Leibel, and JA Koutcher. Towards multidimensional radiotherapy (MD-CRT): biological imaging and biological conformality. *Int J Radiat Oncol Biol Phys*, 47(3):551–560, 2000.

[38] A Ljungkvist. *Imaging the tumor microenvironment: The Dynamics and Modification of Hypoxia*. PhD thesis, Umeå University, Sweden, 2003.

[39] AS Ljungkvist, J Bussink, JH Kaanders, PF Rijken, AC Begg, JA Raleigh, and AJ van der Kogel. Hypoxic cell turnover in different solid tumor lines. *Int J Radiat Oncol Biol Phys*, 62(4):1157–1168, 2005.

[40] AS Ljungkvist, J Bussink, JH Kaanders, NE Wiedenmann, R Vlasman, and AJ van der Kogel. Dynamics of Hypoxia, Proliferation and Apoptosis after Irradiation in a Murine Tumor Model. *Radiat Res*, 165:326–336, 2006.

[41] ASE Ljungkvist, J Bussink, PFJW Rijken, JH Kaanders, AJ van der Kogel, and J Denekamp. Vascular architecture, hypoxia, and proliferation in first-generation xenografts of human head-and-neck squamous cell carcinomas. *Int J Radiat Oncol Biol Phys*, 54(1):215–228, 2002.

[42] J Logan. Graphical Analysis of PET Data Applied to Reversible and Irreversible Tracers. *Nucl Med Biol*, 27:661–670, 2000.

[43] J Logan. A review of graphical methods for tracer studies and strategies to reduce bias. *Nucl Med Biol*, 30:833–844, 2003.

[44] H-J Machulla. *Imaging of Hypoxia*. Kluwer Academic Publishers, Dordrecht, Boston, London, 1999.

[45] TJ McMillan and GG Steel. DNA damage and cell killing. In GG Steel, editor, *Basic clinical radiobiology*, pages 58–69. Arnold, London, 2nd edition, 1997.

[46] K Meyberg and P Vachenauer. *Höhere Mathematik 2. Differentialgleichungen, Funktionentheorie, Fourier-Analysis, Variationsrechnung*. Springer, Berlin, Heidelberg, New York, 1997.

[47] JD Murray. *Mathematical Biology*. Springer, Berlin, Heidelberg, New York, 1989.

[48] M Nordsmark and J Overgaard. A confirmatory prognostic study on oxygenation status and loco-regional control in advanced head and neck squamous cell carcinoma treated by radiation therapy. *Radiother Oncol*, 57:39–43, 2000.

[49] M Nordsmark, M Overgaard, and J Overgaard. Pretreatment oxygenation predicts radiation response in advanced squamous cell carcinoma of the head and neck. *Radiother Oncol*, 41:31–39, 1996.

[50] J Overgaard, JG Eriksen, M Nordsmark, J Alsner, and MR Horsman. Plasma osteopontin, hypoxia, and response to the hypoxia sensitiser nimorazole in radiotherapy of head and neck cancer: results from the DAHANCA 5 randomised double-blind placebo-controlled trial. *Lancet Oncol*, 6(10):757–764, 2005.

[51] N Paudit, M Gonen, L Krug, and SM Larson. Prognostic value of [^{18}F]FDG-PET imaging in small cell lung cancer. *Eur J Nucl Med Mol Imaging*, 30:78–84, 2003.

[52] GA Plataniotis, M-E Theofanopoulou, A Kalogera-Fountzila, A Haritanti, E Ciuleanou, N Ghilezan, N Zamboglou, A Dimitriadis, I Sofroniadis, and G Fountzilas. Prognostic impact of tumor volumetry in patients with locally advanced head-and-neck carcinoma (non-nasopharyngeal) treated by radiotherapy alone or combined radiochemotherapy in a randomized trial. *Int J Radiat Oncol Biol Phys*, 59(4):1018–1026, 2004.

[53] JPW Pluim, JBA Maintz, and MA Viergever. Mutual information based registration of medical images: a survey. *IEEE Transactions on Medical Imaging*, 22(8):986–1004, 2003.

[54] WH Press, SA Teukolsky, WT Vetterling, and BP Flannery. *Numerical Recipes in C: The Art of Scientific Computing*. Cambridge University Press, 2nd edition, 1992.

[55] JG Rajendran, DA Mankoff, F O'Sullivan, LM Peterson, DL Schwartz, EU Conrad, AM Spence, M Muzi, DG Farwell, and KA Krohn. Hypoxia and Glucose Metabolism in Malignant Tumors: Evaluation by [18F]Fluoromisonidazole and [18F]Fluorodeoxyglucose Positron Emission Tomography Imaging. *Clin Cancer Res*, 10(7):2245–2252, 2004.

[56] JG Rajendran, DC Wilson, EU Conrad, LM Peterson, JD Bruckner, JS Rasey, LK Chin, PD Hofstrand, JR Grierson, JF Eary, and KA Krohn. [18F]FMISO and [18F]FDG PET imaging in soft tissue sarcomas: correlation of hypoxia, metabolism and VEGF expression. *Eur J Nucl Med Mol Imaging*, 30(5):695–704, 2003.

[57] JS Rasey, W-J Koh, ML Evans, LM Peterson, TK Lewellen, MM Graham, and KA Krohn. Quantifying regional hypoxia in human tumours with positron emission tomography of [^{18}F]fluoromisonidazole: A pretherapy study of 37 patients. *Int J Radiat Oncol Biol Phys*, 36(2):417–428, 1996.

[58] JS Rasey, NJ Nelson, L Chin, ML Evans, and Z Grunbaum. Characteristics of the binding of labeled fluoromisonidazole in cells in vitro. *Radiat Res*, 122(3):301–308, 1990.

[59] D Rischin, RJ Hicks, R Fisher, D Binns, J Corry, S Porceddu, and LJ Peters. Prognostic significance of [18F]-misonidazole positron emission

tomography-detected tumor hypoxia in patients with advanced head and neck cancer randomly assigned to chemoradiation with or without tirapazamine: a substudy of Trans-Tasman Radiation Oncology Group Study 98.02. *J Clin Oncol*, 24(13):2098–2104, 2006.

[60] A Saleem, N Charnley, and P Price. Clinical molecular imaging with positron emission tomography. *Eur J Cancer*, 42:1720–1727, 2006.

[61] H Stöcker. *Taschenbuch der Physik*. Verlag Harri Deutsch, Frankfurt, 1998.

[62] K Tanderup, DR Olsen, and C Grau. Dose Painting: Art or science? *Radiother Oncol*, 79:245–248, 2006.

[63] RH Thomlinson and LH Gray. The histological structure of some human lung cancers and the possible implications for radiotherapy. *Br J Cancer*, 9(4):539–549, 1955.

[64] D Thorwarth, SM Eschmann, F Paulsen, and M Alber. A kinetic model for dynamic [^{18}F]-Fmiso PET data to analyse tumour hypoxia. *Phys Med Biol*, 50:2209–2224, 2005.

[65] D Thorwarth, SM Eschmann, J Scheiderbauer, F Paulsen, and M Alber. Kinetic analysis of dynamic 18F-fluoromisonidazole PET correlates with radiation treatment outcome in head-and-neck cancer. *BMC Cancer*, 5:152, 2005.

[66] B Vanderstraeten, W Duthoy, W De Gersem, W De Neve, and H Thierens. [^{18}F]fluoro-deoxy-glucose positron emission tomography ([^{18}F]FDG-PET) voxel intensity-based intensity-modulated radiation therapy (IMRT) for head and neck cancer. *Radiother Oncol*, 79:249–258, 2006.

[67] P Vaupel, F Kallinowski, and P Okunieff. Blood Flow, Oxygen and Nutrient Supply, and Metabolic Microenvironment of Human Tumors: A Review. *Cancer Res*, 49:6449–6465, 1989.

[68] P Viola and WM Wells. Alignment by Maximization of Mutual Information. *Int J Comp Vision*, 24(2):137–154, 1997.

[69] RL Wahl. *Principles and Practice of Positron Emission Tomography*. Lippincott Williams & Wilcons, Philadelphia, 2002.

[70] M Weinmann, C Belka, and L Plasswilm. Tumour hypoxia: impact on biology, prognosis and treatment of solid malignant tumours. *Onkologie*, 27(1):83–90, 2004.

[71] M Weinmann, V Jendrossek, D Guner, B Goecke, and C Belka. Cyclic exposure to hypoxia and reoxygenation selects for tumor cells with defects in mitochondiral apoptotic pathways. *FASEB*, 18(15):1906–1908, 2004.

[72] RJ Wong, DT Lin, H Schöder, SG Patel, M Gonen, S Wolden, DG Pfister, JP Shah, SM Larson, and DH Kraus. Diagnostic and Prognostic Value of [^{18}F]Fluorodeoxyglucose Positron Emission Tomography for Recurrent Head and Neck Squamous Cell Carcinoma. *J Clin Oncol*, 20:4199–4208, 2002.

[73] A Ziegler, S Lange, and R Bender. Überlebenszeitanalyse: Eigenschaften der Kaplan-Meier Methode. *Dtsch Med Wochenschr*, 127:T14–T16, 2002.

[74] A Ziegler, S Lange, and R Bender. Überlebenszeitanalyse: Der Log-Rang-Test. *Dtsch Med Wochenschr*, 129:T4–T6, 2004.

Acknowledgments

I want to express my deepest gratitude to Markus Alber, who was during the whole time a mentor, teacher and friend to me. Without him, his visions, his enthusiasm and idealism, this work would not have been possible.

My special thanks go to Martin Soukup, who shared not only the office with me, but also joys and sorrows and all kinds of food. I will never forget our discussions on political, religious and also scientific topics.

I kindly thank the whole group of Biomedical Physics in Tübingen, who made this time a good time. I also wish to thank Bettina Frey who always had an open ear for me and Gustav Meedt for long and inspiring discussions. Thanks also to Christoph Baum whose colourful qt-figures facilitated my work a lot.

Furthermore, I wish to thank Susanne-Martina Eschmann and Frank Paulsen for sharing essential data and knowledge, which were so important for this work.

I am very grateful for all the support of my husband Harald. Thanks to my parents and family, who always believed in me.

Appendix A

A kinetic model for dynamic [^{18}F]-Fmiso PET data to analyse tumour hypoxia

published in
Physics in Medicine and Biology 2005; **50**: 2209-2224

INSTITUTE OF PHYSICS PUBLISHING PHYSICS IN MEDICINE AND BIOLOGY

Phys. Med. Biol. **50** (2005) 2209–2224 doi:10.1088/0031-9155/50/10/002

A kinetic model for dynamic [^{18}F]-Fmiso PET data to analyse tumour hypoxia

Daniela Thorwarth[1], **Susanne M Eschmann**[2], **Frank Paulsen**[3] **and Markus Alber**[1]

[1] Section for Biomedical Physics, University Hospital for Radiation Oncology, Hoppe-Seyler-Str. 3, 72076 Tübingen, Germany
[2] Department of Nuclear Medicine, Radiological University Clinic, Otfried-Müller-Str. 14, 72076 Tübingen, Germany
[3] Department of Radiation Therapy, University Hospital for Radiation Oncology, Hoppe-Seyler-Str. 3, 72076 Tübingen, Germany

E-mail: daniela.thorwarth@med.uni-tuebingen.de

Received 22 November 2004, in final form 9 February 2005
Published 27 April 2005
Online at stacks.iop.org/PMB/50/2209

Abstract

A method is presented to identify and quantify hypoxia in human head-and-neck tumours based on dynamic [^{18}F]-Fmiso PET patient data, using a model for the tracer transport. A compartmental model was developed, inspired by recent immunohistochemical investigations with the tracer pimonidazole. In order to take the trapping of the tracer and the diffusion in interstitial space into account, the kinetic model consists of two compartments and a specific input function. This voxel-based data analysis allows us to decompose the time-activity curves (TACs) into their perfusion, diffusion and hypoxia-induced retention components. This characterization ranges from well perfused tumours over diffusion limited hypoxia to strong hypoxia and necrosis. The overall shape of the TAC and the model parameters may point at the structural architecture of the tissue sample. The model addresses the two main problems associated with hypoxia imaging with PET. Firstly, the hypoxic areas are spatially separated from well perfused vessels, causing long diffusion times of the tracer. Secondly, tracer uptake occurs only in viable hypoxic cells, which constitute only a small subpopulation in the presence of necrosis. The resulting parameters such as the concentration of hypoxic cells and the perfusion are displayed in parameter plots ('hypoxia map'). Quantification of hypoxia performed with the presented kinetic model is more reliable than a criterion based on static standardized uptake values (SUV) at an early timepoint, because severely hypoxic/necrotic tissues show low uptake and are thus overlooked by SUV threshold identification. The derived independent measures for perfusion and hypoxia may provide a basis for individually adapted treatment planning.

(Some figures in this article are in colour only in the electronic version)

1. Introduction

Hypoxia in tumours, as measured by polarographic Eppendorf pO_2 histographs, has been associated with poor treatment outcome and survival (Nordsmark *et al* 1996, 2000). Thus, to measure and quantify hypoxia may be beneficial for patient selection or treatment modification. Individually adapted treatment strategies to overcome this therapy resistance, such as ARCON (Kaanders *et al* 2002) or hypoxia dose painting (Alber *et al* 2003), appear necessary and promising.

There have been several attempts to quantify tumour hypoxia with polarographic needle electrodes (Nordsmark *et al* 1996, 2000) or with positron emission tomography (PET) by using hypoxia-specific tracer molecules such as [^{60}Cu]-ATSM (Chao *et al* 2001), [^{18}F]-Fluoroerythronitroimidazole (FETNIM) (Lehtiö *et al* 2004), [^{18}F]-Fluoroazomycin (FAZA) (Machulla 1999) or [^{18}F]-Fluoromisonidazole (Fmiso) (Koh *et al* 1992, Rasey *et al* 1996).

Fmiso binds selectively to macromolecules in hypoxic cells. At low oxygen levels, the compound is reduced and binds, when reduced by a second electron, covalently to intracellular macromolecules. In the presence of oxygen, the favoured reaction is the re-oxygenation to the less reactive parent compound which is freely diffusible and clears from tissue (Laubenbacher and Schwaiger 2000).

Koh *et al* (1992) and Rasey *et al* (1996) developed a strategy for the identification and quantification of hypoxic tumour areas on the basis of Fmiso PET images. They pointed out the necessity of very long (2–4 h) examination protocols because of the slow transport and reaction mechanisms of the tracer molecules. These investigators defined a fractional hypoxic tumour volume which is the proportion of the tumour area presenting a tumour-to-blood activity ratio $\geqslant 1.4$ at 2–3 h post injection (p.i.). Their results displayed a highly variable character of human tumour hypoxia among different tumours and also among regions within the same tumour. A study by Bentzen *et al* (2003) reports on an unclear correlation between Fmiso PET scans and direct oxygen measurements with polarographic needle electrodes.

Casciari *et al* (1995) developed a kinetic compartment model for the transport and metabolism of Fmiso. This model aims to determine the cellular Fmiso reaction rate constant from time-activity data, which is assumed to reflect the mean local oxygen concentration. It consists of four compartments with a high number of free parameters. Hence, a certain number of parameters have to be fixed to increase the robustness of the model. The model is a classical kinetic model where the different compartments co-exist in the same volume. This is problematic because it assumes homogeneous oxygen concentration which contradicts the observation of concentration gradients in a tissue.

Fortunately, the pattern of tracer accumulation in hypoxic tumours can be made visible by histological investigations with the related compound pimonidazole. Ljungkvist *et al* (2002) and Janssen *et al* (2002, 2004) investigated the structural architecture of hypoxic tumours with pimonidazole. These studies depict hypoxic islands interspersed throughout the tissue on length scales between 100 and 500 μm, located in regions far from blood vessels and including necrotic tissue. A 'hypoxia signal' on macroscopic length scales (size of PET voxels: $4 \times 4 \times 4.25$ mm^3) emerges from an irregular heterogeneous distribution of tracer accumulation on microscopic length scales.

The essential fact that hypoxia exists spatially separated and at any rate far from perfused vessels was not explicitly taken into account by Casciari *et al* (1995). Also, it becomes evident that the total sub-volume which traps the tracer is rather small. These observations are typical of the problem and serve to make the point that hypoxia-PET imaging with any arbitrary tracer is more ambiguous and intricate than with tracers with an active transport mechanism and

Table 1. Table of acquired image frames for each patient ($n = 16$).

Time p.i. (min)	0–2	2–4	4–15	15–60	120	180	240
Acquisition time	12 × 10 s	8 × 15 s	11 × 60 s	9 × 5 min	1 × 5 min	1 × 8–9 min	1 × 10–12 min
Patient no.							
1, 4	×	×	×	×	×	×	×
3, 5, 7, 9, 10, 12, 13, 15	×	×	×	–	×	–	×
8	×	×	×	–	×	×	×
11, 16	×	×	×	×	×	–	×
2, 14	×	×	×	3 × 5 min	×	–	×
6	×	×	×	5 × 5 min	×	–	×

higher reaction rates, such as FDG, and to justify that some model is required to interpret the images.

The immunohistochemical studies also revealed large inter- and intra-patient differences in regard to tumour tissue vasculature. Hypoxia is only a consequence of the irregular geometry of the tumour vasculature. Therefore, it is essential that the model for the transport of the tracer from the perfused vessels to the hypoxic cell is general enough to include both the irregular tumour geometry and the inter-individual tumour heterogeneity.

In the following, a method to quantify hypoxia in tumours based on dynamic [^{18}F]-Fmiso PET patient data is presented. The kinetic model assumes physical, purely diffusive transport of the tracer molecule to the hypoxic cell, where it is trapped according to the local oxygen tension. The application of the model to patient data time-activity curves (TACs) yields the local concentration of hypoxic sub-volumes in each tumour voxel, allowing us to display the results in a parameter plot ('hypoxia map').

2. Methods and materials

2.1. Patient data

The dynamic PET data in this study were obtained from patients with head-and-neck tumours who were examined with the following protocol: with the start of the image acquisition, a tracer activity of $A_0 \simeq 400$ MBq Fmiso was injected. For the first 15–60 min, the PET scanner (Advance, General Electric, Milwaukee, US) was running in dynamic acquisition mode which resulted in a total of 31–40 image frames. Additionally, two static images were taken for all patients 2 and 4 h p.i. and for a few patients also at 3 h p.i. Detailed information about time points and corresponding acquisition durations for each examined patient ($n = 16$) are summarized in table 1.

A decay correction for the decomposition of the radioactive ^{18}F was performed for all data sets. The raw PET data were stored in three separate data sets, one dynamic set consisting of 31 image frames and two static data sets with one frame each. In order to implement a pointwise hypoxia analysis, it was necessary to match these three data sets. The corresponding rigid body transformation matrix was calculated by applying a mutual information algorithm (Viola and Wells 1997). This matching procedure reached an accuracy $\leqslant 2$ mm in the region of the tumour and allowed us to determine a TAC for each voxel.

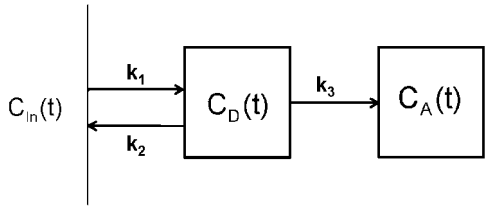

Figure 1. Compartmental model consisting of a diffusive and an accumulative compartment. The input function $C_{\mathrm{In}}(t)$ comprises the tracer concentration in the blood and in the interstitial space close to the vessels.

2.2. Kinetic model

Histochemical studies (Ljungkvist *et al* 2002, Janssen *et al* 2002, 2004) found increasing staining intensities for pimonidazole in addition to a larger quantity of cells accumulating the tracer molecules far from blood vessels. Typical distances for increased pimonidazole staining are 100–200 μm. Since there exists no active transport mechanism for pimonidazole or Fmiso in the interstitium, the transport of the tracer molecules is purely diffusive (Jain 1987). Considering the molecular weight of Fmiso and the distances the molecules have to travel from the vessel to the hypoxic cell (Jain 1987), the diffusion time will be high compared to other tracers with active transport mechanisms and shorter diffusion distances (such as e.g. FDG (Laubenbacher and Schwaiger *et al* 2000)). The time the marker needs to reach the hypoxic tissue area far from the blood vessel will be in the order of 100–1000 s, as motivated in the following.

Although the diffusive transport depends crucially on the tissue geometry, blood vessel permeability and the interstitial flow and pressure situation, which is obviously unknown, the bulk diffusion equation (without spatial dependences) for a net flow from a point A to a point B reads schematically:

$$\partial_t C_B = \frac{D}{l^2}(C_A(t) - C_B). \tag{1}$$

Here D is the diffusion constant, l the distance between points A and B and $C_A(t)$ is assumed to be unaffected by the efflux (infinite supply). The linearity of the diffusion equation allows us to associate spatially separated sub-volumes with compartments and an approximate linear reaction rate equation. For a compartmental model, the consequence of this diffusion delay will be a translation of the spatial separation of blood pool and tracer trapping into a temporal separation (Hicks *et al* 1997). With D typically in the order of 10^{-6} cm^2 s^{-1}, and $l \simeq 0.01$ cm it follows that $k \simeq 10^{-2}$ s^{-1}, i.e. typical time scales are >100 s.

Regarding the design of a kinetic model, it is assumed that for all practical purposes a general two compartment model (see figure 1) will be sufficient to describe the dynamic Fmiso data[4]. The model can be motivated by the heuristics that there are essentially three distinguishable components of the TACs. One, showing rapid concentration changes due to perfusion and fast diffusion into the interstitial space close to the vessels, represented by the input function. Another, characterized by slow concentration changes due to long diffusion times to and from the large inter-vessel spaces of irregular tumours. And a third, describing the irreversible binding of the tracer. In the following, the compartment describing the freely diffusive tracer molecules will be referred to as *diffusive* compartment. The *accumulative*

[4] This is a consequence of the integration of the manifold of various TACs of all the particular sub-volumes in a PET voxel. If tumours were more homogeneous or the spatial resolution of the scanner better, a chain of compartment pairs, stratified according to their diffusion time, might be a more appropriate model.

compartment is linked to the diffusive compartment by a kinetic rate constant that depends on the partial oxygen pressure.

In contrast to classic compartmental models, the compartments in this model are spatially separated or overlap only partially (the accumulative compartment corresponds only to those sub-volumes described by the diffusive compartment which are hypoxic) and the volumes of the different compartments are not identical. In addition, some of the kinetic constants of this model are not parameters of a chemical reaction, but reflect purely diffusive transport.

The diffusive compartment is linked to the input function by diffusion rate constants k_1 and k_2. The accumulative part is only coupled to the diffusive one with the rate constant k_3. It is assumed that the diffusion of unbound reduced Fmiso cannot be discerned on the time scales of the experiment. This kinetic model is described by the following system of differential equations:

$$\frac{\partial}{\partial t}C_D(t) = k_1 C_{\mathrm{In}}(t) - (k_2 + k_3)C_D(t) \tag{2}$$

$$\frac{\partial}{\partial t}C_A(t) = k_3 C_D(t). \tag{3}$$

$C_D(t)$ and $C_A(t)$ are the basis functions for the diffusive and the accumulative compartments respectively. They are determined by

$$\begin{aligned} C_D(t) &= \mathrm{e}^{-(k_2+k_3)t} \otimes k_1 C_{\mathrm{In}}(t) \\ &= k_1 \int_0^t \mathrm{e}^{-(k_2+k_3)(t-\tau)} C_{\mathrm{In}}(\tau)\,\mathrm{d}\tau \end{aligned} \tag{4}$$

and

$$\begin{aligned} C_A(t) &= k_3 \otimes C_D(t) \\ &= \frac{k_1 k_3}{k_2 + k_3} \int_0^t (1 - \mathrm{e}^{-(k_2+k_3)(t-\tau)}) C_{\mathrm{In}}(\tau)\,\mathrm{d}\tau, \end{aligned} \tag{5}$$

where the k_i are the respective rate constants and $\otimes$ denotes the convolution product. The total measured PET signal $S(t)$ is given by a linear combination of the basis functions (equations (4) and (5)) and the input function $C_{\mathrm{In}}(t)$:

$$\begin{aligned} S(t) &= w_0 C_{\mathrm{In}}(t) + w_D C_D(t) + w_A C_A(t) \\ &= w_0 C_{\mathrm{In}}(t) + w_D k_1 \int_0^t \mathrm{e}^{-(k_2+k_3)(t-\tau)} C_{\mathrm{In}}(\tau)\,\mathrm{d}\tau \\ &\quad + w_A \frac{k_1 k_3}{k_2 + k_3} \int_0^t (1 - \mathrm{e}^{-(k_2+k_3)(t-\tau)}) C_{\mathrm{In}}(\tau)\,\mathrm{d}\tau. \end{aligned} \tag{6}$$

Here w_D and w_A are the relative weights of the compartments. They represent the relative contribution of each compartment to the total signal. The weight parameters correspond, if properly normalized, to the volume fraction that is occupied by these compartments. Therefore, w_A could also be interpreted as the mean concentration of hypoxic cells in this voxel.

In the complete expression for the total signal $S(t)$ (equation (6)), the rate constant k_1 turns out to be only a multiplicative factor to the weight parameters w_D and w_A. It can therefore be set constant without loss of generality. Variations of this parameter are absorbed in $\tilde{w}_D = w_D k_1$ and $\tilde{w}_A$. Additionally, the rate constant k_2 can be absorbed by substituting $\tilde{k}_3 = k_2 + k_3$ and $\tilde{w}_A = w_A k_1 k_3 / \tilde{k}_3$. The final equation for the PET signal reads

$$S(t) = w_0 C_{\mathrm{In}}(t) + \tilde{w}_D \int_0^t \mathrm{e}^{-\tilde{k}_3(t-\tau)} C_{\mathrm{In}}(\tau)\,\mathrm{d}\tau + \tilde{w}_A \int_0^t (1 - \mathrm{e}^{-\tilde{k}_3(t-\tau)}) C_{\mathrm{In}}(\tau)\,\mathrm{d}\tau. \tag{7}$$

The remaining kinetic model has four open parameters, the weight parameters w_0, $\tilde{w}_D$ and $\tilde{w}_A$ in addition to the modified accumulation rate constant $\tilde{k}_3$.

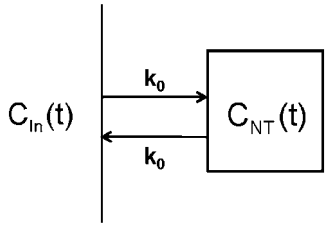

Figure 2. Reference tissue compartment.

2.3. Input function

For head and neck cases, it is difficult to obtain the blood input function directly from the images. Therefore, we propose the use of a reference tissue model. Normal tissues can be described by a kinetic model consisting of the blood concentration $C_{\mathrm{In}}(t)$ and a tightly coupled diffusive compartment, see figure 2. The tracer concentration in the cell layers around a blood vessel (i.e. the diffusive compartment of the normal tissue model) is denoted with $C_{\mathrm{NT}}(t)$. Therefore, the input function may be extracted from typical normal tissue voxels.

During the first minutes after injection, the image signal is governed by diffusion from well perfused capillaries into the interstitial space. This will occur in a similar fashion in both normal tissue and tumour tissue, although the deficient vasculature in tumours may offer less resistance. In this case, k_1 and k_2 of the tumour would be greater than in the reference tissue, but this does not affect the input function, which should be the same as long as the tracer transition from the vessel into the interstitial space is permeability limited and not flow limited. Apart from this difference in kinetic parameters, well perfused tumour areas and normal tissues should behave similarly during the first minutes after injection. This assumption is corroborated by immunohistochemical investigations (Ljungkvist *et al* 2002, Janssen *et al* 2002, 2004) that showed that cells situated in the neighbourhood of a blood vessel under well oxygenated conditions exist in both hypoxic and non-hypoxic tumours.

However, these investigations also show badly perfused vessels. Also, temporary stasis has been described in tumours (Denekamp and Daşu 1999). This means, that the well perfused vasculature which becomes visible in the first minutes after injection may not be the entire vasculature available for tracer transport by flow during the course of the investigation. Frequently, the distinction between chronic and acute hypoxia is made. The effect of fluctuations in the perfusion of a voxel on the TAC depends on the time scale of these fluctuations relative to the diffusion time scale, and the partial volume of the voxel affected by them. In our model, this is approximately taken into account by a spatially dependent input function as follows.

We assume, that the input function to the tumour kinetic model $C_{\mathrm{In}}(t)$ can be derived from the signal of a reference tissue $S_{\mathrm{NT}}(t) = AC_{\mathrm{In}}(t) + BC_{\mathrm{NT}}(t)$. We assume further that the blood concentration after a certain time after injection is a sum of two exponentials:

$$C_{\mathrm{In}} = \mathrm{e}^{-k_0 t} + r\,\mathrm{e}^{-k_K t}. \tag{8}$$

The first term $\mathrm{e}^{-k_0 t}$ describes the dispersion of the tracer in the whole body blood volume, whereas the second exponential represents the kidney clearance of the tracer. The rapid rise of tracer concentration in the blood pool observed in the very early frames is not taken into account by this input function. Therefore, the first frames (typically 4-5) have to be ignored for data analysis.

The concentration in the extravascular normal tissue space obtains from a convolution

$$C_{\mathrm{NT}}(t) = C_{\mathrm{In}}(t) \otimes \mathrm{e}^{-k_0 t}. \tag{9}$$

Here, we assume that the diffusion rate constant k_0 equals the mean rate of tracer flux into the extravascular volume, averaged over the whole body.

The signal measured in a reference tissue voxel $S_{\mathrm{NT}}(t)$ will be of the form

$$S_{\mathrm{NT}}(t) = A(\mathrm{e}^{-k_0 t} + r\,\mathrm{e}^{-k_K t}) + BC_{\mathrm{NT}}(t). \tag{10}$$

The parameters k_0 and k_K are determined by fitting this expression (equation (10)) to a set of TACs from a reference tissue in close proximity of the tumour. For the input function of a tumour voxel, these parameters are kept constant while r remains floating. This allows us to adapt the ratio between the fast and the slow component of the input function to the local properties of the tumour vasculature and perfusion, and to some extent to their temporal variability. The number of parameters in the fit of the voxel-by-voxel TACs to the compartment model (equation (7)) thereby increases to five.

2.4. Data evaluation

In order to evaluate the time-activity data with the presented kinetic model, a least-squares fit was performed to adjust the analytical function $S(t)$ (6) to the patient TACs. For this, a Levenberg–Marquardt algorithm was used (Press *et al* 1992).

The data points were included into the proximity function with errors corresponding to Poissonian noise. In analogy to Casciari *et al* (1995), standard deviations σ_i were calculated as scaled Poissonian noise, depending on local count rate $Y_i(t)$ and acquisition time T_i for the respective frame.

Additional uncertainties may occur due to image coregistration errors. As only the late data sets (2–4 h p.i.) undergo a matching procedure, additional errors have only to be taken into account for the late data points. The magnitude of the individual error associated with each image voxel depends strongly on the image gradient in the considered region. Hence, the error due to an eventual mismatch ΔY_{MM} can be estimated by

$$\Delta Y_{MM} = \Delta x \left(\sum_{i=1}^{n} \frac{(Y - Y_i)^2}{n x_i} \right)^{1/2}, \tag{11}$$

where Y_i are the count rates of the n neighbour voxels, x_i is the distance to the respective neighbour voxel and Δx represents the average coregistration error, which is assumed to be approximately 2 mm in our case. The total error associated with data points 2, 3 and 4 h p.i. is determined by $\Delta Y_i^{\mathrm{tot}} = \sigma_i Y_i + \Delta Y_{MM}$.

The variability of the model parameters due to the estimated data errors is then determined by the covariance matrix associated with the least-squares fit (Press *et al* 1992). The diagonal matrix elements represent estimates of the respective parameter variances.

In addition, the continuous automatic tracer injection during the first 10 s after the start of the acquisition is not taken into account by the model. To avoid problems, the very steep and slightly oscillating component dominating all data curves during the first 60 s was omitted.

In order to visualize the voxel-by-voxel results of the compartmental data analysis, *hypoxia maps* were generated by colouring each voxel of the tumour volume according to the tracer uptake at infinite times S_∞:

$$S_\infty = \lim_{t \to \infty} S(t) = \alpha \tilde{w}_A, \tag{12}$$

where $\alpha = Ak_1(1/k_0 + r/k_K)$. The parameter plots show areas presenting high levels of tracer uptake which correlates to the mean density of viable hypoxic cells in the respective voxel.

Prompted by the immunohistochemical experiments which imply that vascular density and hypoxia are independent parameters and which report a great variability of vascular geometries, a second visualization tool was devised. A *scatter plot* is generated by plotting the value of $w_A k_3$, describing the concentration of hypoxic cells weighted with the mean degree of hypoxia for each voxel on the abscissa against w_0 (the grade of perfusion) on the ordinate. Characteristic patterns in the scatter plots will allow us to distinguish between tumour areas according to vascular density and concentration of hypoxia.

3. Results

The TACs observed in a group of 16 examined patients showed great variability. In figure 3, four examples of characteristic shapes of the acquired time-activity data are displayed.

In well perfused regions[5], the shapes of the curves have a very pronounced tracer influx and distribution during the first few minutes after tracer injection followed by an exponential washout (see figure 3(a)). These tumour areas are characterized by a high density of vessels and a good blood supply. The majority of cells should be well oxygenated because no tracer retention can be seen.

In figure 3(b), a very similar behaviour can be observed during the first 30 min, followed by a clear retention. This shows that a large number of viable hypoxic cells are present, which co-exist with a very well perfused cell population. This is the classical picture of diffusion limited hypoxia, where oxygen consumption outweighs supply.

More serious forms of hypoxia result from a deficient vasculature and chaotic blood flow. However, this may also result in a decrease of viable hypoxic cells as necrotic cores may form in which no tracer retention occurs. In terms of the TAC, the perfusion peak should become smaller, and retention less pronounced until finally a horizontal curve type results, see figures 3(c) and (d). In voxels with a significant concentration of necrosis, the purely diffusive contribution to the signal as represented by w_D and r should go up. The tracer enters these tissue regions very slowly due to the low density of blood vessels. Accumulation of tracer can be observed in the order of several hours after injection (see figure 3(d)). Because of the small fraction of viable hypoxic cells, the total uptake is low.

Figure 4 shows the analytical curves $S(t)$ determined by the kinetic analysis for the data TACs presented in figure 3. The corresponding parameter values are summarized in table 2, whereas table 3 shows the corresponding parameter value uncertainties.

In summary, figures 3 (a)–(d) represent the TACs in tumour regions with increasingly deficient vasculature. The tracer influx peak at short timepoints after injection decreases as the blood supply gets worse due to the more and more chaotic vasculature. At the same time, while the number of viable hypoxic cells decreases (w_A), the degree of hypoxia increases (k_3). The kinetic analysis showed that the resulting parameter values might reveal information about the structural architecture of the tissue sample. Curve types representing putatively well perfused and only slightly hypoxic tumours (such as figure 4(a)) are described by a relatively high weight parameter w_0 in addition to a small value for the product $\tilde{w}_A \tilde{k}_3$ for the hypoxic compartment. Also for the diffusion limited hypoxia type (figure 4(b)) a large w_0 is found, but in this case the value of $\tilde{w}_A$ and thus S_∞ is also high.

In contrast, there exist tumour areas where very small parameters w_0 are necessary to describe the time-activity course of the data adequately. This behaviour is mainly observed

[5] Good perfusion/high vascular density is supposed in regions where the dynamic TAC presents a fast tracer influx after injection ($\approx$ 30–40 s).

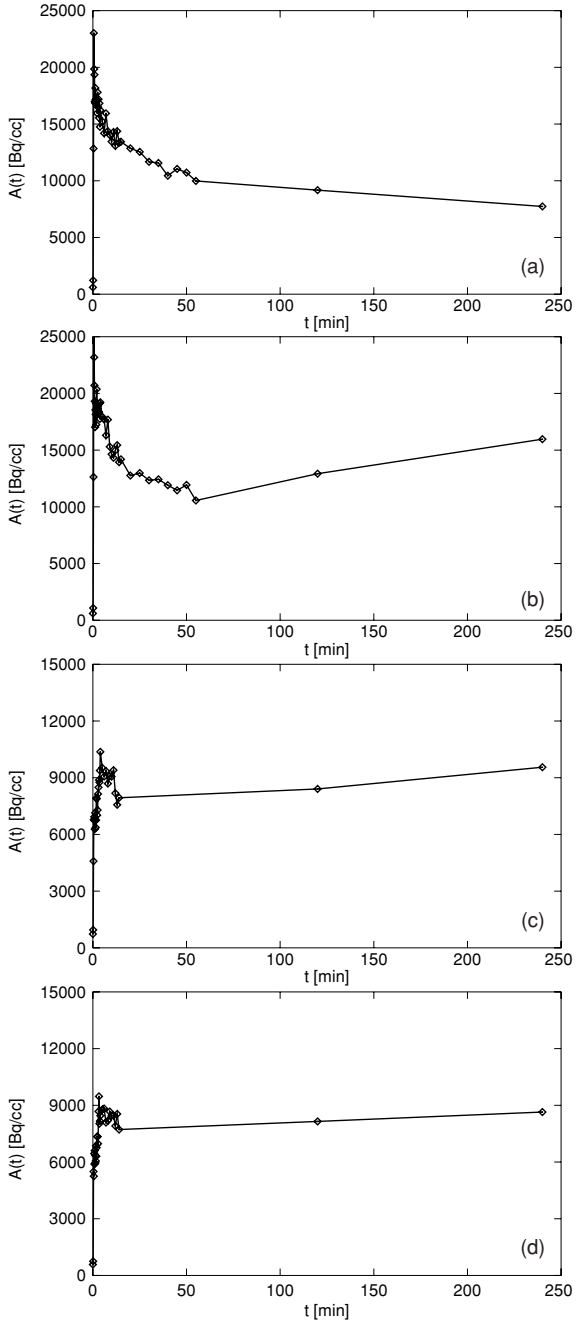

Figure 3. Different characteristic time-activity data curves corresponding to tumour areas with increasingly deficient vasculature. (a) Well perfused tumor area. (b) Tissue area with diffusion limited hypoxia. (c) Diffusion limited and structural hypoxia. (d) Hypoxic/necrotic area.

for curves that putatively represent severely hypoxic or necrotic tissues (such as figures 4(c) and (d)). Hence, $\tilde{w}_A\tilde{k}_3$ turns out to take relatively high values.

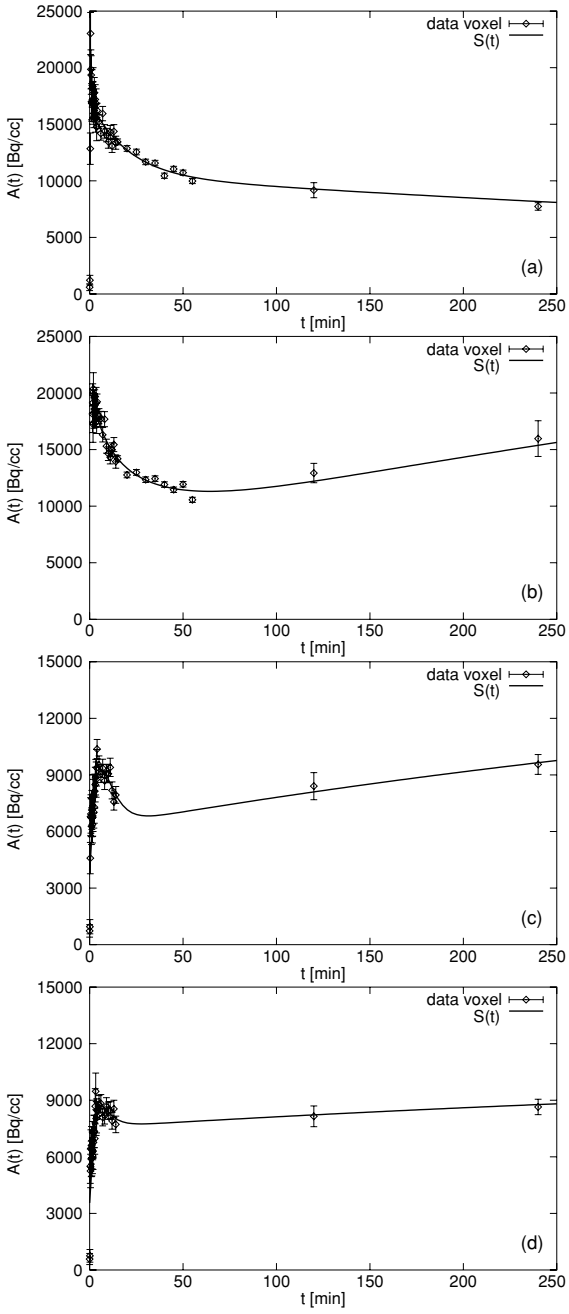

Figure 4. Resulting analytical time-activity curves corresponding to data curves (a)–(d) of figure 3.

In the following, the kinetic data analysis will be shown in more detail exemplarily for two of the 16 examined patients. Nevertheless, a kinetic analysis was performed for each data set, but they cannot all be shown in the context of this paper.

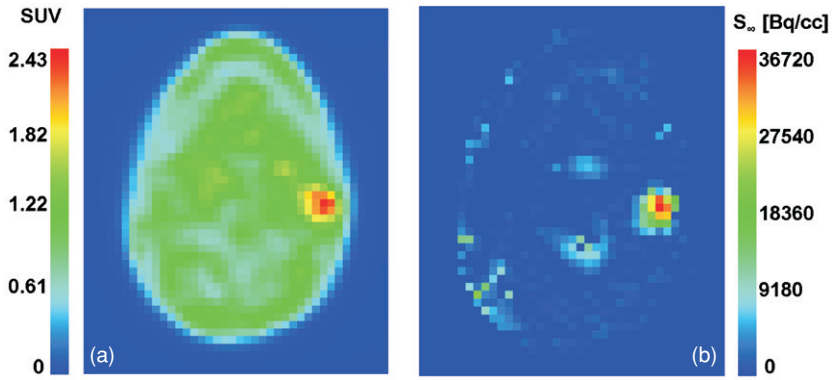

Figure 5. Tumour region of a head-and-neck patient: (a) SUV distribution 2 h p.i. for a whole PET slice, (b) parametric plot: S_∞ for each voxel.

Table 2. Resulting parameter values for curves (a)–(d), figure 4.

	Putative structure types	w_0	r	$\tilde{w}_D$ (min^{-1})	$\tilde{w}_A$ (min^{-1})	$\tilde{k}_3$ (min^{-1})
(a)	Low hypoxia/ well perfused	1.06	0.29	0.09	0.00	–
(b)	Diffusion limited hypoxia	1.50	0.10	0.13	0.31	0.03
(c)	Diffusion limited and structural hypoxia	0.32	0.45	0.28	0.08	0.21
(d)	Strongly hypoxic/ necrotic	0.16	1.67	0.14	0.01	0.36

Table 3. Errors of model parameters due to image noise and coregistration uncertainties associated with curves (a)–(d), figure 4.

	Δw_0	Δr	$\Delta\tilde{w}_D$ (min^{-1})	$\Delta\tilde{w}_A$ (min^{-1})	$\Delta\tilde{k}_3$ (min^{-1})
(a)	0.17	0.17	0.02	0.00	–
(b)	0.18	0.11	0.02	0.11	0.02
(c)	0.16	0.39	0.06	0.08	0.11
(d)	0.18	1.86	0.07	0.01	0.25

Figures 5(b) and 7(b) show S_∞ parameter plots of two different patients. Both hypoxia maps are displayed in comparison to the corresponding SUV distributions at 2 h p.i. (figures 5(a) and 7(a)).

Figure 5(b) represents a first example of a parametric plot for a head-and-neck patient. The region characterized by an increased SUV 2 h p.i. is also highlighted in the parametric plot. A typical TAC of this region is plotted in figure 6. The curve shows a relatively high influx peak as well as a positive slope for long times after injection.

In the second case, displayed in figure 7, the SUV image 2 h after injection indicates two distinct areas where the tracer seems to be accumulated (figure 7(a)). However, the parametric plot for the indicated region of interest only highlights one of these two regions (figure 7(b)). This phenomenon is due to a different overall shape of the curves in the respective tumour

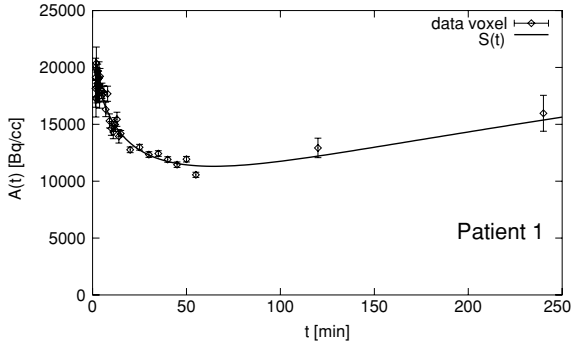

Figure 6. Typical TAC of the tracer accumulating region in figure 5.

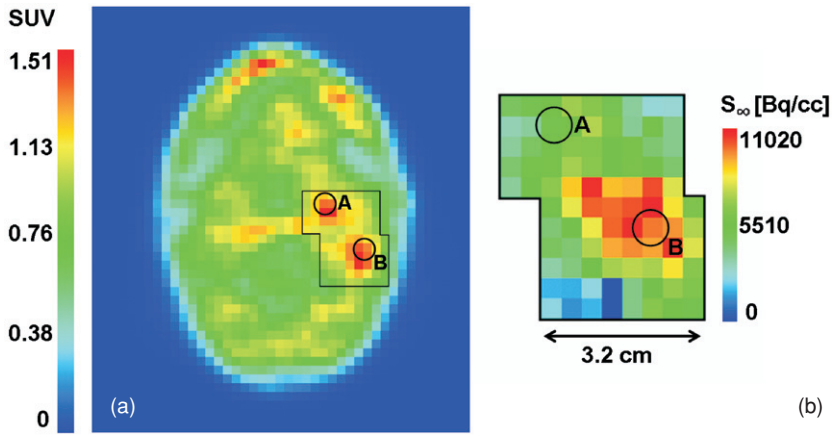

Figure 7. (a) SUV distribution 2 h p.i., (b) parametric plot for the marked tumour region: S_∞ for each voxel.

voxels and may be caused by different architectures of the tumour vascularization leading to different diffusion times for the tracer.

Voxels A and B were chosen as representatives for these two areas. The analytical curves $S(t)$ as well as the corresponding measured data points are displayed in figure 8. The plotted TACs present an interesting behaviour: even though the two curves have nearly the same activity level 120 min after tracer injection, the shape of the curves is completely different. While the TAC for voxel A shows a very high tracer influx peak followed by a continuous washout, voxel B is characterized by a steady accumulation of tracer 30 to 240 min p.i. in addition to a much lower influx peak at the beginning. Hence, the impression that the static image 2 h after injection presented the same level of tracer accumulation was due to the fact that the intercept point of two absolutely different curves was situated coincidentally at the time of image acquisition. Therefore, it does not seem reliable to identify hypoxia only on the basis of a static image 2 h p.i. which obviously bears high risks of incorrect interpretation.

An additional tool to analyse hypoxia and perfusion characteristics of a tumour is provided by the $(w_0, w_A k_3)$ scatter plot. It allows us to determine the dominating type of structural architecture in the tumour volume. Patients displaying large values for w_0 for most of the voxels have putatively well perfused tumours. Whereas, if the tumour contains hypoxic cores,

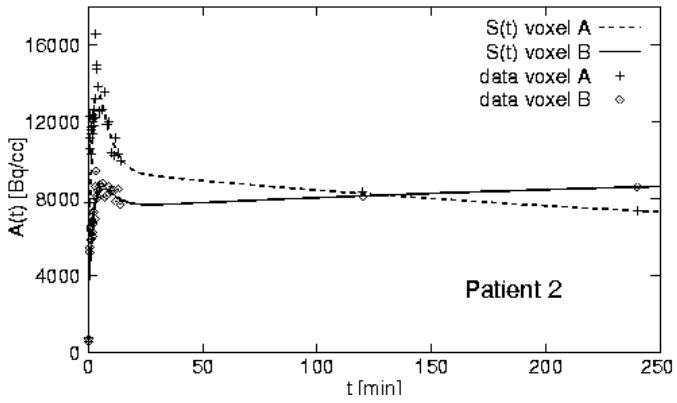

Figure 8. Comparison of the overall curve shapes of voxels *A* and *B*, figure 7.

the corresponding $w_A k_3$-parameters will have high values and will therefore be situated in the lower right area of the scatter plot. Hence, the presented scatter plot provides a medium to classify tumours according to different characteristic structure types.

For the two patients exemplarily shown above (figures 3 and 5), scatter plots have been generated. The analysis of the scatter plot for patient 1 (figure 9(a)) reveals that a large fraction of the tumour volume has relatively high levels of perfusion together with rather small concentrations of hypoxia. In contrast, patient 2 (figure 9(b)) shows for the whole tumour very low perfusion values, and at the same time high concentrations of hypoxia are observed.

4. Discussion

The presented investigation showed that the overall shapes of the TACs contain essential information about hypoxic tumour areas. Particularly the behaviour of the curves at long time scales is important. Hence, a criterion based on a single time point threshold is not sufficient to perform a reliable hypoxia analysis. The use of a static criterion to identify hypoxia in Fmiso PET scans might have been a reason why Bentzen *et al* (2003) could not find a clear correlation between PET and Eppendorf electrode measurements.

Curve features such as the position of the minimum in the TACs between 20 and 60 min hint at the characteristics of the underlying processes which occur on corresponding time scales. This property is understandable by the immunohistochemical investigations with pimonidazole (Ljungkvist *et al* 2002, Janssen *et al* 2002, 2004) that found that long diffusion distances had to be travelled by the tracer before reaching hypoxic cells. The signature of the characteristic diffusion times in the tumour tissue is the position of the minimum in the curves.

Different tumour structure types may be associated with different characteristic shapes of the TACs. Putatively well perfused and regularly vascularized tumours show curves with a high influx peak and exponential washout, whereas a good perfusion together with diffusion limited hypoxia should result in a positive slope at long time scales, leading to high tracer uptake values S_∞. The curves probably corresponding to severely hypoxic or necrotic tissues present no influx peak and a horizontal time trend remaining at relatively low SUV levels. These results can be understood by comparison with the microscopic tissue sections presented by other investigators (Ljungkvist *et al* 2002), where different characteristic hypoxia patterns (‘patchy’ and ‘ribbon-like’) were found.

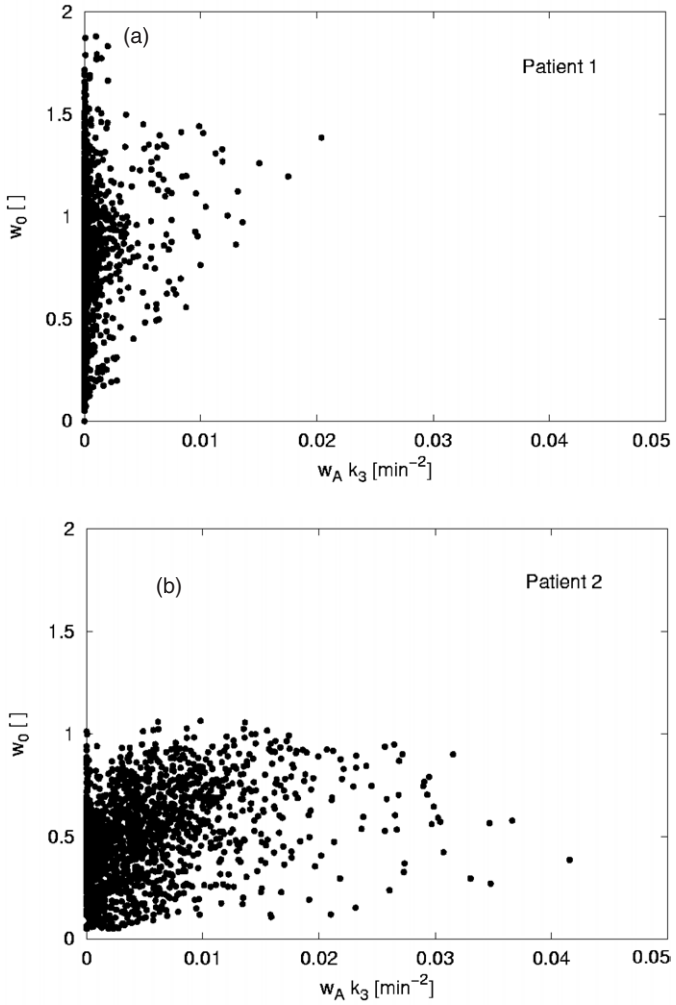

Figure 9. Scatter plots for two patients. (a) Patient 1 (cf figure 3) shows a quite well perfused and only moderately hypoxic tumour. (b) Patient 2 (cf figure 5) in contrast has a badly perfused and severely hypoxic tumour.

A particular problem with severely hypoxic areas is the presence of necrosis. Since Fmiso uptake occurs only in viable hypoxic cells, a low uptake may be caused by a small fraction of surviving cells. This is compounded by the finding that the binding rate constant is similar to the rate of renal clearance, so that the net effect can be a constant signal. In contrast, tumour areas that present very high levels of tracer uptake consist of many viable, hypoxic cells by necessity. These may not be the most resistant tumours and they might constitute a group that highly benefits from individually adapted therapies. A classification of the patients according to these criteria can be performed on the basis of the introduced perfusion-hypoxia scatter plots.

The presented model involves slow diffusion rates of the tracer in the interstitium, caused by long diffusion distances in the tumour tissue. It also respects the inherent heterogeneity of tumour tissues, where well perfused and hypoxic sub-volumes may coexist in the same

PET voxel. These facts were not considered by previous models (Casciari *et al* 1995), which explicitly treated homogeneous tumour tissues and were more appropriate to normal tissues made hypoxic under experimental conditions.

The heterogeneity of the tumour structure requires that all compartment weights remain floating in the fits to accommodate partial volume effects by virtue of the linearity of the differential equation and the input function becomes spatially variable. Due to the particular choice of the input function and the assumption of physical transport into the diffusive compartment which ensures $k_{1,\mathrm{in}} = k_{1,\mathrm{out}}$, the total number of fit parameters is five. This reduces the variability and co-variance of the fits. The experimentally established need for a spatially variable input function poses an obstacle to the use of graphical TAC analysis.

5. Conclusion

The investigated method allows us to identify and quantify hypoxia in human head-and-neck tumours based on dynamic Fmiso PET scans better than SUV alone. Hypoxia is essentially a consequence of irregular vascularization, and this needs to be taken into account when time-activity curves of hypoxia PET tracers are interpreted. Perfusion and the degree of hypoxia seem to be independent properties of a tumour.

Acknowledgments

We would like to thank Professor H-J Machulla (Department of Radiopharmacy, University Hospital Tübingen) and his team for [^{18}F]-Fmiso tracer production. We also thank Professor A van der Kogel and Dr A Ljungkvist (University Medical Center Nijmegen, The Netherlands) and Professor A Begg (The Netherlands Cancer Institute, Amsterdam, The Netherlands) for helpful discussions.

This project was financially supported by the *f*ortüne program of the University Hospital Tübingen, grant no. 1161-0-0 and by the German Research Foundation (DFG), grant no. AL 877/1-1.

References

Alber M, Paulsen F, Eschmann S M and Machulla H-J 2003 On biologically conformal boost dose optimization *Phys. Med. Biol.* **48** N31–5

Bentzen L, Keiding S, Nordsmark M, Falborg L, Hansen S B, Keller J, Nielsen O S and Overgaard J 2003 Tumour oxygenation assessed by ^{18}F-fluoromisonidazole PET and polarographic needle electrodes in human soft tissue tumours *Radiother. Oncol.* **67** 339–44

Casciari J J, Graham M M and Rasey J S 1995 A modeling approach for quantifying tumor hypoxia with [F-18]fluoromisonidazole PET time-activity data *Med. Phys.* **22** 1127–39

Chao K S C, Bosch W R, Mutic S, Lewis J S, Dehdashti F, Mintun J F, Dempsey J F, Perez C A, Purdy J A and Welch M J 2001 A novel approach to overcome hypoxic tumor resistance: cu-aTSM-guided intensity-modulated radiation therapy *Int. J. Radiat. Oncol. Biol. Phys.* **49** 1171–82

Denekamp J and Daşu A 1999 Inducible repair and the two forms of tumour hypoxia—time for a paradigm shift *Acta Oncol.* **38** 903–18

Hicks K O, Ohms S J, van Zijl P L, Denny W A, Hunter P J and Wilson W R 1997 An experimental and mathematical model for the extravascular transport of a DNA intercalator in tumours *Br. J. Cancer* **76** 894–903

Jain R K 1987 Transport of molecules in the tumor interstitium: a review *Cancer Res.* **47** 3039–51

Janssen H L K *et al* 2002 HIF-1A, pimonidazole, and iododeoxyuridine to estimate hypoxia and perfusion in human head-and-neck tumors *Int. J. Radiat. Oncol. Biol. Phys.* **54** 1537–49

Janssen H L K, Hoebers F J, Sprong D, Goethals L, Williams K J, Stratford I J, Haustermans K M, Balm A J and Begg A C 2004 Differentiation-associated staining with anti-pimonidazole antibodies in head and neck tumors *Radiother. Oncol.* **70** 91–7

Kaanders J H A M, Bussink J and van der Kogel A J 2002 ARCON: a novel biology-based approach in radiotherapy *Lancet Oncol.* **3** 728–37

Koh W-J, Rasey J S, Evans M L, Grierson J R, Lewellen T K, Graham M M, Krohn K A and Griffin T W 1992 Imaging of hypoxia in human tumors with [F-18]fluoromisonidazole *Int. J. Radiat. Oncol. Biol. Phys.* **22** 199–212

Laubenbacher C and Schwaiger M 2000 The potential role of positron emission tomography in investigation of microenvironment *Blood Perfusion and Microenvironment of Human Tumors* ed M Molls and P Vaupel (Berlin: Springer)

Lehtiö K, Eskola O, Viljanen T, Oikonen V, Grönroos T, Sillanmäki L, Grénman R and Minn H 2004 Imaging perfusion and hypoxia with PET to predict radiotherapy response in head-and-neck cancer *Int. J. Radiat. Oncol. Biol. Phys.* **59** 971-82

Ljungkvist A S E, Bussink J, Rijken P F J W, Kaanders J H A M, van der Kogel A J and Denekamp J 2002 Vascular architecture, hypoxia, and proliferation in first-generation xenografts of human head-and-neck squamous cell carcinomas *Int. J. Radiat. Oncol. Biol. Phys.* **54** 215–28

Machulla H-J 1999 *Imaging of Hypoxia* (Dordrecht: Kluwer)

Nordsmark M and Overgaard J 2000 A confirmatory prognostic study on oxygenation status and loco-regional control in advanced head and neck squamous cell carcinoma treated by radiation therapy *Radiother. Oncol.* **57** 39–43

Nordsmark M, Overgaard M and Overgaard J 1996 Pretreatment oxygenation predicts radiation response in advanced squamous cell carcinoma of the head and neck *Radiother. Oncol.* **41** 31–9

Press W H, Teukolsky S A, Vetterling W T and Flannery B P 1992 *Numerical Recipes in C: The Art of Scientific Computing* 2nd edn (Cambridge: Cambridge University Press)

Rasey J S, Koh W-J, Evans M L, Peterson L M, Lewellen T K, Graham M M and Krohn K A 1996 Quantifying regional hypoxia in human tumors with positron emission tomography of [^{1}8F]fluoromisonidazole: a pretherapy study of 37 patients *Int. J. Radiat. Oncol. Biol. Phys.* **36** 417–28

Viola P and Wells W M 1997 Alignment by maximization of mutual information *Int. J. Comput. Vis.* **24** 137–54

Appendix B

Kinetic analysis of dynamic ^{18}F-fluoromisonidazole PET correlates with radiation treatment outcome in head-and-neck cancer

published in
BMC Cancer 2005; **5**: 152

BMC Cancer

BioMed Central

Research article

Open Access

Kinetic analysis of dynamic ^{18}F-fluoromisonidazole PET correlates with radiation treatment outcome in head-and-neck cancer

Daniela Thorwarth*[1], Susanne-Martina Eschmann[2], Jutta Scheiderbauer[3], Frank Paulsen[3] and Markus Alber[1]

Address: [1]Section for Biomedical Physics, Clinic for Radiation Oncology, University Hospital Tübingen, Germany, [2]Department of Nuclear Medicine, Radiological Clinic, University Hospital Tübingen, Germany and [3]Department of Radiation Therapy, Clinic for Radiation Oncology, University Hospital Tübingen, Germany

Email: Daniela Thorwarth* - daniela.thorwarth@med.uni-tuebingen.de; Susanne-Martina Eschmann - susanne-martina.eschmann@med.uni-tuebingen.de; Jutta Scheiderbauer - jutta.scheiderbauer@med.uni-tuebingen.de; Frank Paulsen - frank.paulsen@med.uni-tuebingen.de; Markus Alber - markus.alber@med.uni-tuebingen.de

* Corresponding author

Published: 01 December 2005

BMC Cancer 2005, **5**:152 doi:10.1186/1471-2407-5-152

Received: 11 July 2005
Accepted: 01 December 2005

This article is available from: http://www.biomedcentral.com/1471-2407/5/152

Abstract

Background: Hypoxia compromises local control in patients with head-and-neck cancer (HNC). In order to determine the value of [^{18}F]-fluoromisonidazole (Fmiso) with regard to tumor hypoxia, a patient study with dynamic Fmiso PET was performed. For a better understanding of tracer uptake and distribution, a kinetic model was developed to analyze dynamic Fmiso PET data.

Methods: For 15 HNC patients, dynamic Fmiso PET examinations were performed prior to radiotherapy (RT) treatment. The data was analyzed using a two compartment model, which allows the determination of characteristic hypoxia and perfusion values. For different parameters, such as patient age, tumor size and standardized uptake value, the correlation to treatment outcome was tested using the Wilcoxon-Mann-Whitney *U*-test. Statistical tests were also performed for hypoxia and perfusion parameters determined by the kinetic model and for two different metrics based on these parameters.

Results: The kinetic Fmiso analysis extracts local hypoxia and perfusion characteristics of a tumor tissue. These parameters are independent quantities. In this study, different types of characteristic hypoxia-perfusion patterns in tumors could be identified.

The clinical verification of the results, obtained on the basis of the kinetic analysis, showed a high correlation of hypoxia-perfusion patterns and RT treatment outcome ($p = 0.001$) for this initial patient group.

Conclusion: The presented study established, that Fmiso PET scans may benefit from dynamic acquisition and analysis by a kinetic model. The pattern of distribution of perfusion and hypoxia in the tissue is correlated to local control in HNC.

Background

Local control remains a great challenge in head-and-neck cancer (HNC) treatment. Even with an optimal combination of radio- and chemotherapy, local recurrences are

observed in up to 50% of the treated patients [1,2]. Up to now, no reliable parameter could be established that would account for this high rate of local failures.

Tumor hypoxia has been known to be associated with poor radiation response for several decades. Recent publications suggested that hypoxia in tumors had a direct influence on treatment success [3,4] by a variety of mechanisms [5,6]. A prognostic impact of tumor hypoxia for therapy outcome in head and neck cancer (HNC) has been shown by different investigators [7-9]. Hypoxia has also been related to lower survival probability and higher risk of recurrence in patients with cervix cancer [4,10]. In these studies, hypoxia was assessed invasively by polarographic Eppendorf electrodes.

Positron emission tomography (PET) with appropriate radiotracers enables non-invasive assessment of the presence and distribution of hypoxia. The radiotracers in frequent use are ^{18}F-fluoromisonidazole (Fmiso) [11-13] and chemically similar markers such as ^{18}F-fluoroazomycin (Faza) [14] or, with a different binding mechanism, ^{60}Cu-ATSM [15]. Some investigations report an unclear correlation between Eppendorf measurements and standardized uptake values (SUV) determined on the basis of Fmiso PET [16]; even though a tumor-to-blood ratio of 1.4 was defined as diagnostic of hypoxia [11]. Thus, the predictive value of Fmiso SUV even several hours after tracer injection remains unclear. Based on their chemical structure, nitroimidazoles are trapped inside hypoxic cells. This feature makes these agents ideal markers for hypoxia in in-vitro cell systems [17]. However, transforming this into larger scale biological systems is problematic and the interpretation of Fmiso PET images remains unclear. An advantage of PET compared to Eppendorf measurements is the ability to display spatial distributions, which is necessary for the integration of hypoxia information into adaptive treatments such as hypoxia dose painting [18-20]. For immunohistochemical investigations, the marker pimonidazole is well established [21-23] to stain hypoxic tumor cells. As the functional binding mechanisms of pimonidazole and Fmiso are similar, Fmiso should be specific to hypoxia to a similar degree. However, the immunohistochemical staining patterns are very complex and reveal a highly heterogeneous distribution of perfused blood vessels and hypoxic patches, sometimes interspersed with necrotic islands, all occurring on a microscopic scale. This may hint as to why Fmiso tracer uptake alone is not a reliable diagnostic quantity, and indicates the requirement of an analysis of dynamic Fmiso PET which takes into account the structural complexity of hypoxic tumor tissues. The study described here was designed to develop a kinetic model in order to understand the spatial and temporal distribution of Fmiso in the tumor tissue. Since the predictive character of Fmiso SUV remains unclear in literature [13,16], the time course of tracer accumulation in the tumor was investigated. This analysis delivers patient specific values for perfusion, kinetic constants and the concentration of tracer retaining cells. Furthermore, the relation between these parameters and radiation therapy (RT) treatment outcome for HNC was investigated in a group of 15 HNC patients who were examined with dynamic Fmiso PET prior to treatment with primary radiotherapy.

Methods

Patients

After informed consent, sixteen patients (mean age: 57.2 years old, range: 46 – 69; 14 male, 2 female) with advanced stage head and neck cancer (HNC) were examined between November 2001 and March 2004. The Fmiso examinations were performed prior to radiation therapy (RT) treatment. All patients were treated with primary RT to 70 Gy. Three of these patients were treated with Intensity Modulated Radiotherapy (IMRT) in 35 fractions, 5 fractions a week with a daily dose of 2 Gy. The other 13 patients received conventional RT, 5 fractions with 2 Gy per week until 30 Gy. This first phase was followed by a hyperfractionation composed of a dose of 1.4 Gy applicated twice per day until the end of treatment. In addition, concomitant chemotherapy was prescribed for 14 patients. Seven patients received 5-Fluorouracil/Mitomycin chemotherapy, whereas for six patients Cisplatin/Mitomycin was prescribed; one patient had Paclitaxel/Cisplatin chemotherapy. Whenever possible (n = 12), an additional [^{18}F]-fluorodeoxyglucose (FDG) PET was taken a few days (1 – 3) before or after the Fmiso PET scan. For each patient, additional computed tomography (CT) image data was available. These CT scans, on which delineation of target volumes and organs at risk was performed, were used for RT treatment planning.

After the end of therapy, patients were reviewed regularly every three months with clinical examination, flexible endoscopy and computed tomography (CT) when recurrent disease was suspected. Routine CT scans were also acquired six weeks and one year after therapy was finished. Failure was defined as CT proven tumor progression.

Data acquisition

The Fmiso PET examinations were performed on a whole-body scanner (Advance, GE Medical Systems, Milwaukee, US) after automatic bolus injection of 400 MBq Fmiso. PET data acquisition was started at the time of tracer injection. During the first 15 (9 patients) to 60 min (7 patients), a dynamic image acquisition of 31 (40) frames was performed. Additional static emission scans were taken 2 h and 4 hour post injection (p.i.). Concerning the

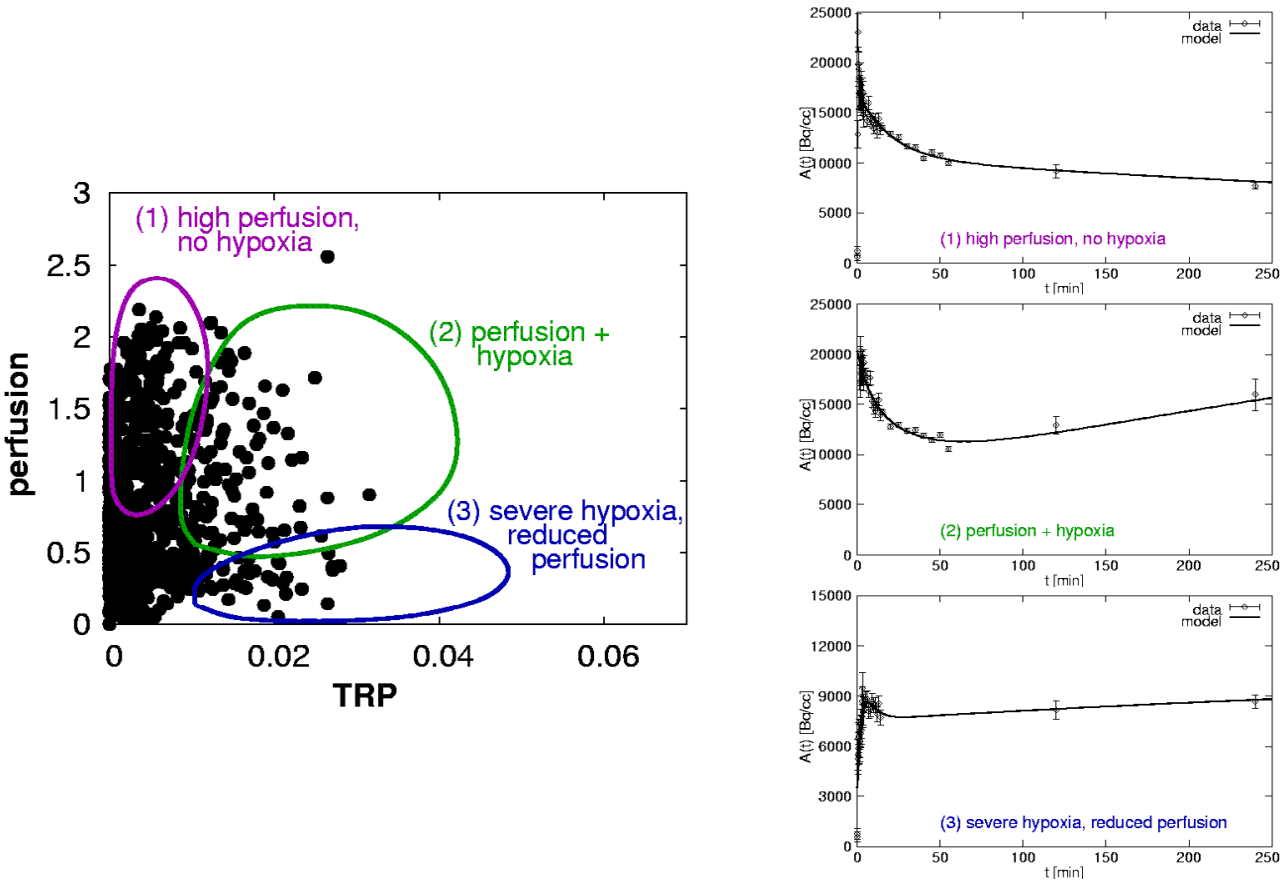

Figure 1
Left: Scatter plot for one patient based on tracer retention and perfusion parameters resulting from a kinetic Fmiso analysis. Schematically shown are typical regions for characteristic perfusion-hypoxia patterns: (1) High perfusion without hypoxia, (2) well perfused and simultaneously hypoxic, and (3) severe hypoxia, low vessel density. *Right*: Corresponding types of characteristic Fmiso Time-Activity Curves.

FDG PET acquisition, a static emission scan was taken 1 h after injection of approximately 400 MBq FDG.

For the delineation of the tumor volume relevant in the context of this study, the FDG PET image data was used. The tumor volume was defined as the volume including all voxels with at least 40% of the maximum intensity. This delineation technique was combined with a 12 mm margin (3 PET voxels). The tumor volume variable V used in the current study refers to the described FDG PET volume. It is determined as $V = n \cdot v$, where n is the number of tumor voxels. v represents the volume of a single voxel, in our case $v = (0.4^2 \cdot 0.425)\ \text{cm}^3 = 0.068\ \text{cm}^3$. In order to match the FDG-defined tumor volume onto the three different Fmiso data sets (dynamic, 2 and 4 h p.i.), an automatic coregistration [24] was performed, which achieved a matching accuracy of ≤ 2 mm. The resulting transformation matrices were used to determine a time-activity curve (TAC) for each tumor voxel.

Compartment model

The voxel-by-voxel TACs were analyzed using a pharmaco-kinetic model which is described in detail elsewhere [25]. Briefly, the kinetic model consists of two compartments, one corresponding to the irreversible binding of the tracer in hypoxic cells, the other representing freely diffusive Fmiso. This two-compartment system is combined with an input function which is individually determined by a reference tissue approach for lack of a blood signal in the field of view of the scanner (see [25] for details). The voxel-by-voxel analysis of the Fmiso TACs was done by fitting the five-parameter analytical model function for the tracer concentration in the tissue compartments to the measured Fmiso curves. This approach

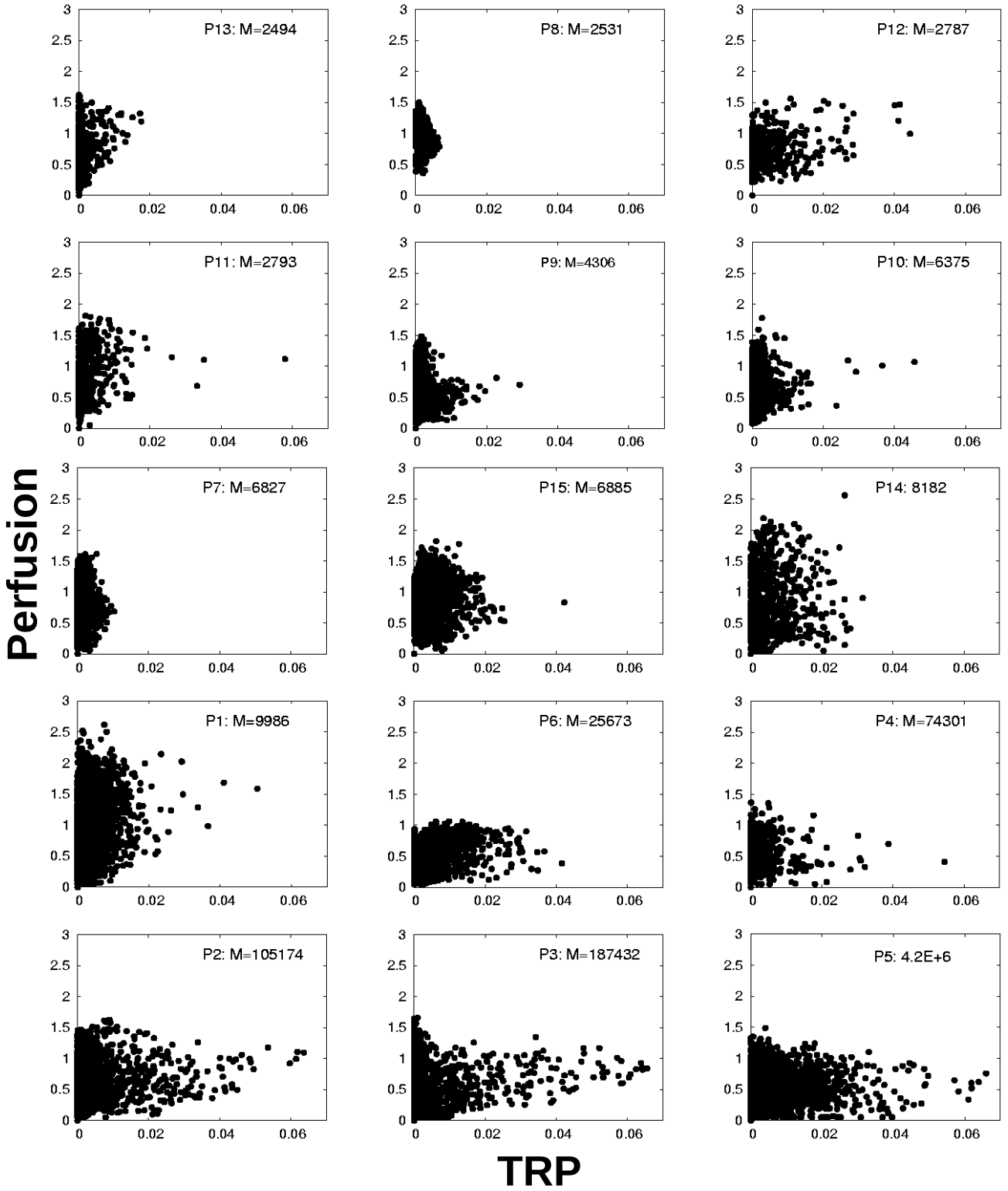

Figure 2
Scatter plots of all 15 patients with increasing *M*-value.

Table 1: patient characteristics. Tumor characteristics of the examined patients.

Patients						
Pat. nr.	primary tumor site	age	sex	TNM stage	tumor volume *V* [cm³]	failure site
1	oropharynx	60	m	T4 N2b M0	258.1	T*/N†
2	oropharynx	51	m	T4 N2c M0	126.2	T*
3	larynx	66	m	T4 N2c M0	153.7	T*/N†
4	FOM‡	46	m	T3 N2b M0	59.0	T*
5	BOT§	49	m	T4 N2c M0	287.6	T*/N†
6	oropharynx	48	m	T2 N2c M0	114.7	T*/N†
7	FOM‡	68	m	T4 N1 M0	213.7	T*/N†
8	oropharynx	65	m	T3 N2c M0	74.3	-
9	hypopharynx/ BOT§	51	m	T4 N2c M0	100.9	-
10	oropharynx	59	m	T2 N3 M0	172.4	-
11	oropharynx	50	f	T4 N2c M0	44.0	-
12	larynx-/ hypopharynx	60	m	T4 NO M0	32.4	-
13	oro-/hypopharynx	49	m	T3 N2c M0	80.9	-
14	oropharynx	60	f	T4 N2b M0	52.4	-
15	unknown	68	m	T4 N1 M0	125.5	-

*T: tumor; †N: node.
‡FOM: floor of mouth; §BOT: base of tongue.

yields for each tumor voxel one characteristic value for tracer retention and perfusion. The perfusion value, i.e. the density of perfused blood vessels in the respective tumor voxel, is mainly guided by the shape of the TAC during the first few minutes after injection. In contrast, the amount of tracer retention potential (TRP) in the voxel is related to the properties of the curve several hours after tracer injection. TRP takes into account the number of viable hypoxic cells as well as their grade of hypoxia. In other words, TRP is a measure of the concentration of specifically bound tracer in the considered area. Fluctuations in perfusion states are taken into account by construction of the model [25]. In order to visualize TRP and perfusion characteristics of the whole tumor simultaneously, a *scatter plot* is introduced (see appendix and fig. 1). In this plot, the TRP in a voxel is plotted along the *x*-axis, while the contribution to the signal from perfused blood vessels is plotted along the *y*-axis. The variety of scatter patterns in the patient group leads to the hypothesis that TRP and perfusion are independent and spatially variable parameters of a tumor tissue (see figure 2).

Data analysis and statistics

Tumor control was defined on the basis of computed tomography (CT) scans as complete and persistent regression of the primary tumor and failure was defined as local recurrence of the tumor in the irradiated fields. Follow up time was determined from the end of RT treatment until the day of the last CT. Different variables that might influence treatment outcome were compared using the Wilcoxon-Mann-Whitney (Wilcoxon signed rank) *U*-test between patient groups showing no local relapse and failure. In all cases, a two-sided significance level of 0.05 was used. Correlation of different variables with was assessed using a Pearson correlation coefficient.

The impact on treatment outcome was checked for different classes of variables: tumor volume and patient age, SUV related factors and variables derived from the kinetic analysis. The SUV related factors were the maximum standardized uptake value (SUV_{max}) and the fractional hypoxic volume (FHV) 4 h after Fmiso injection. FHV is defined as the fraction of tumor volume presenting a tumor-to-blood ratio larger than 1.4. Both variables SUV_{max} and FHV have been correlated with tumor hypoxia in earlier studies [11,13]. Finally, a number of parameters derived from the compartmental analysis were checked for a statistically significant influence on therapy outcome. These parameters were the mean value of TRP, the mean value of perfusion, and two metrics involving both TRP and perfusion parameter values. A first metric was defined intuitively as the volume integral of the TRP-to-perfusion ratio (HPR). A second metric, which was derived from a model of tumor dose-response and reoxygenation, is the *malignancy value M* as described in more detail in the appendix.

Table 2: results of statistical analysis. Results of univariate analysis of prognostic factors.

Results *U*-Test	
variables	*P*-Value
age [years]	NS* (0.30)
tumor volume *V* [cm³]	0.014
$SUV^{\dagger}_{max}$	0.041
FHV‡ [%]	NS* (0.13)
mean TRP*	NS* (0.18)
mean perfusion§	0.05
HPR§	0.008
malignancy value *M*§	0.001

*NS: not significant ($p > 0.05$); †SUV_{max}: maximum SUV; ‡FHV: fractional hypoxic volume.
§derived from kinetic model

Results

Kinetic Fmiso data

The voxel-by-voxel Fmiso TACs showed a variety of different tracer uptake patterns. Perfusion and hypoxia status of the tissue area can be differentiated by means of the Fmiso TAC shape. The former is determined by the part of the TAC corresponding to time points only a few minutes p.i, whereas the latter is linked to the shape of the curve several hours after tracer injection. The TACs observed for the group of 16 patients showed mainly three different types of perfusion-hypoxia patterns which correspond to (1) tissue areas with a high vessel density, (2) well perfused but also hypoxic, and (3) severely hypoxic tumor areas (see fig. 1).

Model

The presented compartment model allows us to derive patient specific perfusion-hypoxia patterns. The model is able to describe the different observed types of Fmiso time curves. Characteristic TACs are associated to distinct areas in the scatter plot (figure 1), which indicates high stability of the model. The patterns for the whole group of patients are displayed in scatter plots in figure 2 (appendix). The ultimate purpose of the kinetic model is to subtract the background of unbound tracer from the signal intensity.

Patients

Characteristics of the group of 15 patients are summarized in table 1. For the examined patient group, the follow up time was in the range of 2 – 21 months (median: 12.8 months). Patients were 46 to 68 years old (median: 59 years). FDG-tumor volumes ranged from 32.4 to 287.6 cm³ with a median volume of 114.5 cm³. Overall, 7 of the 15 patients had local recurrences. All observed failures occurred in the first 8 months after the end of therapy.

Image analysis of the Fmiso PET scans taken 4 h p.i. revealed maximum SUVs in the tumor volume between 1.36 and 4.02. The median SUV_{max} was 2.25. The FHV ranged from 0 to 72.5% with a mean of 19.7%. Due to the chosen tumor volume definition strategy, which implies the addition of a margin, the determined FHV can never reach 100%.

Examination of the scatter plots showed very different patterns of hypoxia and perfusion. All possible combinations of hypoxia and perfusion parameters were observed: well perfused tumors which were not at all hypoxic, tumors showing at the same time a quite high vascular density and hypoxic subareas, and finally also tumors that were badly perfused and severely hypoxic. These two variables represent physiological tumor characteristics that are not correlated ($r = -0.096$). As a first result, it has to be stated that hypoxia occurs independently from the degree of perfusion in tumor tissues.

The Wilcoxon-Mann-Whitney *U*-test with respect to the age of the patients showed no difference ($P = 0.3$) between the subgroups with and without relapse. In contrast, there was a significant difference in tumor volume between the two subgroups ($P = 0.014$). This corroborates the findings of earlier studies that correlated tumor size with treatment outcome [26]. Also, SUV_{max}, determined 4 h after injection separated patients according to failure and progression free survival (PFS). The significance for SUV_{max} was only weak $P = 0.041$, whereas the *U*-test for the FHV showed no significance at all ($P = 0.13$).

Regarding the variables derived from the kinetic analysis, mean tumor perfusion and HPR discriminated between the group without recurrence and the failure group ($P = 0.05$ and 0.008, respectively). The mean TRP value showed no significance ($P = 0.18$). Finally, the malignancy value *M* was highly significant, with $P = 0.0013$ (table 2). The prognostic value of this model based metric *M* is higher than the value of tumor size or SUV_{max} after 4 h.

Discussion

Recent publications revealed contradictory results concerning the correlation of static Fmiso PET data and tumor hypoxia [11-13,16]. As the irregular architecture of tumors complicates Fmiso uptake, a kinetic model was developed in order to analyze spatial and temporal distribution of the tracer in head-and-neck tumors. The presented model enables to differentiate between tumor perfusion and hypoxia. This feature of the model consti-

tutes the link between Fmiso distribution and retention and the structural architecture of the tumor tissue.

The results of this study showed, that SUV_{max} alone even at late time points has limited predictive value. These findings are in line with results of other investigators [16] who found that SUV 2 h p.i. and Eppendorf did not correlate well.

A limiting factor for the retention of Fmiso in the tumor is that binding of the tracer can only take place in *viable* hypoxic cells which may be few if the tumor is largely necrotic. In other words, a low level of the Fmiso TAC several hours after tracer injection is not necessarily due to non-hypoxic tissue. This might also be caused by largely necrotic tumor areas which contain only a very low number of strongly hypoxic cells. In this case, the low intensity of the PET signal would lead to an underestimation of the extent of hypoxia by the SUV-method. A kinetic analysis subtracts the non-specific background signal and hence enables to determine the local TRP of the tumor. Still, the classical hypoxic tumor core may only give a weak signal due to the low density of tracer retaining cells. Hence, a second parameter is needed to give a more complete picture of the abnormalities of the tissue architecture.

The analysis of the parameters derived from the kinetic model demonstrated, that TRP and perfusion values alone do not predict treatment outcome. Additionally, hypoxia occurred independent of degree of perfusion, since no correlation was found between the two variables. Recent immunohistochemical investigations of simultaneous pimonidazole and blood vessel staining of tissue sections [21-23] revealed the co-existence of hypoxic areas and perfused blood vessels. These results were corroborated in our study. Taking both parameters together proved to be reliable predictors for treatment outcome. The malignancy metric *M*, which involves these two physiological characteristics of the tissue, was found to be the strongest prognostic factor.

Most essential for the design of new adaptive treatment strategies is the time until reoxygenation takes place after the beginning of RT. The malignancy metric *M* involves an estimate of this characteristic time. The worst physiological setting in a tumor seems to be the combination of low perfusion and severe hypoxia, as reoxygenation then appears to be very slow. In contrast, a high degree of perfusion co-existing with hypoxic areas may favor fast reoxygenation. Hence, this setting might be associated with an intermediate level of risk. This interpretation can be supported by follow-up scans during RT, which will be reported in a future publication.

Fmiso uptake kinetics are quite slow due to long diffusion distances and for lack of active transport mechanisms. PET scans several hours after injection of the radiotracer are therefore essential. Nevertheless, dynamic scans at short times p.i. cannot be abandoned, as they are needed to determine the degree of perfusion of the tumor.

There is no possibility in Fmiso PET to distinguish between acute and chronic hypoxia [27]. On one hand, this is due to a quite large size of the image voxels ($\approx (4\ mm)^3$). On the other hand, the slow kinetics of tracer retention do not allow a distinction of fast re-perfusion. Since both effects are a consequence of the deficient vasculature, they may co-exist anyway.

The results of this study demonstrate that Fmiso PET has prognostic value for therapy outcome, but only when perfusion and retention are both taken into consideration. A higher predictive value was associated to the malignancy value *M* derived form kinetic analysis than to tumor volume or SUV based variables. Hence, Fmiso PET might in the future be used to individually select patients for an adapted radiotherapy treatment as e.g. dose painting [18-20]. Furthermore, variables derived from a kinetic analysis [25] may serve to determine individual dose escalation factors in order to overcome hypoxia related treatment resistance.

Conclusion

The interpretation of Fmiso PET examinations with respect to hypoxia benefits greatly from a kinetic analysis. The presented kinetic analysis determines hypoxia and perfusion parameters, which were shown to be able to stratify patient groups according to RT treatment outcome. The results of this explorating, hypothesis generating study require validation in a larger group of patients.

Appendix

Scatter plots

By virtue of the kinetic model analysis of the time-activity curves of tracer uptake, it is possible to eliminate the non-specific background activity in the signal. The model has five fit parameters, which are determined for each voxel of the tumor volume. Two parameters are of special interest: the relative contribution of the perfused blood vessels, short W_P, which dominates the signal during the first few minutes after injection. Further, the tracer retention potential *R*, which is a combination of the concentration of retaining cells and the kinetic constants of the reaction. In a scatter plot, the values of *R* are plotted along the *x*-axis, and the values of W_P are plotted along the *y*-axis for all voxels of the tumor volume. The scatter plots of all 15 patients in figure 2 show clearly that both values are independent variables and vary widely in a population.

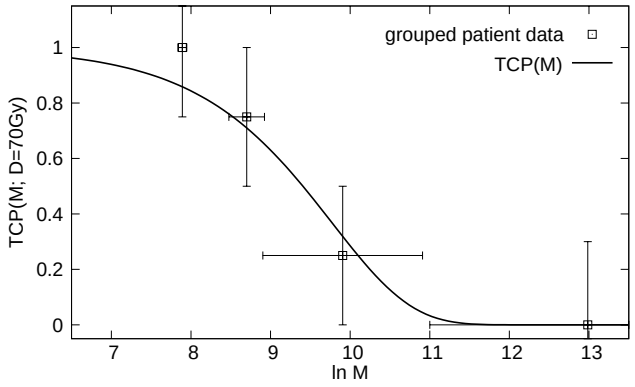

Figure 3
TCP curve fitted to the outcome data of 15 patients irradiated with a total dose of 70 Gy.

TCP model

The resistance of a hypoxic tumor to RT is governed, among others, by two factors: the initial magnitude of the hypoxic subpopulation of clonogenic cells, and the rate with which these cells are reoxygenated. We assume that the former is related to R, while the latter is related to W_P. The rationale for the second assumption is, that in areas where the blood vessel density is high, hypoxic cells have a greater chance to become oxic quickly. Conversely, if the vasculature is severely deficient, reoxygenation is delayed. The common Poisson model of tumor control probability (TCP) states:

$$-\ln \mathrm{TCP}\,(D) = \sum_i n \exp(-\alpha_0 D) \qquad (1)$$

where the sum runs over all voxels i of the tumor and n is the number of cells per voxel. D is the total dose and α_0 the radiation sensitivity of a non-hypoxic cell. We modify this to include hypoxic subpopulations to read

$$-\ln \mathrm{TCP}(D) = \sum_i \int d\alpha_h \, n h_i(\alpha_h) \exp(-(\alpha_0 - \alpha_h) D) \qquad (2)$$

$$= n \exp(-\alpha_0 D) \sum_i \int d\alpha_h \, h_i(\alpha_h) \exp(\alpha_h D). \qquad (3)$$

Here, $h(\alpha_h)$ is the frequency with which an average reduction of the cell sensitivity by α_h occurs over the course of the treatment. The integral is the malignancy M. We define a phenomenological relation between the kinetic model parameters and the malignancy by:

$$M = 1 + \exp(bR/(W_P + c)), \qquad (4)$$

where b and c are fit parameters. Finally, we obtain

$$-\ln \mathrm{TCP}(D) = a \sum_i [1 + \exp(bR_i/(W_{P,i} + c))] \qquad (5)$$

with $a = n \exp(-\alpha_0 D)$ as an additional fit parameter. This sum can be computed as a sum over the points of a scatter plot.

The parameters a, b and c were determined by a maximum log-likelihood fit of TCP to the group of 15 patients in this study. Their values obtained as $a = 5.7 \cdot 10^{-5}$, $b = 198.6$ and $c = 0.565$. The goodness of fit was estimated by evaluation of the deviance Δ. The deviance is defined as twice the difference between the current and the full log-likelihood $\Delta = -2(L_c - L_f)$, which is supposed to follow a χ^2 distribution. In our case, the deviance confirmed an acceptable fit ($\Delta = 2.75$, $p > 0.05$).

Figure 3 shows the the fitted TCP curve as a function of the malignancy value M together with the grouped data points obtained from outcome data for the group of 15 patients in this study.

Competing interests

The author(s) declare that they have no competing interests.

Authors' contributions

DT developed the kinetic model, the parameter analysis strategy, and the TCP model, performed all data analysis, and drafted the manuscript. SE carried out all PET examinations and acquired the data. FP was involved in the design of the study and its coordination. JS participated in the design of the study and performed the statistical analysis. MA conceived the study, developed the kinetic model and the TCP model, has made substantial contributions for data interpretation and was participated in drafting the manuscript. All authors read and approved the final manuscript.

Acknowledgements

This project has been financially supported by the German Research Foundation (DFG), grant no. AL 877/1. The authors would like to thank Prof. H-J Machulla and his team (Radiopharmacy Section, University Hospital Tübingen) for excellent [^{18}F]-Fmiso production. We also thank Dr. C Belka for careful manuscript revision.

References

1. Brizel DM, Albers ME, Fisher SR, Scher RL, Richtsmeier WJ, Hars V, George SL, Huang AT, Prosnitz LR: **Hyperfractionated irradiation with or without concurrent chemotherapy for locally advanced head and neck cancer.** *N Engl J Med* 1998, **338(25):**1798-1804.
2. Budach V, Stuschke M, Budach W, Baumann M, Geismar D, Grabenbauer G, Lammert I, Jahnke K, Stueben G, Herrmann T, Bamberg M, Wust P, Hinkelbein W, Wernecke K: **Hyperfractionated accelerated chemoradiation with concurrent fluorouracil-mitomycin is more effective than dose-escalated hyperfractionated accelerated radiation therapy alone in locally advanced head**

and neck cancer: final results of the radiotherapy cooperative clinical trials group of the German Cancer Society 95-06 Prospective Randomized Trial. *J Clin Oncol* 2005, **23(6):**1125-1135.
3. Coleman CN, Mitchell JB, Camphausen K: **Tumor Hypoxia: Chicken, Egg, or a Piece of the Farm? (editorial).** *J Clin Oncol* 2002, **20:**610-615.
4. Fyles A, Milosevic M, Hedley D, Pintilie M, Levin W, Manchul L, Hill RP: **Tumor Hypoxia has Independent Predictor Impact Only in Patients With Node-Negative Cervix Cancer.** *J Clin Oncol* 2002, **20:**680-687.
5. Weinmann M, Belka C, Plasswilm L: **Tumour hypoxia: impact on biology, prognosis and treatment of solid malignant tumours.** *Onkologie* 2004, **27:**83-90.
6. Weinmann M, Jendrossek V, Guner D, Goecke B, Belka C: **Cyclic exposure to hypoxia and reoxygenation selects for tumor cells with defects in mitochondiral apoptotic pathways.** *FASEB* 2004, **18(15):**1906-1908.
7. Nordsmark M, Overgaard M, Overgaard J: **Pretreatment oxygenation predicts radiation response in advanced squamous cell carcinoma of the head and neck.** *Radiother Oncol* 1996, **41:**31-39.
8. Nordsmark M, Overgaard J: **A confirmatory prognostic study on oxygenation status and loco-regional control in advanced head and neck squamous cell carcinoma treated by radiation therapy.** *Radiother Oncol* 2000, **57:**39-43.
9. Brizel DM, Sibley GS, Prosnitz LR, Scher RL, Dewhirst MW: **Tumor hypoxia adversely affects the prognosis of carcinoma of the head and neck.** *Int J Radiat Oncol Biol Phys* 1997, **38(2):**285-289.
10. Höckel M, Knoop C, Schlenger K, Vorndran B, Knapstein PG, Vaupel P: **Intratumoural pO_2 predicts survival in advanced cancer of the uterine cervix.** *Radiother Oncol* 1993, **26:**35-50.
11. Rasey JS, Koh WJ, Evans ML, Peterson LM, Lewellen TK, Graham MM, Krohn KA: **Quantifying regional hypoxia in human tumours with positron emission tomography of [^{18}F] fluoromisonidazole: A pretherapy study of 37 patients.** *Int J Radiat Oncol Biol Phys* 1996, **36(2):**417-428.
12. Koh WJ, Rasey JS, Evans ML, Grierson JR, Lewellen TK, Graham MM, Krohn KA, Griffin TW: **Imaging of hypoxia in human tumours with [F-18]fluoromisonidazole.** *Int J Radiat Oncol Biol Phys* 1992, **22:**199-212.
13. Eschmann SM, Paulsen F, Reimold M, Dittmann H, Welz S, Reischl G, Machulla HJ, Bares R: **Prognostic Impact of Hypoxia Imaging with ^{18}F-Misonidazole PET in Non-Small Cell Lung Cancer and Head and Neck Cancer Before Radiotherapy.** *J Nucl Med* 2005, **46:**253-260.
14. Piert M, Machulla HJ, Picchio M, Reischl G, Ziegler S, Kumar P, Wester HJ, Beck R, McEwan AJB, Wiebe LI, Schwaiger M: **Hypoxia-Specific Tumor Imaging with ^{18}F-Fluoroazomycin Arabinoside.** *J Nucl Med* 2005, **46:**106-113.
15. Dehdashti D, Grigsby PW, Aintun MA, Lewis JS, Siegel BA, Welch M: **Assessing tumour hypoxia in cervical cancer by positron emission tomography with ^{60}Cu-ATSM: Relationship to therapeutic response – a preliminary report.** *Int J Radiat Oncol Biol Phys* 2003, **55(5):**1233-1238.
16. Bentzen L, Keiding S, Nordsmark M, Falborg L, Hansen SB, Keller J, Nielsen OS, Overgaard J: **Tumour oxygenation assessed by ^{18}F-fluoromisonidazole PET and polarographic needle electrodes in human soft tissue tumours.** *Radiother Oncol* 2003, **67:**339-344.
17. Rasey JS, Nelson NJ, Chin L, Evans ML, Grunbaum Z: **Characteristics of the binding of labeled fluoromisonidazole in cells in vitro.** *Radiat Res* 1990, **122(3):**301-308.
18. Ling Hummi JCC, Larson S, Amols H, Fuks Z, Leibel S, Koutcher JA: **Towards multidimensional radiotherapy (MD-CRT): biological imaging and biological conformality.** *Int J Radiat Oncol Biol Phys* 2000, **47(3):**551-560.
19. Chao KS, Bosch WR, Mutic S, Lewis JS, Dehdashti F, Mintun MA, Dempsey JF, Perez CA, Purdy JA, Welch MJ: **A novel approach to overcome hypoxic tumour resistance: Cu-ATSM-guided intensity-modulated radiation therapy.** *Int J Radiat Oncol Biol Phys* 2001, **49(4):**1171-1182.
20. Alber FM, Paulsen , Eschmann SM, Machulla HJ: **On biologically conformal boost dose optimization.** *Phys Med Biol* 2003, **48:**N31-N35.
21. Ljungkvist ASE, Bussink J, Rijken PFJW, Kaanders JH, van der Kogel AJ, Denekamp J: **Vascular architecture, hypoxia, and proliferation in first-generation xenografts of human head-and-neck squamous cell carcinomas.** *Int J Radiat Oncol Biol Phys* 2002, **54:**215-228.
22. Janssen HL, Haustermans KMG, Sprong D, Blommestijn G, Hofland I, Hoebers FJ, Blijweert E, Raleigh JA, Semenza GL, Varia MA, Balm AJ, van Velthuysen MF, Delaere P, Sciot R, Begg AC: **HIF-1A, pimonidazole, and iododeoxyuridine to estimate hypoxia and perfusion in human head-and-neck tumours.** *Int J Radiat Oncol Biol Phys* 2002, **54(5):**1537-1549.
23. Janssen HL, Hoebers FJ, Sprong D, Goethals L, Williams KJ, Stratford IJ, Haustermans HM, Balm AJ, Begg AC: **Differentiation-associated staining with anti-pimonidazole antibodies in head and neck tumours.** *Radiother Oncol* 2004, **70:**91-97.
24. Viola P, Wells WM: **Alignment by Maximization of Mutual Information.** *Int J Comp Vision* 1997, **24(2):**137-154.
25. Thorwarth D, Eschmann SM, Paulsen F, Alber M: **A kinetic model for dynamic [^{18}F]-Fmiso PET data to analys.** *Phys Med Biol* 2005, **50:**2209-2224.
26. Plataniotis GA, Theofanopoulou ME, Kalogera-Fountzila A, Haritanti A, Ciuleanou E, Ghilezan N, Zamboglou N, Dimitriadis A, Sofroniadis I, Fountzilas G: **Prognostic impact of tumor volumetry in patients with locally advanced head-and-neck carcinoma (non-nasopharyngeal) treated by radiotherapy alone or combined radiochemotherapy in a randomized trial.** *Int J Radiat Oncol Biol Phys* 2004, **59(4):**1018-1026.
27. Denekamp J, Dasu A: **Inducible Repair and the Two Forms of Tumour Hypoxia – Time fir a Paradigm Shift.** *Acta Oncol* 1999, **38(7):**903-918.

Pre-publication history

The pre-publication history for this paper can be accessed here:

http://www.biomedcentral.com/1471-2407/5/152/prepub

Appendix C

Combined uptake of [^{18}F]-FDG and [^{18}F]-FMISO correlates with radiation therapy outcome in head-and-neck cancer patients

published in
Radiotherapy and Oncology 2006; **80**: 151-156

Radiotherapy and Oncology 80 (2006) 151–156
www.thegreenjournal.com

Hypoxic markers

Combined uptake of [^{18}F]FDG and [^{18}F]FMISO correlates with radiation therapy outcome in head-and-neck cancer patients

Daniela Thorwarth[a,*], Susanne-Martina Eschmann[b], Felix Holzner[a], Frank Paulsen[c], Markus Alber[a]

[a]*Section for Biomedical Physics, Clinic for Radiation Oncology, Tübingen, Germany,* [b]*Department of Nuclear Medicine, Radiological Clinic, Tübingen, Germany,* [c]*Department of Radiation Therapy, Clinic for Radiation Oncology, Tübingen, Germany*

Abstract

***Purpose*: FDG PET is frequently used for radiotherapy (RT) planning to determine the tumour extent. Similarly, FMISO is used to assess the hypoxic sub-volume. The relationship between the volumes determined on the basis of FDG and FMISO was investigated. Additionally, the quantitative correlation of the tracers on a voxel basis was studied.**

***Methods*: Twelve head-and-neck cancer (HNC) patients underwent FDG and FMISO PET examinations prior to RT treatment. The tumour volumes assessed by the two tracers and also the voxel-based joint uptake values were investigated. The characteristic shapes and patterns of the determined scatter plots were analyzed.**

A number of different variables such as the maximum uptake values of FDG and FMISO, the FDG and FMISO positive volumes, the slope *m* of the regression line and the scatter width σ of the scatter plots were tested for their ability to stratify the patient group with respect to treatment outcome.

***Results*: A diversity of characteristic FDG-FMISO distributions was observed in the patient group. However, no general correlation of enhanced glucose metabolism and FMISO uptake was observed.**

The maximum uptake of FMISO ($p = 0.045$) showed borderline significance for stratifying the patient group. FDG positive tumour volume, hypoxic fraction, maximum FDG uptake and *m* were not significant. σ turned out to be the most significant variable ($p = 0.008$) to predict treatment success probabilities.

***Conclusion*: FMISO and FDG PET data provide independent information about the examined tumour. A quantification of the correlated tracer uptake seems to be meaningful.**

Keywords: FMISO; FDG; PET; Hypoxia; Head-and-neck cancer

[^{18}F]Fluorodeoxyglucose (FDG) positron emission tomography (PET) is being established as a solid basis for target volume delineation in the radiotherapy (RT) planning process for head-and-neck cancer (HNC) [2]. Additional information imaged by tracers such as [^{18}F]Fluoromisonidazole (FMISO) could form the basis for dose painting.

Tumour hypoxia has been shown to be one of the major factors affecting therapy resistance [4]. Also, enhanced glucose metabolism was determined to be a predictor for reduced survival probabilities [8]. Despite this analogy, it remains unclear how the local tracer uptake is related and what this reveals about the two phenomena tumour hypoxia and enhanced glucose metabolism in tumours. Tumour tissues that present a high metabolic activity often show also enhanced proliferation rates [1]. In combination with insufficient neovascularization these high proliferation rates could lead to tumour hypoxia. Conversely, glucose metabolism may be activated under hypoxic conditions [7,9–11,13].

Modern imaging technologies, especially PET, allow non-invasive imaging of both hypoxia and glucose metabolism. FDG is the most common tracer to visualize the intra-tumoural glucose metabolism [8]. FDG is used in clinical routine for tumour detection, staging, RT target volume definition and therapy monitoring [5]. To assess tumour hypoxia by means of PET, FMISO is one of the most frequently employed tracers [3,6,12,14].

Different investigators analyzed the correlation of hypoxia and energy status in tumours. Pugachev et al. [9] performed immunohistochemical studies on one human prostate tumour cell strain in mice in order to compare the staining intensities of FDG and pimonidazole, which is identical to FMISO by way of its binding mechanism. A positive correlation between FDG and pimonidazole staining intensities was determined in this study, and higher FDG

0167-8140/$ - see front matter doi:10.1016/j.radonc.2006.07.033

uptake was described to be indicative of tumour hypoxia. Other investigators [7,13] reported that glucose consuming and FMISO trapping regions showed wide overlaps. On the other hand, they also found differences in the distribution homogeneities. A combined use of FDG and FMISO was suggested to provide better information on individual tumour characteristics. Rajendran et al. [10,11] assumed the glucose metabolism of tumours to be affected by hypoxia. A general correlation could not be found, only for single cases correlations of FDG and FMISO were identified. The investigators found all different combinations of high/low hypoxia and high/low glucose metabolism in their study. They presumed an eventually tumour type specific correlation.

To date, it remains unclear if there is a general correlation of tumour hypoxia and glucose metabolism. The presented data hint at a wide variety of combined tracer uptake in addition to tumour specific patterns. Hypothetically, it seems possible that the quality of the relationship between these two phenomena in PET investigations might be a separate, individual characteristic of a tumour, reflecting its degree of structural heterogeneity on a microscopic level.

The presented study investigates the correlation between FDG and FMISO uptake in tumours in a clinical setting. The correlation of FDG and FMISO based volumes is studied. Additionally, the joint accumulation of FDG and FMISO in human HNC is analyzed on a voxel basis. Furthermore, the relationship between glucose metabolism, FMISO accumulation and therapy outcome is determined. The hypothesis that correlated uptake of FDG and FMISO might be an independent property of a tumour is investigated.

Methods and materials

Patients

After informed consent, a total of 12 patients with advanced stage HNC were included into this study. Prior to treatment, each patient underwent FMISO and FDG PET examination within a few days. Patient characteristics are summarized in Table 1.

All patients were treated with RT of 70 Gy. In addition, concomitant chemotherapy was prescribed for 11 patients. After the end of therapy, patients were reviewed regularly every three months with clinical examination, flexible endoscopy and computed tomography (CT). Failure was defined as CT proven tumour progression.

PET imaging

All PET examinations were performed on a whole-body scanner (Advance, GE Medical Systems, Milwaukee, US) with an axial field of view (FOV) of 14.9 cm. FDG and FMISO were both injected with a total activity of approximately 400 MBq. FDG scans were acquired 60 min after tracer injection. For the FMISO examinations, two static scans were recorded at 2 and 4 h post-injection (pi). The data were reconstructed with an iterative ordered subsets expectation maximization (OSEM) algorithm and had a spatial resolution of $4 \times 4 \times 4.25\ mm^3$.

Image analysis

The definition of regions of interest (ROIs) for a voxel-based analysis was based on the FDG scans. All voxels showing a higher intensity than 40% of the maximum value were included into the ROI. In a second step, this region was extended by 3 voxels in each direction. A hypoxic fraction (HF) was defined as the percentage of tumour voxels that presents FMISO standardized uptake values (SUVs) at 2 h pi larger than 1.4.

FMISO scans were matched to the FDG scans with a rigid registration algorithm that uses a mutual information (MI) metric [15]. This matching procedure was validated against manual fusion and showed errors of the order of 2 mm ($\approx$0.5 voxel).

Further analysis of voxel-by-voxel FDG-FMISO correlation was based on scatter plots. The FDG SUV is plotted on the *x*-axis versus the corresponding FMISO SUV on the *y*-axis. It is assumed that the later FMISO scans were taken, the more of

Table 1
Patient characteristics

Pat. #	Primary tumour site	Age	Sex	TNM stage	FDG vol [cm^3]	HF[c] [%]	Local relapse
1	Oropharynx	65	m	T3 N2c M0	22.9	75.2	n
2	Oropharynx	60	m	T4 N2b M0	67.0	47.0	y
3	Hypopharynx/BOT[a]	51	m	T4 N2c M0	22.5	20.1	n
4	Oropharynx	59	m	T2 N3 M0	67.6	89.4	n
5	Hypopharynx	65	m	T4 N2c M0	27.2	95.7	y
6	Oropharynx	50	f	T4 N2c M0	5.4	10.3	n
7	Larynx-/hypopharynx	60	m	T4 N0 M0	3.1	2.2	n
8	Larynx	66	m	T4 N2c M0	32.3	75.7	y
9	Oro-/ hypopharynx	49	m	T3 N2c M0	17.4	36.2	n
10	Unknown	68	m	T4 N1 M0	27.9	0.3	n
11	Oropharynx	48	m	T2 N2c M0	27.3	6.8	y
12	FOM[b]	68	m	T4 N1 M0	34.0	84.4	y

Tumour characteristics for all HNC patients.
[a] BOT, base of tongue.
[b] FOM, floor of mouth.
[c] HF, hypoxic fraction.

the unspecifically bound tracer had washed out. Hence, for the scatter plots only FMISO data acquired 4 h pi were used. Voxels with FDG and FMISO values below a certain threshold ($2/3x + y \leqslant 2$) were omitted from the scatter plots and any further analysis.

A regression line $f_r(x) = mx + b$ was fitted to each FDG-FMISO scatter plot and the scatter width σ was calculated. σ is determined by the width of a band delimited by two straight lines parallel to f_r. The scatter band is defined in such a way that 95% of the data points fall into this band.

In order to validate the stratification of patient groups according to different variables, the Student *t*-test was used. As the *t*-test is only valid for gaussian distributions and the sample size in our study is quite small, the Wilcoxon–Mann–Whitney *U*-test was applied for comparison. In all cases, a two-sided significance level of 0.05 was used.

Results

The tumour volume analysis revealed large differences in size for the FDG positive areas, ranging from 3.1 up to 67.0 cm^3. The bandwidth of HF was 0.3–95.7% (mean: 45.3%).

The results of the PET data analysis are shown in Table 2. Maximum FDG SUVs ranged from 8.00 to 12.07 (mean: 9.53). The range of maximum FMISO SUVs was 1.40–3.22 (mean: 2.20) at 4 h pi.

A first visual comparison of the scatter plots showed a large inter-patient diversity of FDG-FMISO distributions and revealed different characteristic types of scatter patterns (see Fig. 1). No general correlation of FDG and FMISO uptake was found. For some patients, very good voxel-by-voxel correlation of FDG and FMISO was observed. The scatter patterns were very narrow and could have suggested a functional dependence between FDG and FMISO uptake (cf. patients #4, 6, 7, 10, 11). In contrast, the scatter patterns of other patients were more irregular and no clear correlation between the uptake values of the two tracers could be observed.

Table 2
PET data analysis

Pat. #	FDG		$FMISO_{4h}$	
	SUV_{max}	SUV_{avg}	SUV_{max}	SUV_{avg}
1	8.88	3.35	2.22	1.49
2	7.87	3.22	2.15	1.18
3	9.65	3.24	1.80	1.14
3_{PT}[a]	9.65	3.24	1.37	1.11
3_{LN}[a]	7.94	3.38	1.80	1.24
4	7.84	3.80	2.27	1.47
5	12.07	3.10	2.93	1.41
6	10.75	3.47	1.40	0.98
7	10.49	3.34	1.58	1.07
8	9.20	3.75	2.65	1.32
9	9.10	3.19	2.73	1.20
9_{PT}[a]	9.03	2.99	1.45	1.06
9_{LN}[a]	9.10	3.48	2.73	1.49
10	8.00	3.25	1.51	0.97
11	10.41	3.84	1.66	0.96
12	10.09	3.55	3.22	1.44

[a] For patients #3 and 9, primary tumour (PT) and lymph node (LN) were spatially separated and analyzed separately.

Patients #3 and 9 presented with tumours where primary and a lymph node region were spatially separated. These two sub-regions were then further analyzed as separate ROIs. The scatter analysis resulted in completely different FDG-FMISO distributions for the two parts. In both cases, the scatter plot for the main tumour revealed very narrow and well-correlated FDG-FMISO scatter patterns, mostly because little FMISO uptake occurred. The lymph node regions in contrast presented widely dispersed data points of FDG and FMISO SUVs (Fig. 2).

The regression lines $f_r(x)$ manifested very different values for the slope *m*, ranging from 0.01 to 0.17. The scatter width σ ranged from 0.23 to 0.55, with a mean value of 0.38 (Table 3). In cases of spatially separated sub-tumours, regression line and scatter width were determined separately for each region (Fig. 3).

Variables tested for their ability to stratify the patient group with respect to treatment outcome were the FDG positive volume, the HF, the maximum FDG uptake, the maximum FMISO uptake at 4 h pi as well as the slope *m* of the regression line $f_r(x)$ and the scatter width σ. With the *t*-test non-significant *p*-values were determined for the FDG volume ($p = 0.130$), for the HF ($p = 0.101$) as well as for SUV_{max} of FDG ($p = 0.198$) and the slope *m* ($p = 0.10$). Maximum FMISO SUV ($p = 0.045$) was borderline significant. The scatter width σ resulted in a highly significant value of $p = 0.008$. The *p*-values obtained from the non-parametric *U*-test are shown for comparison in Table 4.

Discussion

Recent publications revealed inconclusive results concerning the correlation of glucose metabolism and hypoxia [7,9–11,13] which could be caused by a large variability of tumour biology and structural heterogeneity. The presented work investigates the correspondence between FDG and FMISO uptake in HNC patients. The results did not show a general correlation. These findings corroborate the results of Rajendran et al. [10,11] who reported no global correlation, but the presence of all possible combinations of high/low uptake of FDG and FMISO. However, our data did not reveal tumours with high FMISO and low FDG uptake.

A detailed analysis of FDG-FMISO scatter plots manifested large inter- and also intra-patient variations of FDG-FMISO distribution patterns. For some cases, a good correlation of the two tracers could be observed. In contrast to other investigators [9] this study also revealed tumours where no correlation of the glucose tracer FDG and the hypoxia tracer FMISO could be seen. One of the reasons why Pugachev et al. saw clear correlations might have been the fact that all investigated tumours were grown from the same cell line.

The two patients allowing a spatial differentiation between primary tumour and lymph node showed that the FDG-FMISO scatter patterns present not only inter-, but also

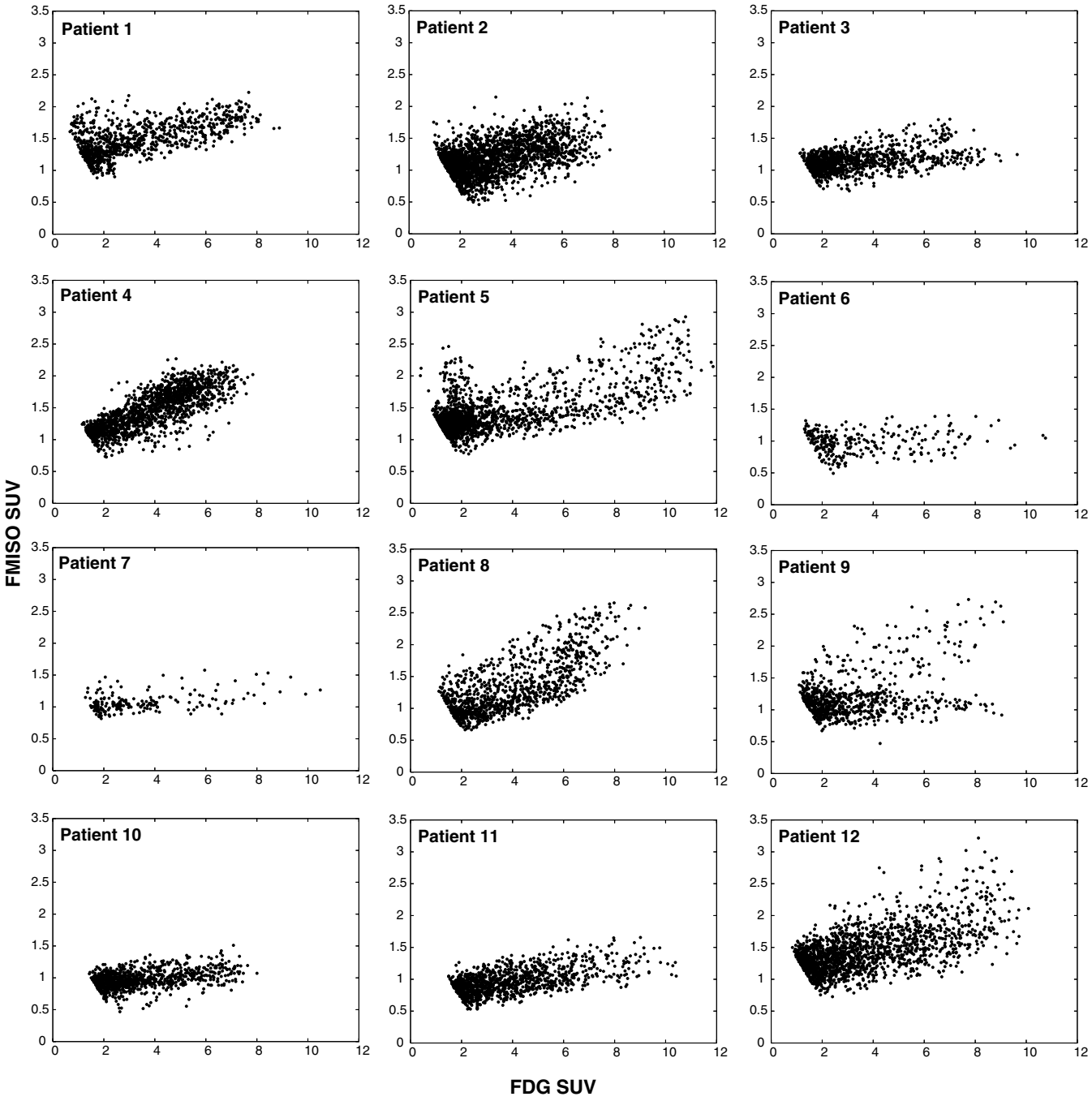

Fig. 1. FDG-FMISO scatter plots for all 12 patients. Data points that presented low SUVs for FMISO and FDG were omitted.

strong intra-patient variations. In these patients, each region separately showed a narrow correlation between FDG and FMISO.

The joint data of FDG and FMISO support the initial hypothesis: Correlated uptake of FDG and FMISO may be an independent property of a tumour of predictive value. Consequently, a good correlation of the two tracers might hint at a favourable situation in terms of treatment success probability, while the lack of correlation indicates the necessity of individually adapted treatment approaches.

In order to be able to define a quantitative measure for the shapes of FDG-FMISO distribution patterns, the scatter width σ was introduced. This parameter σ turned out to be the best predictor ($p = 0.008$) for RT treatment outcome. Thus, the parameter σ enables us to stratify patients according to their treatment outcome better than the other tested variables such as FDG tumour volume, HF, maximum FDG and FMISO SUV and the slope m of the regression line. This effect could be due to the fact that σ becomes small also if no FMISO uptake occurs. σ therefore represents a combination of two phenomena.

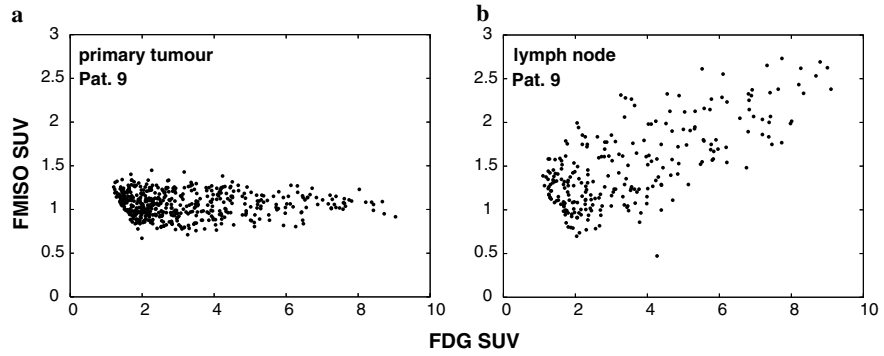

Fig. 2. FDG-FMISO scatter plots for the two different tumour parts of patient 9. (a) Primary tumour. (b) Lymph node.

Table 3
Scatter widths σ

Pat.	1	2	3	4	5	6	7	8	9	10	11	12
σ	0.42	0.45	0.23[a]	0.38	0.52	0.33	0.28	0.55	0.37[a]	0.25	0.29	0.53
Outcome[b]	+	–	+	+	–	+	+	–	+	+	–	–

[a] σ is a weighted mean according to the number of voxels associated to lymph node (LN) and primary tumour (PT) regions. Pat 3: $\sigma_{LN} = 0.24$, $\sigma_{PT} = 0.22$. Pat 9: $\sigma_{LN} = 0.58$, $\sigma_{PT} = 0.26$.
[b] outcome: –, local relapse; +, no local relapse.

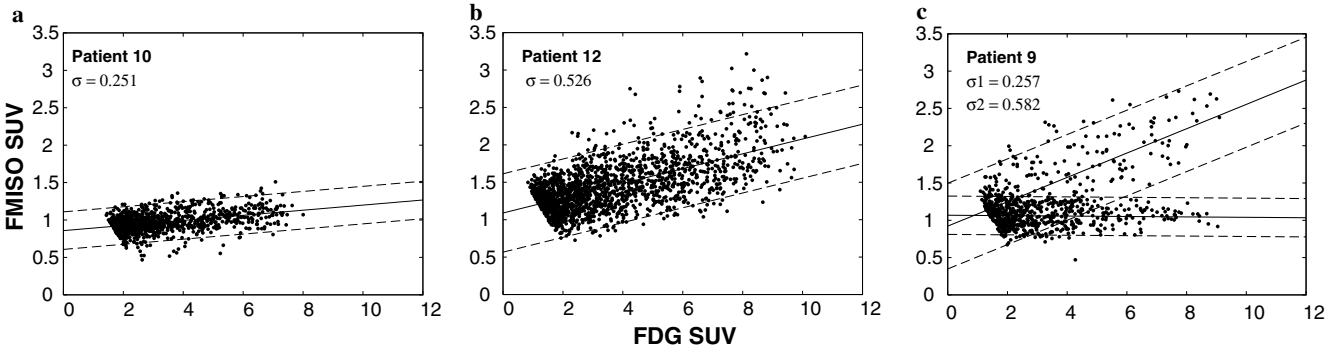

Fig. 3. Scatter widths σ exemplarily shown for three patients. (a) Patient 10, (b) Patient 12, and (c) Patient 9.

Table 4
Univariate statistical analysis

p-value	FDG vol.	HF	$FMISO_{4h}$ SUV_{max}	FDG SUV_{max}	m	σ
t-test	0.130	0.101	0.045	0.198	0.100	0.008
U-test	0.061	0.084	0.061	0.232	0.084	0.014

An attempt to interpret this result biologically could start with the assumption that there are three types of cells. High FDG uptake and no trapping of FMISO correspond to cells in well perfused areas, whereas high FDG and FMISO uptake levels hint at cells that metabolize glucose because of diffusion limited hypoxia. FMISO trapping and no FDG uptake signalizes that no oxygen or glucose are present at large distances from vessels. Hence, a good correlation between FDG and FMISO in a tumour hints at a well-balanced ratio between all types throughout the whole tumour. In contrast, a weak correlation indicates large regional differences in the ratio between all types. A weakly correlated uptake of FDG and FMISO seems to hint at a more malignant tumour phenotype that is prone to less regular growth.

Conclusion

Hypoxia is a consequence of an irregular vascular structure of a tumour, in whose formation excessive proliferation plays a significant role. Macroscopically imageable hypoxia

reflects microscopic heterogeneity in a complex fashion. The combined analysis of FMISO and FDG adds a second dimension to the investigation of this heterogeneity.

The presented study showed that the information obtained by FMISO cannot be substituted by FDG imaging. The joint use of both tracers in PET appears to be beneficial for the assessment of a more detailed image of local tumour characteristics.

Acknowledgements

This project was financially supported by the German Research Foundation (DFG), Grant No. AL 877/1. The authors thank the Radiopharmacy Department, University Hospital Tübingen, for [^{18}F]FMISO and [^{18}F]FDG production.

* **Corresponding author. Daniela Thorwarth**, Section for Biomedical Physics, University Clinic for Radiation Oncology Tübingen, Hoppe-Seyler-Str. 3, 72076 Tübingen, Germany. *E-mail address:* daniela.thorwarth@med.uni-tuebingen.de

Received 24 May 2006; received in revised form 17 July 2006; accepted 19 July 2006

References

[1] Avril N, Menzel M, Dose J, et al. Glucose metabolism of breast cancer assessed by 18F-FDG PET: histologic and immunohistochemical tissue analysis. J Nucl Med 2001;42:9—16.

[2] Daisne JF, Sibomana M, Bol A, et al. Evaluation of a multimodality image (CT, MRI and PET) coregistration procedure on phantom and head and neck cancer patients: accuracy, reproducibility and consistency. Radiother Oncol 2003;69:237—45.

[3] Eschmann SM, Paulsen F, Reimold M, et al. Prognostic impact of hypoxia imaging with 18F-misonidazole PET in non-small cell lung cancer and head and neck cancer before radiotherapy. J Nucl Med 2005;46:253—60.

[4] Fyles A, Milosevic M, Hedley D, et al. Tumor hypoxia has independent predictor impact only in patients with node-negative cervix cancer. J Clin Oncol 2002;20:680—7.

[5] Hicks RJ, Kalff V, MacManus MP, et al. 18F-FDG PET provides high-impact and powerful prognostic stratification in staging newly diagnosed non-small cell lung cancer. J Nucl Med 2001;42:1596—604.

[6] Hicks RJ, Rischin D, Fisher R, Binns D, Scott AM, Peters LJ. Utility of FMISO PET in advanced head and neck cancer treated with chemoradiation incorporating a hypoxia-targeting chemotherapy agent. Eur J Nucl Med Mol Imag 2005;32:1384—91.

[7] Kubota K, Tada M, Yamada S, et al. Comparison of the distribution of fluorine-18 fluoromisonidazole, deoxyglucose and methionine in tumour tissue. Eur J Nucl Med 1999;26:750—7.

[8] Paudit N, Gonen M, Krug L, Larson SM. Prognostic value of [^{18}F]FDG-PET imaging in small cell lung cancer. Eur J Nucl Med Mol Imag 2003;30:78—84.

[9] Pugachev A, Ruan S, Carlin S, et al. Dependence of FDG uptake on tumour microenvironment. Int J Radiat Oncol Biol Phys 2005;62:545—53.

[10] Rajendran JG, Mankoff DA, O'Sullivan F, et al. Hypoxia and glucose metabolism in malignant tumors: evaluation by [18F]fluoromisonidazole and [18F]fluorodeoxyglucose positron emission tomography imaging. Clin Cancer Res 2004;10:2245—52.

[11] Rajendran JG, Wilson DC, Conrad EU, et al. [18F]FMISO and [18F]FDG PET imaging in soft tissue sarcomas: correlation of hypoxia, metabolism and VEGF expression. Eur J Nucl Med Mol Imag 2003;30:695—704.

[12] Rasey JS, Koh WJ, Evans ML, et al. Quantifying regional hypoxia in human tumors with positron emission tomography of [F-18]fluoromisonidazole. Int J Radiat Oncol Biol Phys 1996;36:417—28.

[13] Sørensen M, Horsman MR, Cumming P, Munk OL, Keiding S. Effect of intratumoural heterogeneity in oxygenation status on FMISO PET, autoradiography, and electrode Po_2 measurements in murine tumours. Int J Radiat Oncol Biol Phys 2005;62:854—61.

[14] Thorwarth D, Eschmann SM, Scheiderbauer J, Paulsen F, Alber M. Kinetic analysis of dynamic [^{18}F]fluoromisonidazole pet correlates with radiation treatment outcome in head-and-neck cancer. BMC Caner 2005;5:152.

[15] Viola P, Wells WM. Alignment by Maximization of Mutual Information. Int J Comp Vision 1997;24:137—54.

Appendix D

A model of reoxygenation dynamics of head and neck tumors based on serial FMISO-PET investigations

accepted for publication in the
International Journal of Radiation Oncology, Biology and Physics

A model of reoxygenation dynamics of head and neck tumors based on serial [^{18}F]-FMISO PET investigations

Daniela Thorwarth*[1] , Susanne-Martina Eschmann[2] , Frank Paulsen[3] and Markus Alber[1]

[1]Section for Biomedical Physics, Clinic for Radiation Oncology, University Hospital Tübingen, Germany
[2]Department of Nuclear Medicine, Radiological Clinic, University Hospital Tübingen, Germany
[3]Department of Radiation Therapy, Clinic for Radiation Oncology, University Hospital Tübingen, Germany

Email: DT*: daniela.thorwarth@med.uni-tuebingen.de; SME: susanne-martina.eschmann@med.uni-tuebingen.de; FP: frank.paulsen@med.uni-tuebingen.de; MA: markus.alber@med.uni-tuebingen.de;

*Corresponding author

Abstract

Purpose: To develop a model for reoxygenation dynamics and its relation to local control after radiotherapy (RT) based on repeated dynamic FMISO PET examinations in head-and-neck cancer (HNC) patients.

Methods and Materials: 10 HNC patients were examined with dynamic FMISO PET before RT with 70Gy and after approximately 20Gy. Two of these patients had two additional dynamic FMISO scans during treatment. Local recurrence was assessed by CT-based follow-up 8-24 months after RT. Tumor specific values for the level of FMISO retention R and the vascular perfusion efficiency P were determined using a kinetic compartment model.

Results: Individual $R-P$ scattergrams before and during therapy were analyzed and significant therapy induced changes in the characteristic $R-P$ patterns were observed. A TCP model was derived that involves the tissue parameters R and P and estimates the time to reoxygenation. On the basis of this model, a malignancy value M was introduced and calibrated by a fit to the observed outcome data. Reoxygenation is reflected by the model as a progression to less malignant tumor types i.e. smaller values of M. In four out of six patients with severe hypoxia, $\bar{M}$ had decreased after 20Gy, whereas two patients showed increasing $\bar{M}$. Four patients showed no hypoxia in the pre-treatment scan.

Conclusion: A TCP model was developed based on repeated FMISO PET scans during RT. The model combines the local perfusion efficiency and the degree of hypoxia to estimate the reoxygenation time. It constitutes a key for hypoxia image guided dose escalation in RT.

Key Words: Hypoxia, FMISO PET, TCP, Reoxygenation, Radiotherapy.

1 Introduction

Hypoxia assays of individual tumors are increasingly becoming accessible [1–7], while hypoxia-targeted therapies are proven to be efficient for increased local control and overall survival [8–10]. Given the long standing tenet of hypoxia induced radioresistance of the target cells, it comes naturally to direct a dose increment at the volumes which appear positive in hypoxia imaging. The obvious question remains how image intensity translates into dose escalation [11–14].

Assuming that the hypoxic cell population exhibits a decrease of radiosensitivity by a factor $2.5-3$ [15], it is immediately clear that this cannot be compensated for by dose escalation unless this cell population is rapidly reduced by reoxygenation. Thus, the most relevant quantity for hypoxia image guided dose escalation (HIDE) is the time from the onset of radiotherapy to reoxygenation, which is equivalent to the number of treatment fractions lost on the radioresistant cells. At first sight, this suggests that a single pre-treatment hypoxia image cannot suffice to determine the required extent of dose escalation.

The presence of regions in a tumor where cells can suffer from a lack of oxygen supply is a symptom of an insufficient or deficient vasculature. Hence, despite the complicated processes that occur during normal growth or under therapy, like repopulation, redistribution between cell compartments, and loss of cells either by starvation or as a consequence of therapy, the central question for HIDE is: When does the vasculature become sufficient again, either by neovascularisation or reduced consumption, or both? Animal experiments show that the phenomenon of hypoxia is an inherent property of cell lines [16] and can outlast the lifespan of hypoxic cells by far [17]. The emergence of hypoxia seems to be engrained in the growth characteristics of a clonogen population.

If functional imaging reveals the irregularity and coarseness of the tumor vasculature, it may be possible to estimate the time to reoxygenation. In dynamic studies of PET tracer or MR/CT contrast agent uptake, it is possible to obtain a measure of the efficiency of perfusion (determined by the number, caliber and distribution of blood vessels and the magnitude of blood flow within them) during the influx phase shortly after injection. The degree of hypoxia as given by the uptake of PET tracer is in itself an indicator of the coarseness of the vasculature, as hypoxia can only persist in wide pouches between perfused blood vessels. The combination of both, perfusion efficiency and hypoxia labeling, has been shown to carry significant information about the success of chemo-radiotherapy [18].

In the following, we develop a model for tumor control that predicts in essence the time to reoxygenation from measurements of perfusion efficiency and hypoxia with the PET tracer [^{18}F]-FMISO. The model was inspired by a series of repeated PET scans of a number of head and neck patients undergoing chemo-radiotherapy, giving some insight into the changes of both perfusion efficiency and hypoxia. All dynamic PET scans were evaluated with a kinetic compartment model introduced in [19].

2 Methods and Materials

2.1 Patients

The total size of the study was 15 patients, details about patient and tumor characteristics can be found in [18]. Each of these patients was examined with FDG and dynamic FMISO PET before the start of treatment. A subgroup of 10 patients received repeat scans after approximately 2 weeks of treatment ($\approx$ 20 Gy). Patients were treated with radio-chemotherapy of 70 Gy applied in 35 fractions (fx). Therapy outcome data were available for all patients. After the end of therapy, patients were reviewed regularly every three months with clinical examination, flexible endoscopy and computed tomography (CT) when recurrent disease was suspected. Routine CT scans were also acquired six weeks and one year after therapy was finished.

For a total of eight patients (#1-4, 7, 9, 10 and 14), one FMISO repeat scan is available, whereas for two patients (#6 and 13), three repeat scans could be acquired. Patient 6 had follow-up scans after 20, 50 and 70 Gy, patient 13 after 10, 20 and 50 Gy. The secondary FMISO PET scans were also acquired using a dynamic acquisition mode. The scans were performed as explained in [18]. The long acquisition times made it difficult to organize the trial and put a large burden on the patients who were suffering from acute reactions during therapy.

The repeat scans were analyzed with the same kinetic model as the pre-treatment scans and scatter plots as shown below were calculated based on the results of the compartmental analysis [19]. The volumes taken into account for the analysis of the repeat scans were defined by the FDG PET positive

areas of the tumors before the start of treatment. Notice that the tumor size cannot be assessed on a FMISO image.

2.2 Tumor Control Model

Naturally, given the population-averaged experimental data, the best a tumor control model including reoxygenation can do is to describe the observations. No attempt at a mechanistic model is made, and all parameters are understood as averages over the patient population.

We start with the common Poisson approximation of TCP

$$-\ln \mathrm{TCP} = \rho \sum_{i=1}^{n} \exp(-\alpha_0 D_i) \quad , \tag{1}$$

where ρ is the mean cell density per volume element, α_0 is the mean cell sensitivity, D_i is the dose in volume element i and the sum runs over all volume elements $i = 1, ..., n$. The rhs is equal to the expected value of surviving cells in the total tumor volume, henceforth denoted with μ_0. If $\mu_i = \rho \exp(-\alpha_0 D_i)$ is the expected value of surviving cells per volume element, we obtain

$$\mu_0 = \sum_{i=1}^{n} \mu_i \quad . \tag{2}$$

Assume now that the cells of a given tumor volume element are labeled according to their distance s to the nearest perfused blood vessel. Next, the cells are sorted according to their distance label and collected into bins. Let $\rho \cdot h(s)$ be the number of cells in the bin of width Δs and mean distance to the next vessel s. Clearly, the number of cells will decrease as the mean distance to the next vessel increases: $h(s) \to 0$, as $s \to \infty$.

In order to take into account hypoxia induced radio-resistance, we assume that each bin has a specific mean cell sensitivity $\alpha(s)$ and reoxygenates after a fraction $t_R(s)$ of the total number of treatment fractions. Therefore

$$\begin{aligned} \mu_i &= \rho \int_0^\infty ds\ h(s) \cdot \\ &\quad \exp\left(D_i\left(-\alpha(s) t_R(s) - \alpha_0(1 - t_R(s))\right)\right) \\ &= \rho \exp(-\alpha_0 D_i) \cdot \\ &\quad \int_0^\infty ds \exp\left(-(\alpha(s) - \alpha_0) t_R(s) D_i + \ln h(s)\right). \end{aligned} \tag{3}$$

The integral is the excess of cells surviving the treatment because of reduced cell sensitivity. In case no hypoxia is present, the integral is 1. If there is some hypoxia present, the integral becomes rapidly dominated by the bins where a large number of cells are initially hypoxic and suffer delayed reoxygenation. Assume that these bins are centered around a distance s_0. In keeping with the well established saddle-point approximation (i.e. in the limit $D_i \to \infty$), we write

$$\begin{aligned} &\int_0^\infty ds \exp\left(-(\alpha(s) - \alpha_0) t_R(s) D_i + \ln h(s)\right) \\ &\qquad = \sqrt{\frac{2\pi h^2(s_0)}{|f''(s_0)| D_i}} \exp(-(\alpha_h - \alpha_0) t_R D_i) \end{aligned} \tag{4}$$

where $\alpha_h = \alpha(s_0)$ and $t_R = t_R(s_0)$ are the macroscopically observable quantities of cell sensitivity and reoxygenation time for this volume element. The term $(2\pi h^2(s_0)/(|f''(s_0)|D_i))^{1/2}$ has a constant value, $f(s)$ is given by $f(s) = (\alpha(s) - \alpha_0) t_R(s)$. In the following, this normalization constant will be neglected, as it can be absorbed in the fit constant A of the final model (eq. (7)). The rhs is termed the *malignancy value* M_i of this volume element. The here introduced malignancy value is purely related to hypoxia and consequential treatment resistance. It does not relate to the potential of a tumor to develop metastases.

The kinetic analysis of FMISO uptake delivers for each volume element a measure of perfusion efficiency P and of tracer retention R. In [18] it was shown that the distributions of (R, P) are quite characteristic for each tumor, with an indication that the presence of high-R – low-P volume elements is an unfavorable indicator for treatment response. Here, we assume

1. the macroscopic cell sensitivity α_h is proportional to the tracer retention R and
2. the macroscopic time to reoxygenation t_R is proportional to $1/(P + P_0)$, suggesting that there exists a maximum time $1/P_0$ after which any volume element will have reoxygenated.

The results corroborate this choice.

Finally, we obtain

$$M_i = \exp(bR_i/(P_i + P_0)) \tag{5}$$

where the dose D_i to the volume element i is implicit in the parameter $b = \tilde{b} \cdot D_i/D$. Assuming that

$D_i = D$ everywhere, the final expression for the total number of surviving cells reads

$$\mu_0 = \rho \exp(-\alpha_0 D) \sum_{i=1}^{n} M_i \quad . \tag{6}$$

The parameters $A = \rho \exp(-\alpha_0 D)$, b and P_0 were determined by a maximum log-likelihood fit of $\exp -\mu_0$ to the group of 15 patients, as shown in [18].

3 Results

The distributions of tracer retention - perfusion efficiency for each patient can be classified as one of three typical scatter patterns. The classical hypoxic tumor shows high tracer retention and lower than average perfusion efficiency values, see figure 1(a). Here, a deficient vasculature creates pockets of severe hypoxia, which may even contain necrotic cells which are not visible on FMISO images. A second class of tumors shows significant tracer retention and more than average perfusion efficiency values, see figure 1(b). These tumors do have a viable vasculature, but oxygen consumption is so high that the supply is not sufficient. These tumors may be more amenable to hypoxia-modifying treatments and may show faster reoxygenation than the first type. Finally, tumors of the third class show no tracer retention, while their perfusion efficiency values are normal to greater than average, see figure 1(c). In [18] it was shown that the prognosis for type 1 is very poor, for type 2 intermediate, but very good for type 3.

The observed correlation between the two-dimensional distributions of tracer retention and perfusion efficiency corroborates assumptions 1 and 2 made in the methods section. As high levels of tracer retention indicate an unfavorable prognosis, this parameter was assumed to be proportional to the sensitivity parameter α_h (assumption 1). Secondly, the fact that very poor outcome could be associated with patients presenting in addition with badly perfused tumors indicates an inverse correlation of perfusion efficiency and the time until reoxygenation occurs (assumption 2).

The fast response of a tumor to radiotherapy could be dominated by two effects. Firstly, due to a deceleration of proliferation, the oxygen consumption drops and as a consequence, perfusion limited hypoxia vanishes. Secondly, due to an acute inflammatory reaction, the blood flow increases which increases oxygen supply with the same result as above. This turns out to be the reoxygenation pattern of type 2 tumors. Of the 6 patients classified as type 2, only 3 had noticeable traces of hypoxia left at 20 Gy, while the perfusion was generally enhanced.

At later times during treatment, the reoxygenation response could be shaped by an overall shrinkage of tumor mass and neovascularisation, two effects that can enhance the quality of the vasculature, while it is certainly also damaged by radiation. The net effect is somewhat elusive on the basis of current knowledge. For this reason, type 1 tumors are more interesting study objects. Figure 2 shows the scatter patterns of patient 6 before treatment (a), at 20 Gy (b) and at 50 Gy (c). The early response leads to increased perfusion efficiency, but the overall reduction of tracer retention is rather small. The 20 Gy scatter pattern resembles a type 2 tumor. At 50 Gy, hypoxia has almost vanished, resulting in a type 2-3 scatter pattern.

The example of this patient suggests the hypothesis that the footprint of reoxygenation in the scatter patterns is a progression to less malignant types. In other words, the malignancy value determined on the basis of dynamic FMISO PET decreases during radiotherapy. The aforementioned and additional unknown mechanisms of reoxygenation and redistribution may in effect increase perfusion efficiency and reduce tracer retention and thus propagate a volume element in the scatter plot from the lower right to the upper left. This propagation would move a volume element from a region of high malignancy to lesser malignancy. Hence, the lines of equal malignancy would run orthogonal to the direction of propagation, i.e. from the lower left to the upper right.

This is in fact what the above TCP model tries to capture. From eq. (5), the lines of constant malignancy have the form

$$P = \frac{bR}{\ln M} - P_0 \quad . \tag{7}$$

The model was chosen such that it produces the simplest possible form of iso-malignancy lines that still describes the observations. The directions of progression to lower malignancy obtain as

$$\nabla M = \frac{bM}{P + P_0} \begin{pmatrix} -1 \\ \frac{R}{P+P_0} \end{pmatrix} \quad . \tag{8}$$

Figure 3 shows the iso-malignancy lines and the directions of progression for the example patient of figure 2.

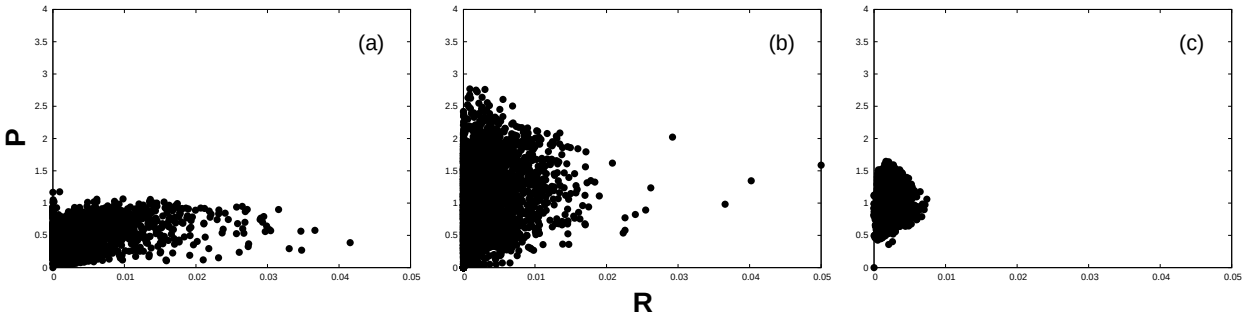

Figure 1: Scattergrams of tracer retention R versus perfusion efficiency P for patients #6 (a), #1 (b) and #8 before the start of RT.

The parameters of the model were obtained from a maximum likelihood fit to the initial set of 15 patients. The following parameter values were determined from the fit: $A = 9.92 \cdot 10^{-5}, b = 208.0$ and $P_0 = 0.704$. For each patient, a TCP value was computed. The patients were grouped according to the expected number of surviving cells μ_0 into four groups. The observed rate of local control is compared with the predicted TCP value of the model in figure 4.

The ratio of $\bar{M}$ before the start of treatment ($\bar{M}_0$) and after 10 fractions ($\bar{M}_{10}$) represents the factor by which the expected value of surviving cells is increased due to hypoxia. For the analysis of the mean malignancy $\bar{M}$, only patients were taken into account that presented $\bar{M}_0 \geq 1.69$. This cutoff value corresponds to a reoxygenation time of two days, which is assumed to be the magnitude of the associated errors. Four of the ten patients presented $\bar{M}_0$-values below this cutoff (# 1, 7, 10 and 13), whereas the mean malignancy values for the remaining six patients are shown in table 1. These results support in four cases (# 3, 4, 6 and 14) the hypothesis of a progression to less malignant tumors during irradiation. The small increase in malignancy observed for patient # 9 is probably due to errors emerging from the data analysis. In contrast, the high $\bar{M}$-value determined for the follow-up data of patient # 2 represents an outlier, that may be caused by too sparse dynamic FMISO PET data. For this patient, dynamic data were acquired only during a period of 10 min. This is in general too short to image the important regions of the FMISO uptake curves accurately.

4 Discussion

The present development sees hypoxia and reoxygenation essentially as a consequence of a deficient vasculature and its response to radiation. While hypoxia constitutes a severe problem in radiotherapy for a variety of reasons [20], it stems from a

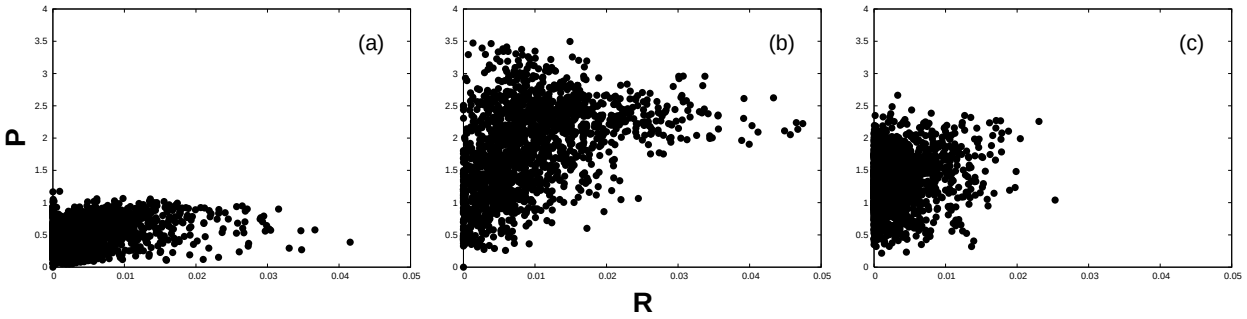

Figure 2: Scatter patterns for patient 6 (a) before treatment, (b) at 20 Gy and (c) at 50 Gy.

deeper cause. The model tries to capture the observable patterns of hypoxia and reoxygenation, both of which are linked to the irregularity of vascularization.

The presented model assumes that the parameter tracer retention is proportional to the cell sensitivity α_h. A second assumption inversely relates the perfusion efficiency with the time until reoxygenation occurs. The observable patterns of reoxygenation in the repeated scans, as shown in figure 2 justify these assumptions. Also the facts that the developed TCP model fits the patient outcome data very well and that the values of M shrink for most of the patients after the first two weeks of therapy support assumptions 1 and 2.

The processes occurring as response to therapy in an individual tumor are many and varied. Histological studies suggest, that any imaginable effect can indeed be found in some specimen [16, 17, 21]. Naturally, a population based TCP model can only describe the net effect of all possible scenarios of hypoxia/reoxygenation on local control. Within the limitations of the study size, this seems to be possible with a single pre-treatment hypoxia image.

The reason for this may be that on average, both the initial degree of hypoxia and the speed of reoxygenation are linked to the irregularity of the vasculature. The patchiness of the intervascular spaces defines the regions where hypoxia can occur. Redistribution of cells between compartments or even a constant loss of the most hypoxic cells do not change anything about the number of cells that are located

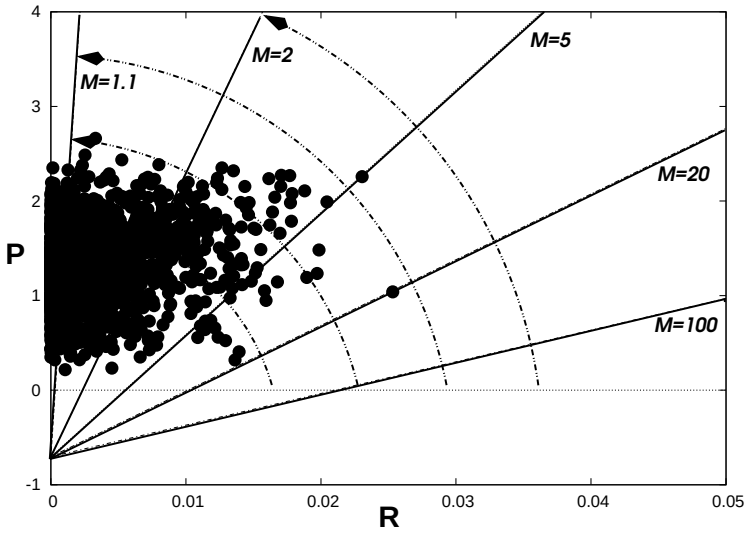

Figure 3: Isolines for different malignancy values M and directions of progression to lower Malignancy for patient #6.

Pat #	M_0	M_{10}
2	35.3	15810
3	17.1	1.16
4	143.1	71.0
6	8.39	2.56
9	1.80	4.56
14	6.02	1.61

Table 1: Mean malignancy values $\bar{M}$ before the start of treatment and after 10 fractions for all patients with $\bar{M}_0 \leq 1.69$.

in a hypoxia-prone region at any given time. Only slower processes like neovascularisation or shrinkage of the tumor can change the overall constitution of the vasculature.

In this image, the concepts of acute and chronic hypoxia seem to lose meaning in the context of clinical treatments. Clearly, both are signs of a less than sufficient vasculature, so the likelihood of coincidence is high, especially given the rather large dimensions of PET image voxels. For a model that averages over the total treatment time and a population of patients, all that matters is the mean size of the hypoxic pouches created by the patchy vascularization. The more relevant distinction here is whether this quantity diminishes quickly due to fast reoxygenation, driven by increased supply and reduced consumption of oxygen, or whether reoxygenation occurs by slow processes.

The speed of reoxygenation also impacts the strategy of dose escalation that could be adopted to overcome hypoxia induced radioresistance, and the consequential reduction of cell kill. If dose escalation was applied from the beginning of treatment, a lot of the additional dose administered to the hypoxic region could be wasted on resistant cells if reoxygenation was slow. It could be better to wait with escalation until reoxygenation has occurred and make up for the loss of cell kill towards the end of the treatment, when the dose is more efficient. This strategy runs the risk that reoxygenation may come too late and the dose per fraction becomes too high.

The model affords predictions about the required dose escalation per volume element. If the strategy of a late boost after reoxygenation is to be adopted, we require for the additional dose ΔD

$$M_i \exp(-\alpha_0 \Delta D) = 1 \tag{9}$$

which leads to

$$\frac{\Delta D + D_0}{D_0} = \frac{\ln M_i}{\alpha_0 D_0} + 1 \tag{10}$$

where D_0 is the base treatment dose, in our case 70 Gy, and the cell sensitivity of non-hypoxic tumors α_0 equals, say, 0.4. This strategy assumes that the image of initial hypoxia is frozen in the distribution of remaining cells half way into the treatment.

In contrast, a homogeneous boost has to overcome the mean cell sensitivity $\bar{\alpha}$

$$M_i \exp(-\alpha_0 D_0) = \exp(-\bar{\alpha} D_0) \tag{11}$$

so that if we require that

$$\bar{\alpha}(\Delta D + D_0) = \alpha_0 D_0 \tag{12}$$

it obtains

$$\frac{\Delta D + D_0}{D_0} = \frac{\alpha_0 D_0}{\alpha_0 D_0 - \ln M_i} \quad . \tag{13}$$

This strategy assumes that the reoxygenation is not accelerated by the hypofractionation. Both strategies do not take into account the additional effect of greater fraction sizes as it is felt that this is of secondary importance given the individual uncertainties of hypoxia images and their interpretation. By means of a Taylor expansion of eq. (13) for $\ln M_i \geq 0$ small, it can be seen easily that both factors agree

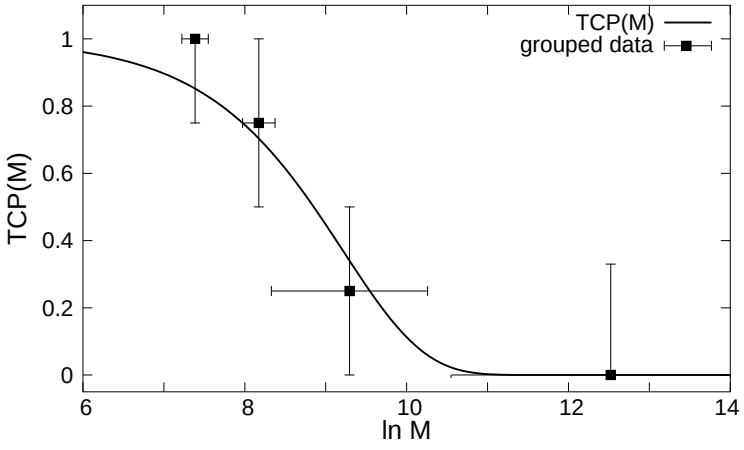

Figure 4: TCP model fitted to the patient outcome data.

for small dose escalations. For large dose escalations, the first factor becomes noticeably smaller than the second. The observed range of required dose escalation factors in the present population according to eq. (13) was between 1 and 1.66.

Some authors have reported model studies about the efficiency of hypoxia dose escalation when there was a risk of misguiding it due to fluctuations of acute hypoxia or image errors [22]. It was found that by far the greatest mishap is missing persistent, i.e. chronic hypoxia. One may take the liberty to reword this finding: if one misses slowly reoxygenating areas. The present model makes dose escalation predictions on the basis of population averaged reoxygenation dynamics. Individual patients can deviate from these predictions. As usual, a greater amount of individual information affords a more efficient treatment. Hence, sequential hypoxia images during radiotherapy can be particularly valuable for patients where the pre-treatment scan predicted slow reoxygenation and consequentially high dose escalation factors.

5 Conclusion

A phenomenological tumor control model including a prediction of reoxygenation speed was presented and validated with observations of local control in head and neck patients after chemo-radiotherapy. The essential image information was gleaned from dynamic FMISO PET scans which provide two individual pieces of information, the perfusion efficiency as seen in the early phase of tracer influx, and late tracer retention. Both quantities relate to the sufficiency and patchiness of the tumor vasculature. The observation of reoxygenation dynamics in this patient population suggests that hypoxia image guided dose escalation is in fact driven by the degree of irregularity of the vasculature.

Acknowledgments

This project was financially supported by the German Research Foundation (DFG), grant no. AL 877/1. The authors would like to thank Prof H-J Machulla and his team (Radiopharmacy Department, University Hospital Tübingen) for excellent PET tracer production.

References

1. Eschmann SM, Paulsen F, Reimold M et al. Prognostic impact of hypoxia imaging with 18F-misonidazole PET in non-small cell lung cancer and head and neck cancer before radiotherapy. J Nucl Med 2005; 46(2): 253-260.

2. Hicks RJ, Rischin D, Fisher R, Binns D, Scott AM, Peters LJ. Utility of FMISO PET in advanced head and neck cancer treated with chemoradiation incorporating a hypoxia-targeting chemotherapy agent. Eur J Nucl Med Mol Imaging 2005; 32(12): 1384-1391.

3. Rasey JS, Koh WJ, Evans ML et al. Quantifying regional hypoxia in human tumors with positron emission tomography of [F-18]fluoromisonidazole. Int J Radiat Oncol Biol Phys 1996; 36: 417-428.

4. Piert M, Machulla HJ, Picchio M et al. Hypoxia-Specific Tumor Imaging with ^{18}F-Fluoroazomycin Arabinoside. J Nucl Med 2005; 46: 106-113.

5. Dehdashti D, Grigsby PW, Aintun MA, Lewis JS, Siegel BA, Welch M. Assessing tumor hypoxia in cervical cancer by positron emission tomography with ^{60}Cu-ATSM: Relationship to therapeutic response - a preliminary report. Int J Radiat Oncol Biol Phys 2003; 55(5): 1233-1238.

6. Nordsmark M, Overgaard J. A confirmatory prognostic study on oxygenation status and loco-regional control in advanced head and neck squamous cell carcinoma treated by radiation therapy. Radiother Oncol 2000; 57; 39-43.

7. Nordsmark M, Overgaard M, Overgaard J. Pretreatment oxygenation predicts radiation response in advanced squamous cell carcinoma of the head and neck. Radiother Oncol 1996; 41: 31-39.

8. Kaanders JHAM, Bussink J, van der Kogel A. ARCON: a novel biology-based approach in radiotherapy. Lancet Oncol 2002; 3: 728-737.

9. Rischin D, Hicks RJ, Fisher R, et al. Prognostic significance of [18F]-misonidazole positron emission tomography-detected tumor hypoxia in patients with advanced head and neck cancer randomly assigned to chemoradiation with or without tirapazamine: a substudy of Trans-Tasman

Radiation Oncology Group Study 98.02. J Clin Oncol 2006; 24(13): 2098-2104.

10. Overgaard J, Eriksen JG, Nordsmark M, et al. Plasma osteopontin, hypoxia, and response to the hypoxia sensitiser nimorazole in radiotherapy of head and neck cancer: results from the DAHANCA 5 randomised double-blind placebo-controlled trial. Lancet Oncol 2005; 6(10): 757-764.

11. Alber M, Paulsen F, Eschmann SM, Machulla HJ. On biologically conformal boost dose optimization. Phys Med Biol 2003; 48(2): N31-35.

12. Chao KS, Bosch WR, Mutic S et al. A novel approach to overcome hypoxic tumor resistance: Cu-ATSM-guided intensity-modulated radiation therapy. Int J Radiat Oncol Biol Phys 2001; 49(4): 1171-1182.

13. Bentzen SM. Theragnostic imaging for radiation oncology: dose-painting by numbers. Lancet Oncol 2005; 6(2): 112-117.

14. Ling CC, Humm J, Larson S et al. Towards multidimensional radiotherapy (MD-CRT): biological imaging and biological conformality. Int J Radiat Oncol Biol Phys 2000; 47(3): 551-560.

15. Gray LH, Conger AD, Ebert M, et al. The concentration of oxygen dissolved in tissues at the time of irradiation as a factor in radiotherapy. Br J Radiology 1953; 26: 638-648.

16. Ljungkvist ASE, Bussink J, Rijken PFJW, et al. Vascular architecture, hypoxia, and proliferation in first-generation xenografts of human head-and-neck squamous cell carcinomas. Int J Radiat Oncol Biol Phys 2002; 54(1): 215-228.

17. Ljungkvist ASE, Bussink J, Kaanders JHAM, et al. Hypoxic cell turnover in different solid tumor lines. Int J Radiat Oncol Biol Phys 2005; 62(4): 1157-1168.

18. Thorwarth D, Eschmann SM, Scheiderbauer J, Paulsen F, Alber M. Kinetic analysis of dynamic 18F-fluoromisonidazole PET correlates with radiation treatment outcome in head-and-neck cancer. BMC Cancer 2005; 5: 152.

19. Thorwarth D, Eschmann SM, Paulsen F, Alber M. A kinetic model for dynamic [^{18}F]-Fmiso PET data to analyse tumor hypoxia. Phys Med Biol 2005; 50: 2209-2224.

20. Coleman CN, Mitchell JB, Camphausen K. Tumor Hypoxia: Chicken, Egg, or a Piece of the Farm? (editorial) J Clin Oncol 2002; 20: 610-615.

21. Ljungkvist ASE, Bussink J, Kaanders JHAM, et al. Dynamics of Hypoxia, Proliferation and Apoptosis after Irradiation in a Murine Tumor Model. Radiat Res 2006; 165: 326–336.

22. Popple RA, Ove R, Shen S. Tumor control probability for selective boosting of hypoxic subvolumes, including the effect of reoxygenation. Int J Radiat Oncol Biol Phys 2002; 54(3): 921-927.

Appendix E

Hypoxia Dose Painting by Numbers: A Planning Study

accepted for publication in the
International Journal of Radiation Oncology, Biology and Physics

Hypoxia Dose Painting by Numbers: A Planning Study

Daniela Thorwarth*[1] , Susanne-Martina Eschmann[2] , Frank Paulsen[3] and Markus Alber[1]

[1]Section for Biomedical Physics, Clinic for Radiation Oncology, University Hospital Tübingen, Germany
[2]Department of Nuclear Medicine, Radiological Clinic, University Hospital Tübingen, Germany
[3]Department of Radiation Therapy, Clinic for Radiation Oncology, University Hospital Tübingen, Germany

Email: DT*: daniela.thorwarth@med.uni-tuebingen.de; SME: susanne-martina.eschmann@med.uni-tuebingen.de; FP: frank.paulsen@med.uni-tuebingen.de; MA: markus.alber@med.uni-tuebingen.de;

*Corresponding author

Abstract

Purpose: The feasibility of different hypoxia dose painting strategies in head-and-neck radiotherapy was investigated. The potential benefit was limited by the stipulation of isotoxicity with respect to the conventional IMRT treatment.

Methods: 13 HNC patients were included into the planning study. For each patient, three different treatment plans were created: A conventional IMRT plan, an additional uniform dose escalation (uniDE) of 10% to the FDG-positive volume, and a plan where dose painting by numbers (DPBN) was implemented. DPBN was realized according to a map of dose escalation factors calculated from dynamic FMISO PET data.

Results: Both DE approaches were shown to be feasible under the constraint of limiting normal tissue doses to the level of conventional IMRT. For DPBN, the prescriptions could be fulfilled in larger regions of the target than for uniDE. FDG-positive volumes had sizes up to 94 ccm. In contrast, regions receiving comparable dose levels with DPBN presented volumes in the range of $0 - 2.7$ ccm. Overtreatment of the target was observed with uniDE in most of the cases while some regions did not receive the required dose to overcome hypoxia-induced radiation insensitivity. TCP increased from 55.9% with conventional IMRT to 57.7% for the uniDE method in the patient group. For DPBN, a potential increase in TCP from 55.9 to 70.2% was determined. Therefore, DPBN seems to result in higher benefits for the patients.

Conclusion: DPBN delivers the dose more effectively than an additional uniform boost to the FDG positive area. If hypoxia could be adequately quantified using a simple imaging technique like FMISO PET, DPBN in HNC could substantially increase tumor control.

Key Words: Dose painting, dose painting by numbers, FMISO, hypoxia, planning study.

1 Introduction

The aim of dose painting (DP) in radiotherapy (RT) is to reach biological instead of physical conformity of the radiation dose delivery to the tumor. The basic idea of DP was first suggested by Ling *et al.* [1], who proposed applying a nonuniform dose prescription according to the functional characteristics of the tumor as assessed by biological imaging.

Positron emission tomography (PET) is a powerful technique for noninvasive biological imaging. It can be used for assessing regions of enhanced glucose metabolism with [^{18}F]-fluorodeoxyglucose (FDG) [2, 3] as well as for imaging proliferation, where [^{18}F]-fluorothymidine (FLT) is preferentially used [4]. In order to visualize hypoxic regions of a tumor, a variety of different PET tracers, such as [^{18}F]-fluoromisonidazole (FMISO) [5–7], [^{18}F]-fluoroazomycin (FAZA) [8] or [^{60}Cu]-ATSM [9], is available. Each of them is of potential use for radiotherapy (RT) planning purposes [10, 11].

Chao *et al.* [12] showed the feasibility of the DP concept by the example of a head-and-neck cancer (HNC) patient. A Cu-ATSM PET scan was used to identify a hypoxic subvolume in the tumor by thresholding. The prescription of 80 Gy to this Cu-ATSM positive biological target volume (BTV) was chosen arbitrarily.

In contrast, Alber *et al.* [13] and Bentzen *et al.* [14] proposed to perform *dose painting by numbers* (DPBN): to deliver spatially variant doses according to the specific functional requirements of the tissue. The feasibility of incorporating functional imaging data into an optimization algorithm for intensity modulated radiotherapy (IMRT) in order to produce spatially varying dose distributions was shown by Alber *et al.* [13].

A correlation of hypoxia in HNC with unfavorable prognosis was determined by different investigators [15–18]. Moreover, hypoxia targeted therapies, such as ARCON, were shown to improve treatment outcome [19]. However, it remains unclear how to quantify hypoxia and thus it becomes difficult to accurately prescribe doses for DPBN in order to overcome hypoxia-induced therapy resistance.

Dose escalation (DE) to a tumor that was identified as hypoxic can be beneficial because of different aspects, concerning malignancy and radiosensitivity of the clonogenes. Hence, a DP concept can be based on different hypotheses. The presence of hypoxia indicates a more malignant phenotype of tumor which may coincide with a number of unfavorable traits, e.g. enhanced proliferation. To counteract these mechanisms preemptively, a uniform dose escalation (uniDE) to the entire macroscopic tumor volume could be proposed. In order to identify this volume, FDG PET can be used. However, a major limitation of this approach might be the high dose levels applied uniformly to large volumes. In addition, there might be a risk of an unacceptably high probability of serious acute reactions due to the larger fraction sizes and higher overall normal tissue doses.

For these reasons, the idea of hypoxia DPBN that applies higher doses only where needed seems to be very promising from a clinical point of view. Applying spatially variant doses, according to the degree of hypoxia, might allow a significant reduction of the normal tissue burden and additionally reduce the overall treatment dose. On the other hand, some subvolumes may require a DE that is greater than that feasible for the entire GTV. Although a measurable amount of hypoxia is known to cause therapy resistance [15–18], in order to assign accurate dose prescriptions for DPBN on the basis of hypoxia PET, a clear relation between treatment outcome and the considered hypoxia imaging method is required. There is initial evidence, that dynamic FMISO PET results may correlate with clinical RT outcome [22]. We previously showed that FMISO data can be analyzed using a kinetic model [23], which allows for the determination of characteristic parameters related to the degree of hypoxia and blood vessel density. The key requirement for the translation of functional imaging data into clinically promising dose prescriptions is given by a tumor control probability (TCP) model based on these parameters and their relation to tumor reoxygenation [22]. Several TCP models incorporating different levels of radiosensitivity to account for tumor hypoxia were published by different investigators [24–26]. There, it was chosen to boost a tumor subvolume to a higher dose level in order to counteract the reduced sensitivity of hypoxic areas.

The present work investigates the feasibility of hypoxia DP in a patient population. Thus, a planning study with 13 HNC patients was performed, where for each patient three IMRT plans were created: a hypoxia DPBN plan according to a DE map determined from dynamic FMISO PET data, a uniDE to an FDG-based BTV, and a conventional IMRT plan. All of these plans were restricted to the same dose in the organs at risk (OARs) spinal cord, brain stem and parotid glands. The aim of of this study was to evaluate the feasibility of DE strategies with respect to target coverage at constant normal tissue toxicity. Additionally, a TCP analysis was carried out in order to determine whether the overall change in local control effected by the directed and the indiscriminate dose escalation would be sufficiently different to prove either one concept,

or both, of value. In the context of this work, the hypothesis was tested whether DPBN based on dynamic FMISO PET data can provide higher levels of tumor control than a uniDE to a FDG-based BTV.

2 Methods and Materials

2.1 Patients and Planning

The planning study was carried out for a total of 13 HNC patients. All patients were treated with primary radio-chemo-therapy to 70 Gy. Three of these patients were treated with IMRT in 35 fractions, 5 fractions a week with a daily dose of 2 Gy. The other 13 patients received conventional RT, 5 fractions with 2 Gy per week until 30 Gy. This first phase was followed by a hyperfractionation composed of a dose of 1.4 Gy applicated twice per day until the end of treatment. Therapy outcome data were available for all patients. After the end of therapy, patients were reviewed regularly every three months with clinical examination, flexible endoscopy and computed tomography (CT) when recurrent disease was suspected. Routine CT scans were also acquired six weeks and one year after therapy was finished.

For each of them, pre-treatment computed tomography (CT) as well as FDG and dynamic FMISO PET data were available. The FDG PET scan was taken 1 h after the injection of a total tracer activity of $\sim$ 400 MBq. For the FMISO PET, also $\sim$ 400 MBq of tracer activity were injected. The data were acquired in a dynamic mode from 0 to 4 h post injection (pi). All PET examinations were performed on a whole-body scanner (Advance, GE Medical Systems, Milwaukee, US) with an axial field of view (FOV) of 14.9 cm and a spatial resolution of $4 \times 4 \times 4.25$ mm^3.

For each patient, three individual IMRT plans were created with the planning system Hyperion: a conventional IMRT plan, a uniDE applied to the FDG PET positive biological target volume (BTV), and finally a plan where a DPBN approach according to dynamic FMISO PET data was realized. The dose calculation algorithm used by the planning system Hyperion is a finite size pencil beam with heterogeneity corrections [27]. For all three plans the same equivalent uniform dose (EUD) constraints for normal tissues were used. Hence, all final dose distributions had the same EUDs in the OARs. The advantage of this approach is that OARs were not compromised if the target goal was hard to achieve. Conversely, if the target dose could not be achieved, higher toxicity would have to be accepted. The OAR that were taken into account generally were the spinal cord, the spinal cord extended by a safety margin of 3 mm, the parotid glands and the non-specified normal tissue. The same beam angle settings were used for the three different plans of a patient. In general, 7 or 8 fields were used. Additionally, acute reactions were taken into account for the plan optimization: the weekly dose was limited to 12 Gy (2.4 Gy per fraction (Gy/fx)) for all three branches.

2.1.1 Conventional IMRT

In each case individual planning target volumes (PTVs) of first, second and third order (PTV70, PTV60 and PTV54 respectively) were defined. The nominal prescription doses were 70, 60 and 54 Gy. A simultaneous integrated boost (SIB) technique allowed us to apply 60/54 Gy during the first 30 fractions to the PTVs of second and third order. An additional boost of 10 Gy in 5 fractions was then given to the PTV70. This type of conventional IMRT plan corresponds to the clinically applied dose distribution.

2.1.2 Uniform Dose Escalation

A second set of plans was created in order to apply a uniformly escalated dose to the FDG positive subarea of the PTV70. The FDG PET image was therefore manually matched to the planning CT. The FDG-avid BTV was defined as the region in the PTV70 containing FDG intensities higher than 40% of the maximum value. No FDG PET data were available for patients # 9 and 10. In these cases, the FMISO scans taken 2 h pi were used to define a BTV as suggested by other investigators [7], defined as the region including tumor voxels with FMISO intensities larger than 40% of the maximum. A dose escalation of 10%, respectively 77 Gy, was prescribed to this area. For this branch, also 35 fractions were used, so that uniDE was applied with a SIB technique. The maximum dose per fraction was limited to 2.2 Gy/fx. The dose prescriptions for the PTVs and the normal tissue constraints were the same as for the conventional IMRT plans.

2.1.3 Hypoxia Dose Painting by Numbers

In order to perform hypoxia DPBN, a map of locally varying dose escalation factors (DEF) was determined on the basis of dynamic FMISO PET scans. The analysis of this data was performed using a compartmental model as previously described [23]. Briefly, a two-compartment model allows us to determine characteristic values for FMISO tracer retention and the density of perfused blood vessels on a voxel basis. A TCP model was developed, that assumes that the time needed for a reoxygenation of the tumor region is inversely proportional to the vascularization-perfusion parameter, which is related to the blood vessel architecture. Secondly, the model assumes a proportionality between local radioresistance of the tissue and the grade of tracer retention [22]. Hence,

$$\text{local cell survival } \sim \exp\left(\frac{b \cdot TR_i}{VP_i + c}\right) := M_i, \quad (1)$$

where TR_i and VP_i are the tracer retention and vascularization-perfusion parameter values for voxel i (of n). b and c are fit constants of the TCP model (for details, see [22]) defined by

$$\ln\,(\mathrm{TCP}) = \frac{\ln\,(\mathrm{TCP}_0)}{n} \cdot \sum_{i=1}^{n} M_i. \quad (2)$$

In the above equation, TCP_0 denotes TCP in the case of a non-hypoxic tissue, which is given by $-\ln(\mathrm{TCP}_0) = N \cdot \exp(-\alpha_0 D_0)$. Here, α_0 is the tumor cell sensitivity in Gy^{-1} and D_0 the required dose for a normoxic tumor tissue region in Gy and N the total number of clonogenes. In the context of this study, $D_0 = 70$ Gy was used. In general, the value of α_0 can vary between 0.2 and 0.5 Gy^{-1} for HNC. Here, α_0 was set to 0.4 Gy^{-1}, according to a SF_2 of 0.45 as reported in [28].

By this definition, M_i is the factor by which the expected number of cells at the end of therapy is increased due to hypoxia-induced radiation resistance. Assuming that the greater probability of cell survival can be compensated for by higher dose per fraction, the local dose escalation factor (DEF) for a given voxel i can be determined. Under the stipulation that the expected value of surviving cells should be constant and equivalent to $-\ln(\mathrm{TCP}_0)/n$ in all voxels, the DEF reads

$$\mathrm{DEF}_i = \frac{\alpha_0 D_0}{\alpha_0 D_0 - ln(M_i)} = \frac{\alpha_i}{\alpha_0}. \quad (3)$$

This local DEF compensates for the mean cell sensitivity $\langle \|\alpha_i\| \rangle_T < \alpha_0$ of a voxel during the whole treatment time. The resulting DE is applied throughout the whole treatment course, starting from the first day of treatment. It is assumed that reoxygenation occurs during the course of radiotherapy [29]. The velocity of reoxygenation of the tissue is assumed to be unaffected by the level of escalation of the radiation dose.

The resulting map of DEFs was used for a gradual dose prescription. By virtue of the model, the DEFs are truncated at 1: $\mathrm{DEF}_i \geq 1.0$. Furthermore, in this study the maximum dose per fraction was limited to 2.4 Gy, which equals $\mathrm{DEF}_i \leq 1.2$. In order to ensure accurate coregistration, the corresponding FMISO image acquired 2 h after tracer injection was manually matched to the planning CT. The resulting transformation matrix was then applied to the respective DEF map, which is available in the same coordinate system as the 2 h pi FMISO scan. The spatial resolution of the DE map was given by the PET voxel size of $4.0 \times 4.0 \times 4.25$ mm^3. For planning purposes, the voxel size was reduced using linear interpolation to the size of the CT planning grid, which was in all cases chosen to be $3 \times 3 \times 3$ mm^3.

2.2 Evaluation and Comparison of Treatment Plans

A statistical analysis of the DEFs associated to uniDE and DPBN was carried out. For DPBN, the mean DEF (DEF_{mean}) and the maximum DEF (DEF_{max}) were determined. Furthermore, the volume of the FDG-based BTV (V_{FDG}) was compared to the fractional tumor volumes associated with DEFs exceeding 1.05 ($\mathrm{V}_{1.05}$), 1.1 ($\mathrm{V}_{1.1}$) and 1.2 ($\mathrm{V}_{1.2}$) respectively. Additionally, the geographic localization (match/mis-match) of $\mathrm{V}_{1.05}$ and the FDG-based BTV were analyzed.

The three different treatment plans were compared based on dose volume histograms (DVHs). In order to evaluate the dose distributions in the target volumes, a comparison of characteristic DVH points is not possible as the DP prescriptions vary from one patient to another. Therefore, it was evaluated how well the applied doses matched the prescribed doses according to the effective DVH method of Alber *et al.* [13]. Cumulative histograms - similar to DVHs - were determined that show the fractional volume which receives at least a certain percentage of the

prescribed dose. To achieve this, the applied doses were weighted with the inverse of the local DEFs. This DVH transformation allows us to objectively compare the target coverage of treatment plans with different DE strategies.

Furthermore, TCP was calculated for different scenarios according to

$$-\ln(\mathrm{TCP}) = C \cdot \sum_{i=1}^{n} \exp(-\alpha_i D_i), \qquad (4)$$

where α_i is the local cell sensitivity in Gy^{-1}, D_i the dose in Gy applied to voxel i and n is the number of voxels. The constant $C = v \cdot n$ equals voxel volume v times number of cells per ccm n and was previously determined by a fit to a population of 15 patients [22]. Here, C was set to $6.3 \cdot 10^7$, according to the results presented in [22]. TCP was in all cases calculated for the GTV.

In a first step, the ideal TCP (TCP_{ideal}) was estimated assuming that the tumor cell sensitivity α was spatially variable and that the dose prescription can be achieved perfectly. This assumes the validity of the hypoxia TCP model [22]. To fulfill the dose requirements perfectly would imply a homogeneous cell survival probability and TCP would depend only on tumor volume.

In contrast, the second TCP scenario (TCP_{real}) took into account that prescriptions could not be achieved perfectly but the TCP model is correct. TCP_{real} was calculated using the realistic dose distributions obtained from the planning study. In general, TCP_{real} will be different from TCP_{ideal}. Usually TCP estimated for the realistic situation will be smaller unless inevitable hot spots counterbalance the effects of cold spots.

The third scenario evaluated the realistic dose distributions, but assumed a homogeneous tumour tissue, i.e. no deleterious influence of hypoxia. Here, $\alpha_i = \alpha_0$ was used everywhere so that the effect of a dose escalation in the absence of hypoxia was estimated in case FMISO and/or the TCP model do not provide relevant information for directed DE.

3 Results

The volumetric analysis for the two DE approaches, uniDE and DPBN, revealed a large bandwidth of volumes determined by the FDG positive area (V_{FDG}). V_{FDG} ranged from 7.32 to 94.34 cm^3, with a mean value of 37.79 cm^3. In most of the cases,

Pat	**PTV70**	$\mathbf{V_{FDG}}$		$\mathbf{V_{1.05}}$		$\mathbf{V_{1.1}}$		$\mathbf{V_{1.2}}$		geogr.
#	[ccm]	[ccm]	[%]	[ccm]	[%]	[ccm]	[%]	[ccm]	[%]	match
1	256.1	21.14	8.25	0	0	0	0	0	0	–
2	450.4	67.12	14.90	2.81	0.62	0.22	0.05	0	0	○
3	438.7	21.12	4.81	4.83	1.10	0.32	0.07	0	0	●
4	559.4	94.34	16.86	2.46	0.44	0.35	0.06	0.03	0.00	●
5	462.8	7.45	1.61	0.84	0.18	0.11	0.02	0.05	0.01	○
6	371.6	7.32	2.00	4.64	1.25	0.70	0.19	0	0	○
7	288.7	36.42	12.61	17.12	5.93	7.75	2.68	1.84	0.64	○
8	174.3	14.28	8.20	0.46	0.26	0	0	0	0	●
9	314.4	93.83*	29.84	25.68	8.17	6.70	2.13	1.22	0.39	○
10	208.1	20.44*	9.82	3.54	1.70	0.49	0.23	0	0	○
11	266.8	31.21	11.70	7.51	2.81	0.62	0.23	0	0	○
12	278.1	32.13	11.55	26.54	9.54	5.78	2.08	0.68	0.24	○
13	447.3	44.50	9.95	0.05	0.01	0	0	0	0	●

Table 1: Volumetric analysis for the different types of dose prescriptions: volume PTV70, volumes of the FDG-avid BTVs (V_{FDG}) and DPBN subvolumes associated to DEFs higher or equal 1.05 ($\mathrm{V}_{1.05}$), 1.1 ($\mathrm{V}_{1.1}$) or 1.2 ($\mathrm{V}_{1.2}$) respectively, according to the FMISO-based DE map. Relative values given in brackets are normalized to the total PTV70 volume. *No FDG scan was available for patients #9 and 10. The BTVs were defined on the basis of the FMISO PET acquired 2 h pi.
Right column: The geographic match/mismatch is analyzed for $\mathrm{V}_{1.05}$ and the FDG-avid volume. – no overlap, ○ partial overlap, ● $\mathrm{V}_{1.05}$ lies completely in the FDG-avid volume.

the tumor region that receives 2.2 Gy/fx would be too large to be clinically applicable. In addition, the geographic analysis showed that there may be large areas of mis-match between the FDG-avid volumes and the regions, where increased levels of hypoxia are observed. Hence, the escalated doses may miss the regions of decreased sensitivity. In contrast, the DPBN approach assigns doses in the order of 2.2 Gy/fx only to very small subvolumes of the tumor. In general, a DE of 10% was only observed for severely hypoxic areas, whereas regions of moderate hypoxia required DE factors lower than 1.1. Volumes that required DEFs greater than or equal to 1.1 ($V_{1.1}$) were in the range of 0 to 7.75 cm^3 (mean: 1.77 cm^3). In contrast, volumes that received additional doses of 5% or more ($V_{1.05}$) were between 0 and 26.54 cm^3, with a mean volume of 7.42 cm^3. Five of the 13 patients required DEFs greater than 1.2. The detailed volumetric analysis for all patients is summarized in table 1. The right column of table 1 shows the analysis of the geographic locations of $V_{1.05}$ and the FDG-avid volume.

The statistical analysis of the DEFs for DPBN revealed a large variation of the maximum DEFs (DEF_{max}) among the patients. DEF_{max} ranged from 1.03 to 1.66. The mean values in the FDG-positive BTVs of the individual DEFs (DEF_{mean}) were in the range $1.01 - 1.03$. Table 2 shows DEF_{max} and DEF_{mean} values for each patient in detail. DPBN escalates the dose for most of the patients by less and also in a smaller subvolume of the tumor. Hence, DPBN might constitute a more effective use of the radiation dose.

Figure 1 exemplarily shows the dose distributions of the three different plans for one patient (#12). For this patient, the dynamic FMISO data revealed large areas of severe hypoxia and low vascularization/perfusion. This is the reason why in small subareas of the PTV doses exceeding 82 Gy can be observed. The maximum DEF for this patient turned out to be 1.35. In contrast to other patients, the FDG positive area of this patient was quite irregular, which leads to a complicated prescription also in the case of uniDE. In the right column of figure 1 the corresponding DVHs are presented. The displayed DVHs for the OARs substantiate the isotoxicity achieved for the three different branches.

A detailed DVH comparison of normal tissue doses is not necessary, since the whole study was defined requiring isotoxicity of the three plans (see also fig. 1). A comparison of the overall treatment doses (expressed in total deposited energy) showed no significant increase of the integral dose neither for the uniDE approach nor for the DPBN plan. The total doses for both branches were in the order of $\pm 2\%$ relative to the conventional IMRT plan.

A comparison of the cumulative 'effective dose' histograms for the three plans of patient #12 is displayed in figure 2 for the PTV of first order. Compared to the conventional IMRT plan, the uniDE showed a non-negligible part of the PTV where the dose prescription could not be fully realized. Underdosages are mainly observed at the edges of the FDG-positive area, where the prescription rises from 70 to 77 Gy. In most cases, a lower target coverage was observed for the uniDE approach, but the requirement of DPBN was easier to fulfill. The target coverage of DPBN was only slightly worse than for the conventional IMRT plan. Nevertheless, if the DE maps become too heterogeneous, a precise application of the required dose might no longer be guaranteed. In table 3, a detailed list is given that summarizes for all patients and for each of the three treatment modalities the percentage of target volume that receives at least 95, 100 or 105% of the prescribed dose. The fact, that V_{95} is in most of the cases lower for DPBN than for conventional IMRT is due to the inhomogeneous DPBN prescriptions, which are difficult to reach exactly. The difficulty to achieve the uniDE prescription also becomes apparent in the greater hot spot volumes V_{105}.

Table 4 shows the detailed TCP analysis for the considered patient group. In the case of patient #2, TCP_{real} and TCP_0 were 0. This was caused by the proximity of the spinal cord to the PTV70. In this area, dose was reduced according to the normal tissue requirements. Therefore, also TCP decreased significantly.

The values for TCP_{ideal} revealed a substantial fraction of patients that is overtreated with uniDE. A large fraction of patients (e.g. #1, 5, 6, 8 and 10) already had TCP values of 0.8 and higher without DE. A uniDE would not significantly improve the probability of tumor control for these patients. The marginal increase of TCP does not justify DEs of such magnitude. In contrast, for severely hypoxic tumors which have initially very low TCPs (≤ 0.3), uniDE is not sufficient and a more focused application of the dose is needed. The low values of TCP_{ideal} for patient #9 in the case of conventional IMRT and uniDE are due to a very large tumor volume in addition to large areas of severe hypoxia

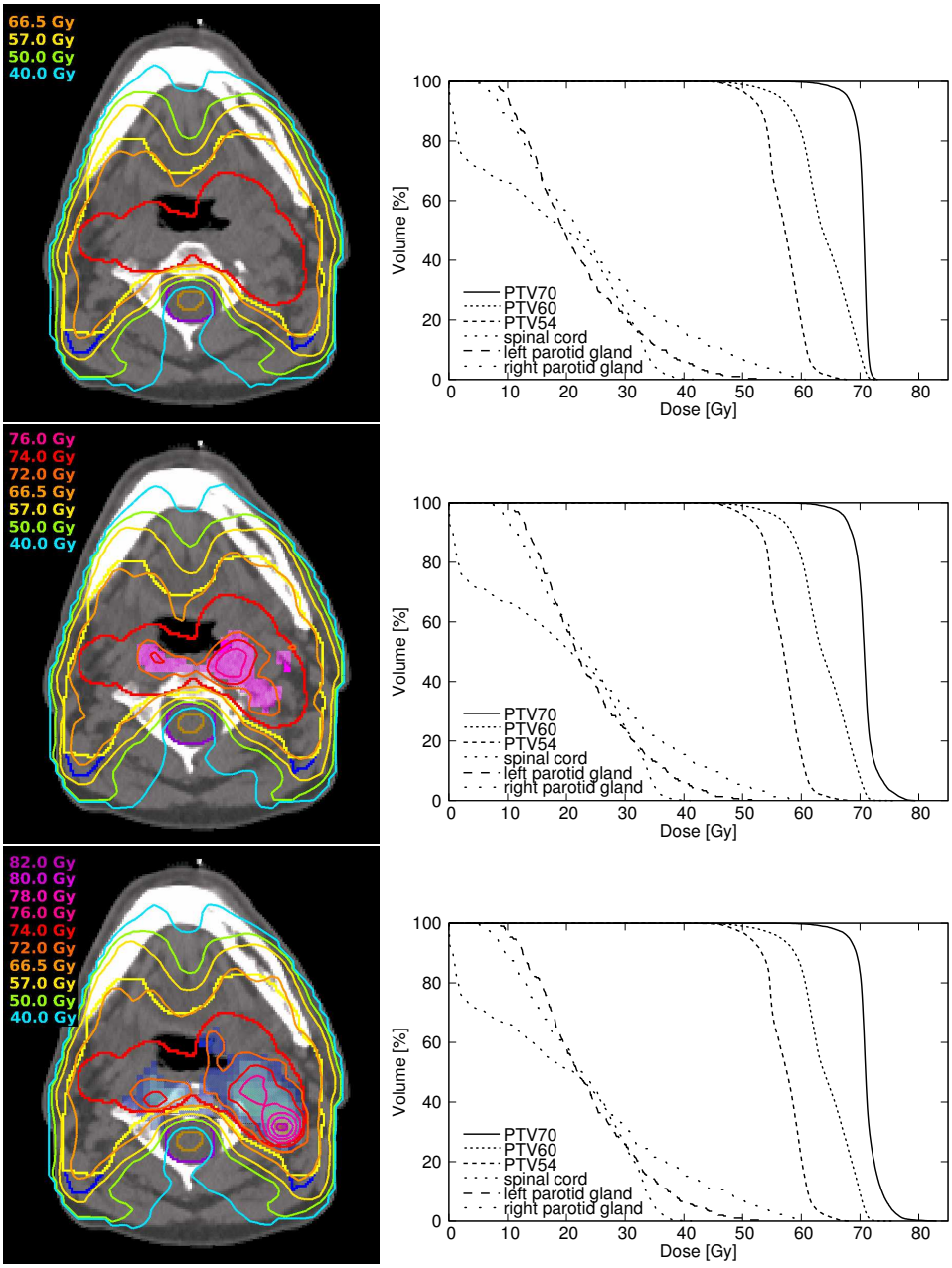

Figure 1: DP Treatment Planning. Dose distributions and corresponding DVHs for patient # 12. (a) Conventional IMRT plan. (b) uniDE to the FDG PET positive area shown in purple. (c) DPBN according to the superimposed DE map determined from dynamic FMISO PET scans. Volumes of interest: PTV70 (red), PTV60 (yellow), PTV54 (blue), spinal cord (brown) and expanded spinal cord (purple).

which would have required higher doses than 70 or 77 Gy. The TCP values for these patients (#7, 9 and 12) show the high potential of DPBN. Notice, that for patients where TCP for DPBN is significantly higher than for uniDE, a 10% DE is not sufficient and therefore the maximum DEF required for DPBN has to be higher than 1.1. On the other hand this means, that for patients where DEF_{max} for DPBN is lower than 1.1, the TCP will be higher for the uniDE approach than for DPBN. This is a consequence of the fact, that TCP values increase with increasing dose - even if the applied dose is higher than necessary.

These most hypoxic patients also affect the mean TCP for the population of this study. The major quality shown by the mean TCP values is the 14.3% increase in TCP_{real} when applying DPBN. Especially for patients with highly hypoxic tumors, which have very low probabilities of treatment success when treated with 70 Gy, DPBN seems to be highly promising. The comparison with uniDE, where only an increase of 1.8% is observed, shows

Pat #	$\mathbf{DEF_{max}}$	$\mathbf{DEF_{mean}}$
1	1.033	1.008
2	1.198	1.010
3	1.172	1.011
4	1.229	1.006
5	1.264	1.007
6	1.190	1.018
7	1.415	1.019
8	1.072	1.004
9	1.664	1.021
10	1.185	1.016
11	1.145	1.019
12	1.350	1.030
13	1.052	1.006

Table 2: Maximum and mean DEFs for DPBN determined for each patient on the basis of dynamic FMISO PET data. Mean DEF values refer to the FDG-based BTV.

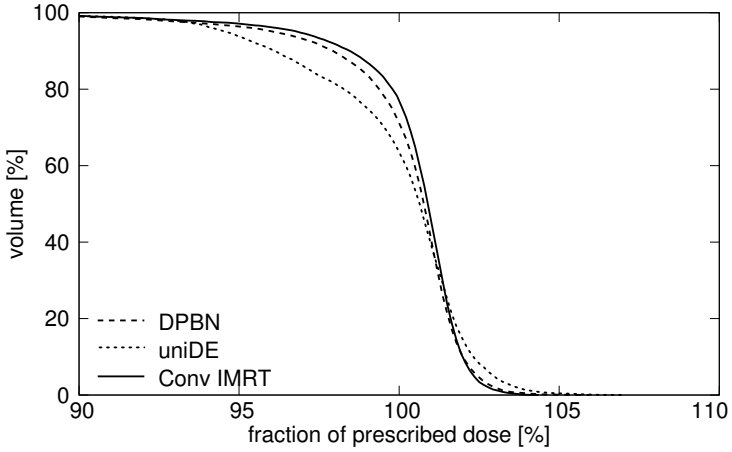

Figure 2: Effective DVH. Target coverage of prescribed dose for patient # 12. The fraction of prescribed dose is displayed for the uniform DE and hypoxia DPBN in comparison to the DVH of the conventional IMRT plan. The prescription of DPBN can be achieved better than uniDE and almost as well as the uniform dose of conventional IMRT.

evidence of the large benefit of DPBN. For those patients, the uniDE is not powerful enough to overcome hypoxia induced radioresistance.

The computation of TCP_0 revealed TCPs comparable to the conventional IMRT plan for both uniDE and DPBN. This is a consequence of nearly unchanged overall doses and small boost volumes.

4 Discussion

The presented work consists of a DP planning study of a group of 13 HNC patients. The aim of the study was to compare two different DE strategies, uniDE and DPBN, in a patient population while maintain-

Pat	**Conv**			**uniDE**			**DPBN**		
#	V_{95}	V_{100}	V_{105}	V_{95}	V_{100}	V_{105}	V_{95}	V_{100}	V_{105}
1	99.1	75.6	0	98.6	72.2	0.5	99.6	74.6	0
2	92.5	69.5	0	89.1	56.4	0.5	92.2	63.9	0
3	96.3	76.7	0	93.6	67.0	0.1	95.6	69.8	0
4	98.0	90.1	0	96.4	78.4	0.5	97.7	89.2	0
5	95.0	72.7	0	94.8	70.9	0.1	95.1	71.1	0
6	98.8	80.8	0	98.5	80.1	0	98.3	78.8	0
7	98.4	86.6	0	97.2	78.0	0.4	97.7	83.5	0.4
8	96.4	87.0	0	95.5	83.6	0.2	96.4	88.8	0
9	99.4	88.8	0	80.7	53.4	0.4	96.8	60.8	0.2
10	97.4	82.4	0.1	91.9	66.8	0.3	96.8	74.0	0
11	99.9	92.6	0.1	98.9	82.5	0.3	99.7	83.8	0
12	97.1	76.9	0	93.8	63.5	0.4	96.4	71.1	0.1
13	99.6	90.5	0	98.3	81.2	0.4	98.3	85.9	0

Table 3: Evaluation of target coverage: fractional volume (in %) that receives at least 95, 100 or 105% of the prescribed dose.

Pat	$\mathbf{TCP_{ideal}}$			$\mathbf{TCP_{real}}$			$\mathbf{TCP_0}$			out-
#	Conv	uniDE	DPBN	Conv	uniDE	DPBN	Conv	uniDE	DPBN	come*
1	0.817	0.857	0.852	0.836	0.875	0.861	0.869	0.896	0.886	1
2	0.530	0.629	0.637	0.000	0.000	0.000	0.000	0.000	0.000	0
3	0.688	0.757	0.784	0.326	0.238	0.393	0.425	0.312	0.469	1
4	0.644	0.753	0.713	0.727	0.814	0.773	0.783	0.845	0.808	1
5	0.870	0.881	0.915	0.879	0.891	0.903	0.921	0.930	0.929	1
6	0.853	0.883	0.934	0.884	0.905	0.939	0.946	0.953	0.962	1
7	0.135	0.152	0.875	0.198	0.193	0.750	0.791	0.809	0.827	0
8	0.859	0.886	0.876	0.897	0.921	0.916	0.910	0.927	0.923	1
9	0.002	0.002	0.706	0.000	0.001	0.489	0.711	0.781	0.780	0
10	0.832	0.871	0.907	0.867	0.889	0.905	0.927	0.940	0.942	1
11	0.603	0.670	0.764	0.679	0.739	0.793	0.813	0.846	0.872	1
12	0.316	0.373	0.799	0.347	0.393	0.744	0.793	0.808	0.869	0
13	0.612	0.670	0.666	0.617	0.643	0.659	0.676	0.695	0.708	0
avg	**0.597**	**0.645**	**0.795**	**0.559**	**0.577**	**0.702**	**0.744**	**0.749**	**0.767**	**0.615**

Table 4: TCP values calculated for different scenarios. TCP_{ideal}: TCP of an ideal situation, where all tumor voxels are irradiated with exactly the prescribed dose. TCP_{real}: TCP values determined for the real situation, assuming the established TCP-model is valid. TCP_0: TCP assuming the tumor tissue is homogeneous and nevertheless irradiated with the different DE treatment plans. *0: local recurrence, 1: no local recurrence.

ing the requirement of isotoxicity. Previously published investigations either showed the feasibility of uniDE exemplarily for a single patient [10, 12] or studied the possibility of performing DPBN [13, 14]. The presented paper additionally estimates the possible gain in terms of TCP for the different therapy approaches.

The study revealed, that under the condition of isotoxicity, both DE methods are feasible. For the DPBN approach, the prescriptions could be realized in a larger fraction of the target than for uniDE. The lower grade of target coverage for uniDE is partially due to the fact that the dose gradient always lies inside the BTV. Here, the dose gradient was chosen to be inside the BTV due to the intrinsic effect of higher doses on TCP. Also higher dose levels in normoxic regions will increase TCP. In order to separate this effect from the effect of a dose escalation to a region with reduced sensitivity, the dose gradient was chosen to be inside the BTV. Hence, by virtue of the prescription a complete coverage of the FDG-enriched region with 77.0 Gy can hardly be reached. The DPBN strategy is based on a gradual dose prescription. In general, this results in a higher target coverage.

Furthermore it turned out that the areas of FDG enrichment which should receive additional 10% of dose had volumes up to 94 ccm. The determined volumes of the BTV were in most of the cases too large to be clinically acceptable because of the enhanced risk of acute reactions. In contrast, only small areas received comparable radiation doses using the DPBN approach. In a large number of cases, the maximum DEFs did stay significantly below 1.1. Only in severely hypoxic areas, doses of 2.2 Gy/fx or higher were needed.

For the purpose of this study, a constant DE was applied for the whole treatment course. The premise of this approach is to keep the expected value of surviving cells per voxel constant. Moreover, the reoxygenation time is assumed to be unaffected by the dose escalation. These assumptions lead to $\mathrm{DEF}_i = \alpha_0 D_0/(\alpha_0 D_0 - \ln(M_i))$. Due to hypoxia induced radioresistance, escalating the dose from the first day may not constitute the most efficient use of dose at the start of treatment. The escalated dose may be used more effectively by applying the DE after reoxygenation of the tumor. This approach would lead to

$$\overline{\mathrm{DEF}_i} = \frac{Fx_{tot}}{Fx_{accel}} = 1 + \frac{\ln(M_i)}{\alpha_0 D_0} \qquad (5)$$

where Fx_{tot} denotes the total number of fractions and Fx_{accel} is the number of DE fractions. The benefit of this DE strategy is focused on the treatment period where the escalated doses $D_i > D_0$ combine with a non-reduced cell sensitivity α_0. One of the major disadvantages of this strategy is the lack of information about the local reoxygenation status. Additionally, reoxygenation might take place too late so that the resulting escalated doses would be too high to be clinically applicable. However, for fast reoxygenating tumors the resulting DEFs will be smaller: $\overline{\mathrm{DEF}_i} < \mathrm{DEF}_i$.

Previously, a TCP model could be established [22] relating dynamic FMISO data with therapy outcome. This model formed the basis for the DE map used for DPBN. In addition, it allows us to estimate the potential benefit of the different DE strategies. The theoretically achievable increase in TCP has been determined for both DE branches. Assuming full validity of the TCP model, a large fraction of patients would be overtreated by the use of uniDE. At the same time, uniDE assigns too low doses for small severely hypoxic subvolumes. Especially in cases, where the TCP values are high even without increasing the dose, the benefit of higher dose levels would be too small compared to the enhanced risk of acute toxic reactions.

Moreover, the analysis showed a potential increase in TCP of $\sim 15\%$ for a population treated with DPBN, whereas the increase is only 2% for the uniDE approach. An estimation of TCPs assuming complete homogeneity of the tumor tissue shows no significant difference between the three treatment branches. Hence, DPBN based in dynamic FMISO PET revealed substantially more potential than uniDE using FDG in combination to a comparable risk level and should be sufficiently more successful to be verified in a clinical study.

However, the technical issues of delivering a DE treatment plan in a clinical setting have to be addressed in further studies. The theoretical benefits of DPBN may not be fully achieved due to e.g. the finite size of the radiation fields used for the step and shoot technique. Furthermore, the dosimetric aspect regarding small radiation fields remains a challenge. Also patient set-up issues are of great relevance for DE treatments.

In general, both chronic and acute hypoxia will affect the radioresistance of a tumor. In contrast to chronic or diffusion limited hypoxia, acute hy-

poxia results from a temporal closing of blood vessels on a (micro-)second basis [30]. Therefore, it may be difficult to measure acute hypoxia with macroscopic, non-invasive imaging modalities. Nevertheless, both phenomena are symptoms of the same insufficient and chaotically organized vasculature. The presented TCP model is based on parameters derived from dynamic FMISO PET scans which characterize the local vascular configuration of a tumor region. As PET does not have the temopral resolution which is necessary to image acute hypoxia, the developed TCP model takes primarily chronic hypoxia into account.

In contrast to other TCP models that take a reduced radiosensitivity due to hypoxia into account [24–26], the TCP model used in the context of this paper is determined based on realistic patient data. In contrast to the definition to only two tissue compartments [25, 26] (hypoxic and normoxic), the presented TCP model accounts for gradual sensitivity changes. Moreover, the model is calibrated to realistic patient data. Nevertheless, this TCP model is based on a rather small patient sample and represents a population average, which may introduce non-negligible errors.

The presented study is based on dynamic FMISO PET imaging, in order to measure tumor hypoxia. The use of FMISO for the assessment of hypoxia is still controversially discussed. Even though FMISO is the most extensively studied bio-marker for hypoxia imaging with PET, difficulties regarding the quantification of hypoxia are due to long diffusion and tracer uptake times. However, a recent investigation correlated the accumulation of FMISO in tumor tissue with the uptake of the hypoxia marker pimonidazole in immunohistochemical experiments [31].

5 Conclusions

The presented planning study showed the technical feasibility of uniDE and DPBN with normal tissue constraints comparable to conventional IMRT. The TCP model suggests that uniDE overtreats a substantial fraction of patients while not being sufficient for others. The expected population gain for DPBN was estimated to increase the TCP from 55.9 to 70.2%, which is comparable to the hypoxia modifying RT approach ARCON [19].

6 Acknowledgements

This project was financially supported by the German Research Foundation (DFG), grant no. AL 877/1.

References

1. Ling CC, Humm J, Larson S et al. Towards multidimensional radiotherapy (MD-CRT): biological imaging and biological conformality. Int J Radiat Oncol Biol Phys 2000; 47(3): 551-560.

2. Hicks RJ, Kalff V, MacManus MP et al. 18F-FDG PET provides high-impact and powerful prognostic stratification in staging newly diagnosed non-small cell lung cancer. J Nucl Med 2001; 42: 1596-1604.

3. Paudit N, Gonen M, Krug L, Larson SM. Prognostic value of [^{18}F]FDG-PET imaging in small cell lung cancer. Eur J Nucl Med Mol Imaging 2003; 30: 78-84.

4. Shields AF, Grierson JR, Dohmen BM et al. Imaging proliferation in vivo with [F-18]FLT and positron emission tomography. Nature Med 1998; 4(11): 1334-1336.

5. Eschmann SM, Paulsen F, Reimold M et al. Prognostic impact of hypoxia imaging with 18F-misonidazole PET in non-small cell lung cancer and head and neck cancer before radiotherapy. J Nucl Med 2005; 46(2): 253-260.

6. Hicks RJ, Rischin D, Fisher R, Binns D, Scott AM, Peters LJ. Utility of FMISO PET in advanced head and neck cancer treated with chemoradiation incorporating a hypoxia-targeting chemotherapy agent. Eur J Nucl Med Mol Imaging 2005; 32(12): 1384-1391.

7. Rasey JS, Koh WJ, Evans ML et al. Quantifying regional hypoxia in human tumors with positron emission tomography of [F-18]fluoromisonidazole. Int J Radiat Oncol Biol Phys 1996; 36: 417-428.

8. Piert M, Machulla HJ, Picchio M et al. Hypoxia-Specific Tumor Imaging with ^{18}F-Fluoroazomycin Arabinoside. J Nucl Med 2005; 46: 106-113.

9. Dehdashti D, Grigsby PW, Aintun MA, Lewis JS, Siegel BA, Welch M. Assessing tumor hypoxia in cervical cancer by positron emission tomography with ^{60}Cu-ATSM: Relationship to therapeutic response - a preliminary report. Int J Radiat Oncol Biol Phys 2003; 55(5): 1233-1238.

10. Grosu A-L, Piert M, Molls M. Experience of PET for target localisation in radiation oncology. Br J Radiol 2005; Supplement 28: 18-32.

11. Rajendran JG, Hendrickson KR, Spence AM et al. Hypoxia imaging-directed radiation treatment planning. Eur J Nucl Med Mol Imaging 2006; 33 Suppl 13: 44-53.

12. Chao KS, Bosch WR, Mutic S et al. A novel approach to overcome hypoxic tumor resistance: Cu-ATSM-guided intensity-modulated radiation therapy. Int J Radiat Oncol Biol Phys 2001; 49(4): 1171-1182.

13. Alber M, Paulsen F, Eschmann SM, Machulla HJ. On biologically conformal boost dose optimization. Phys Med Biol 2003; 48(2): N31-35.

14. Bentzen SM. Theragnostic imaging for radiation oncology: dose-painting by numbers. Lancet Oncol 2005; 6(2): 112-117.

15. Brizel DM, Sibley GS, Prosnitz LR, Scher RL, Dewhirst MW. Tumor hypoxia adversely affects the prognosis of carcinoma of the head and neck. Int J Radiat Oncol Biol Phys 1997; 38(2): 285-289.

16. Nordsmark M, Overgaard J. A confirmatory prognostic study on oxygenation status and loco-regional control in advanced head and neck squamous cell carcinoma treated by radiation therapy. Radiother Oncol 2000; 57; 39-43.

17. Nordsmark M, Overgaard M, Overgaard J. Pretreatment oxygenation predicts radiation response in advanced squamous cell carcinoma of the head and neck. Radiother Oncol 1996; 41: 31-39.

18. Fyles A, Milosevic M, Hedley D et al. Tumor Hypoxia has Independent Predictor Impact Only in Patients With Node-Negative Cervix Cancer. J Clin Oncol 2002; 20: 680-687.

19. Kaanders JHAM, Bussink J, van der Kogel A. ARCON: a novel biology-based approach in radiotherapy. Lancet Oncol 2002; 3: 728-737.

20. Vanderstraeten B, Duthoy W, De Gersem W, De Neve W, Thierens H. [18F]fluoro-deoxy-glucose positron emission tomography ([18F]FDG-PET) voxel intensity-based intensity-modulated radiation therapy (IMRT) for head and neck cancer. Radiother Oncol 2006;79(3): 249-258.

21. Das SK, Miften MM, Zhou S et al. Feasibility of optimizing the dose distribution in lung tumors using fluorine-18-fluorodeoxyglucose positron emission tomography and single photon emission computed tomography guided dose prescriptions Med Phys 2004; 31(6), 1452-1461.

22. Thorwarth D, Eschmann SM, Scheiderbauer J, Paulsen F, Alber M. Kinetic analysis of dynamic 18F-fluoromisonidazole PET correlates with radiation treatment outcome in head-and-neck cancer. BMC Cancer 2005; 5: 152.

23. Thorwarth D, Eschmann SM, Paulsen F, Alber M. A kinetic model for dynamic [^{18}F]-Fmiso PET data to analyse tumor hypoxia. Phys Med Biol 2005; 50: 2209-2224.

24. Carlson DJ, Stewart RD, Semenenko VA. Effects of oxygen on intrinsic radiation sensitivity: A test of the relationship between aerobic and hypoxic linear-quadratic (LQ) model parameters. Med Phys 2006; 33(9): 3105-3115.

25. Popple RA, Ove R, Shen S. Tumor control probability for selective boosting of hypoxic subvolumes, including the effect of reoxygenation. Int J Radiat Oncol Biol Phys 2002; 54(3): 921-927.

26. Tome WA, Fowler, JF. Selective boosting of tumor subvolumes. Int J Radiat Oncol Biol Phys 2000; 48(2): 593-599.

27. Jelen U, Söhn M, Alber M. A finite size pencil beam for IMRT dose optimization. Phys Med Biol 2005; 50(8): 1747-1766.

28. Pekkola-Heino K, Jaakkola M, Kulmala J, Grenman R. Comparison of cellular radiosensitivity between different localizations of head and neck squamous cell carcinoma. J Cancer Res Clin Oncol 1995; 121: 452-456.

29. Apisarnthanarax S, Chao KSC. Current imaging paradigms in radiation oncology (Review). Radiat Res 2005; 163(1): 1-25.

30. Dewhirst MW, Kimura H, Rehmus SW et al. Microvascular studies on the origins of perfusion-limited hypoxia. Br J Cancer Suppl 1996; 27: S247-251.

31. Troost EG, Laverman P, Kaanders JH et al. Imaging hypoxia after oxygenation-modification: comparing [18F]FMISO autoradiography with pimonidazole immunohistochemistry in human xenograft tumors. Radiother Oncol 2006; 80(2): 157-164.